(NASA-CR-169330) RESONANT DOPPLER VELOCIMETRY IN SUPERSONIC NITROGEN FLOW Ph.D. Thesis. Final Report, 31 Oct. 1979 - 31 Jul. 1982 (Princeton Univ., N. J.) 187 p HC A09/MF A01 CSCL 14B G3/35

N82-32699

Unclas 28963

PRINCETON UNIVERSITY

DEPARTMENT OF MECHANICAL AND AEROSPACE ENGINEERING

"RESONANT DOPPLER VELOCIMETER"

Final Report

for

Grant NAG 1-152

October 31, 1979 to July 31, 1982

Principal Investigators: R. B. Miles and M. Zimmermann

MAE Report No. T-1574

NASA/LANGLEY

Hampton, Virginia

Resonant Doppler Velocimetry in Supersonic Nitrogen Flow

by

Shi-wai S. Cheng

A thesis
presented to Princeton University
in partial fulfillment of the
requirements for the degree of
Doctor of Philosophy
in
Department of Mechanical and Aerospace Engineering

Princeton, New Jersey, 1982

RESONANT DOPPLER VELOCIMETRY IN SUPERSONIC NITROGEN FLOW

Prepared by:

Shi-Wai S. Cheng

Approved by:

Professor Richard B. Miles
Dissertation Advisor

Professor S. H. Lam
Dissertation Reader

Professor A. J. Smits
Dissertation Reader

ABSTRACT

The Resonant Doppler Velocimeter(RDV) is a new nonintrusive laser technique for flow diagnosis. This work applies the RDV technique to supersonic nitrogen flow with sodium atoms as tracer particles.

The measurements are achieved by shining a tunable single frequency laser beam into the flow. The resonant absorption spectrum of the seeded species is determined by observing the fluorescence signal intensity as a function of excitation wavelength. By comparing the peak absorption wavelength with a reference frequency marker, the flow velocity along the excitation beam can be obtained through the Doppler shift relation. By fitting the spectrum with a theoretical line profile, the static temperature and pressure of the flow can be determined.

Both mean flow and turbulence measurements have been investigated. Data are presented showing velocity, temperature, and pressure measured point by point across the flow field. These data generally agree well with the result obtained by the conventional pitot and total temperature surveys. Turbulence was induced by a small metal tab or a thin wire in the flow and observed by both hot wire and the RDV techniques. The velocity, temperature, and pressure sensi-

tivity curves of the RDV technique and the application of these sensitivity curves for identifying the velocity, temperature, or pressure fluctuation are discussed. The frequency response of the system was investigated by measuring some high frequency disturbances generated in the flow. Photographs of the flow field demonstrate the utility of the RDV for quantitative flow field visualization.

Some preliminary work on future development of the technique, including multi-dimensional measurements and applications to air flow and turbulence flow, is also presented.

ACKNOWLEDGEMENTS

To professor Richard B. Miles, I express my sincere appreciation for his guidance of this program and his constructive criticism as thesis advisor. His advice and assistance are essential to the success of this study. Special thanks are also extended to Dr. Micha Zimmermann, who not only taught me all the skills and knowledge that I need to accomplish this research project, but also helped me out like a brother in virtually all the problems that I had.

I would also like to thank the faculty, the professional staff, and the technical personnel of the Gas Dynamics Laboratory for their specially friendly assistance throughout my graduate program. Assistance from Robert Bogart in setting up the vacuum system, Gary Katona in solving problems in the electronic equipment, and Richard Gilbert in programming advice is gratefully acknowledged. The generosity of David Williams and Kayo Hayakawa in lending me hot wire anemometers and giving me useful advice on the hot wire technique is deeply appreciated.

Finally, I am indebted to my wife, Liu-Ching. Her understanding, help and patience provided the best encouragement throughout my graduate career.

This thesis carries No. 1574-T in the records of the Department of Mechanical and Aerospace Engineering.

CONTENTS

LIST OF TABLES

LIST OF FIGURES

Chapter I

INTRODUCTION

Due to the complexity of fluid motion phenomena and the difficulties involved in applying the equations of motion to even the simplest of the realistic situations, fluid dynamicists rely heavily on experiments. In fact, the experiments play a crucial role in the guidance of theoretical development. For the experimental results to be meaningful, a researcher must know precisely how the instrumental records are related to the various fluid dynamic parameters that he is trying to measure. Unfortunately, there is no perfect measurement technique; all the existing techniques have their limitations. Therefore, the development of new measurement techniques which can be applied beyond the limitations of existing techniques, or can improve the reliability, simplicity, and versatility of the current techniques, is extremely important. The work presented in this dissertation represents an effort to develop a new laser technique which can be used for flow visualization, as well as quantitative measurements in supersonic flow.

1.1 LIMITATION OF CONVENTIONAL ANEMOMETERS

The conventional anemometers are normally intrusive, that is, some solid probe must be introduced into the flow. Pitot probes, static pressure probes, total temperature probes, and hot wire anemometers all fall into this category. Therefore, probe interference is the common disadvantage of these techniques.

Pitot probes, static pressure probes, and total temperature probes are limited in frequency response as well as spatial resolution. Consequently, they are not suitable for turbulence or non-steady flow measurements. Even for the mean property measurements, one has to apply some assumptions to derive the fundamental flow properties such as velocity, static temperature, and static pressure from the measured quantities.

The hot wire technique was developed to achieve a high frequency response and a good spatial resolution for turbulence measurements (see Appendix B). To achieve this, one must use wires with diameters in the order of micrometers. The nonlinear and nonuniversal response of the wires with respect to the flow parameters forces the user to calibrate the hot wire probes against some standard instrument such as the pitot probe. Thus, the hot wire anemometer gives a comparison rather than an absolute measurement. This disadvantage, along with the fact that the hot wire response depends on a large number of flow parameters as well as its geome-

tric orientation, imposes some difficulties in the analysis of the measured results. So far, hot wire technique is still the only well-developed turbulence measurement technique for the supersonic flow.

1.2 OPTICAL TECHNIQUES

Nonintrusive optical techniques can be further classified into conventional flow visualization techniques and laser techniques.

Schlieren, shadowgraph, and interferometer are the most widely used conventional flow visualization techniques. The greatest shortcoming of these techniques lies in the qualitative nature of these techniques. In other words, they are normally not suitable for any quantitative measurements. Even for the qualitative analysis, one can not avoid the problem of having to analyze a three-dimensional flow field from a two-dimensional photograph or interferogram.

The introduction of the laser has made possible the development of modern optical point flow measuring systems. Among the many laser flow diagnostic techniques developed in the last twenty years, Laser Doppler Velocimetry(LDV) is certainly the most popular one (see Appendix A). However, despite the success in applying the LDV to mean velocity measurements in subsonic and transonic flows, the LDV has very limited applications for supersonic flows and turbulent flows. This is mainly caused by the "particle lag" problem,

the bias to higher speed particles, and difficulties in getting particles into low speed regions. These serious shortcomings of the LDV technique led researchers to seek new and more powerful laser techniques. The Resonant Doppler Velocimetry(RDV) is a direct result of this search.

1.3 RESONANT DOPPLER VELOCIMETRY(RDV)

The RDV, which is basically a laser induced fluorescence spectroscopy (LIFS) technique, was proposed by R. B. Miles in 1975(1, 2) and demonstrated in hypersonic helium flow by M. Zimmermann and R. B. Miles(3-6). This technique uses atomic species as the marker particles, thus eliminates the particle lag problem. The signal came from the fluorescence emission of the seeded tracer atoms which were excited with a tunable dye laser. The spectral lines of the tracer atoms can be obtained by tuning the dye laser frequency. Then, from the Doppler shift of the spectral lines, one can calculate the flow velocity. From the shape of the spectral line, the static temperature and static pressure can be derived. These features make the RDV a very powerful and attractive point measurement technique. Furthermore, the fluorescence signal is strong enough to be observed visually, and it is not integrated along the path of the laser light if it is viewed perpendicular to the direction of the laser light. Thus, the RDV is also an excellent flow visualization technique.

This work extends the application of the RDV from hypersonic helium flow to supersonic nitrogen flow, again using sodium atoms as the tracer particles. Preliminary turbulence measurements have also been made.

The differences between the present work and the work on hypersonic helium flow can be understood from several aspects. First of all, there is virtually no pressure induced absorption wavelength shift in the sodium-helium system, while the pressure shift is not negligible in the sodium-nitrogen system. Second, since the helium molecules are atomic, there is no internal energy mode in their structures. On the contrary, the nitrogen molecules are diatomic. The closely-lying vibrational and rotational energy levels can quench the excited sodium atoms; that is, inelastic collision processes exist in the nitrogen-sodium system. Third, helium can be expanded to a very high Mach number because of its very low condensation temperature. In hypersonic flow, helium has a very low static temperature and static pressure. Consequently, the sodium spectral lines detected are very narrow. Nitrogen has a condensation temperature of 77.364°K, so it can only be expanded to a Mach number around 3.6 from room temperature. Thus, the spectral lines are much broader than those obtained from the hypersonic helium flow. All of these make the work on supersonic nitrogen flow much more challenging than that on hypersonic helium flow. But supersonic nitrogen flow is much more re-

alistic than hypersonic helium flow. This point makes the effort worthwhile.

The basic theory of this technique is reviewed in Chapter II. The experimental setup is described in Chapter III. Chapter IV discusses the experimental procedure and the method by which the data is processed. Chaper V presents the experimental results from the measurements using the RDV technique, as well as the conventional techniques. Some preliminary work on the future development of the RDV technique is discussed in Chapter VI. Chapter VII gives a number of conclusions on the RDV technique. The LDV technique and the hot wire technique are briefly reviewed in Appendix A and Appendix B. The supersonic application of these techniques are emphasized. Appendix C discusses the Velocity Dependent Voigt Profile. Appendix D contains a brief discussion of the temperature dependence of the collision cross section.

Chapter II

THEORY

In this chapter, a brief discussion of the fundamental physical phenomena is presented. These phenomena are the building blocks for the RDV technique. However, besides being brief and fundamental, the discussion will be specific. Only those theories related to sodium atom and nitrogen flow are presented.

2.1 SODIUM ATOMIC STRUCTURE

Since it is one of the most common metals used , the properties of the sodium are well known. Table 1 summarizes some sodium properties which are important for this work. Further information about the sodium can be found in Ref. 8 as well as 9, as well as a tremendous number of other sources.

The reasons why sodium was chosen are as follows:

1. Sodium has been investigated extensively with optical spectroscopy.
2. Sodium has a simple atomic structure and no stable isotopes.
3. Sodium has a large optical absorption cross section.

TABLE 1

Physical & Spectral Properties of Sodium Atoms

SODIUM PROPERTIES	
ATOMIC WEIGHT (g/gmole)	22.9898
MELTING POINT (^{o}C)	97.81±0.03
BOILING POINT (^{o}C)	882.9
ELECTRONIC CONFIGURATION	$1s^2 2s^2 2p^2 3s^1$
POLARIZABILITY ($10^{-24}cm^3$)	23.6±0.47
NO NATURAL ISOTOPES	

PROPERTIES OF SODIUM D LINES	
NATURAL LINEWIDTH (MHz)	9.76±0.3
LIFE TIME (nsec)	16.3±0.5
RESONANCE WAVELENGTH (Å)	
D_1 LINE	5896
D_2 LINE	5890
OSCILLATOR STRENGTH	
D_1 LINE	0.33
D_2 LINE	0.65

SODIUM VAPOR PRESSURE	
T(^{o}C)	P(torr)
127	2.2×10^{-6}
227	1.15×10^{-3}
327	5.02×10^{-2}
427	0.888
527	7.53
627	39.98
727	148.5
827	453.7

4. The absorption frequency of the sodium D lines is within the wavelength range of single frequency dye lasers.

The sodium atomic structure is shown in Figure 1. The detailed structures of the sodium D_1 and D_2 lines are shown in Figure 2.

The symbols are conventional, i.e.,

$$n^m L_J$$

where n is the principal quantum number

m is the angular multiplicity

L is the total orbital angular momentum quantum number

J is the total angular momentum quantum number

Since sodium has only one free electron, the multiplicity is two.

The F quantum number is associated with the total angular momentum $\vec{F}$.

$$\vec{F} = \vec{J} + \vec{I}$$

where $\vec{J}$ is the electron angular momentum(orbital + spin) and $\vec{I}$ is the nuclear spin angular momentum

$$|J - I| \leq F \leq J + I$$

The F number corresponds to the hyperfine structure of the atom. The selection rules for F are

$$\Delta F = 0, \pm 1$$

Figure 1: Sodium Atomic Structure (10)

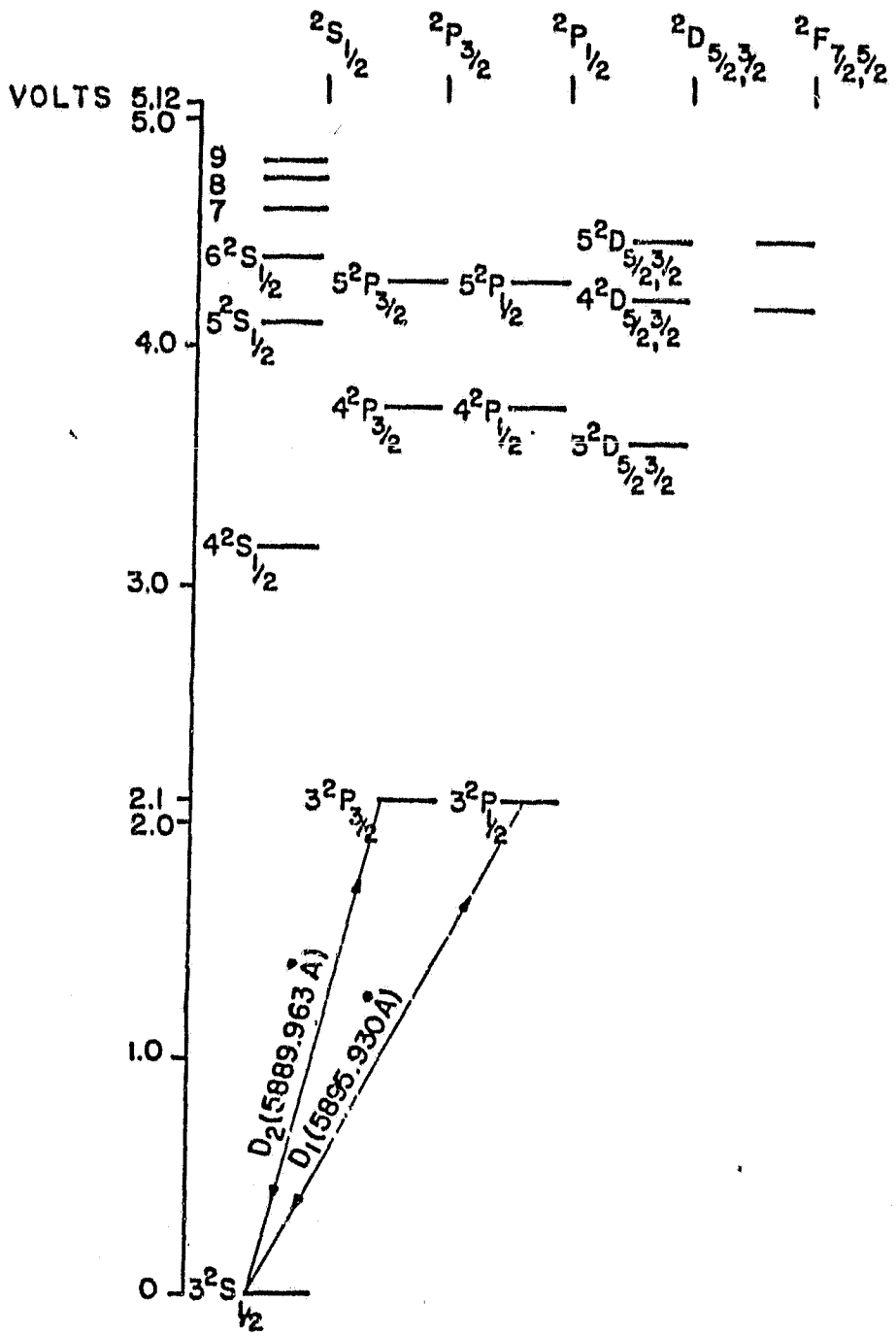

Figure 2: Structure of Sodium D_1 & D_2 Lines (11)

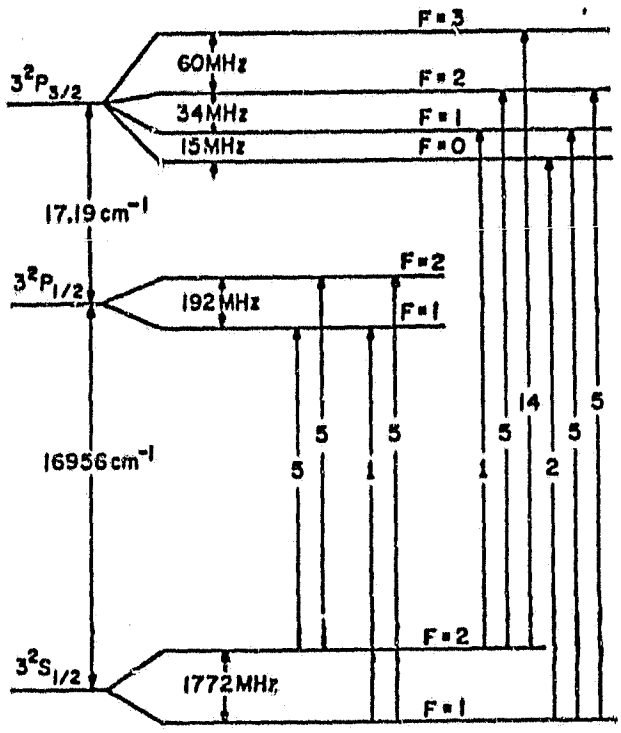

The arrows connecting the hyperfine levels in Figure 2 indicate the allowed transitions. The number associated with each arrow indicates the relative weight of transition probability.

To take advantage of the larger absorption cross section, we used the sodium $D_2(3^2S_{1/2} - 3^2P_{3/2})$ lines as the signal source line throughout this work.

2.2 LINE BROADENING AND LINE SHIFT

The spectral line broadening can be classfied into two catagories the homogeneous broadening and the inhomogeneous broadening. As the names infer, the homogeneous broadening affects all the sodium atoms equally, while the inhomogeneous broadening affects different group of sodium atoms differently. The broadening phenomena are very important for the RDV because they allow us to extract the temperature and pressure information. A brief treatment of line broadening theory is given here. Detailed analyses can be found in Ref. 12 - 18.

2.2.1 Natural Broadening

The excited atomic state will remain excited only for a finite period of time, and then give up the extra energy it gained and return to the ground state. How long it remains excited depends on the nature of the atom and the environ-

mental conditions. In the absence of collisional de-excitation, the lifetime of an excited state must be related to the transition probability for spontaneous emission A_{21}. Since the ground state is stable, we may assume its lifetime is infinite; the relation for the lifetime is then

$$\tau_2 = 1/A_{21}$$

where 2 stands for the excited state,

1 stands for the ground state, and

A_{21} is Einstein A coefficient

From the Heisenberg's uncertainty principle, the linewidth is

$$\Delta\nu_N = 1/(2\pi\tau_2)$$

This is called natural broadening and is a property of the atom. For sodium D lines, as shown in Table 1, the natural linewidth is 9.76 MHz.

2.2.2 Pressure Broadening and Pressure Shift

In a gas flow, the collisions between sodium atoms and other gas molecules play an important role in determining the life time of the excited sodium atoms. In a sodium and nitrogen mixture, the following reactions may happen as the result of binary collisions between the excited sodium atoms and the ground state nitrogen molecules.

(I) $Na^* + N_2(0) \dashrightarrow Na^+N_2^- + K.E.$

(II) $Na^* + N_2(0) \rightarrow Na^* + N_2(0)$

(III) $Na^* + N_2(0) \rightarrow Na + N_2(0) + h\nu$

(IV) $Na^* + N_2(0) \rightarrow Na + N_2(v_f) + K.E.$

Case (I) is the chemical reaction between sodium and nitrogen. But $Na^+N_2^-$ is not stable(23). It may form only when Na and N_2 are very close to each other and then fall apart again. In other words, it can only be an intermediate form for other collision processes.

Case (II) is the elastic collision. As far as energies are concerned, nothing changes. But the periodic oscillation of the excited sodium atom will be interrupted by the collision and lose its phase memory. This kind of dephasing interaction causes a frequency broadening in the frequency domain.

Case (III) is the radiative de-excitation collision. The energy gained by the sodium atom is lost by emitting a photon. The wave train associated with the excited sodium is truncated by this type of collision. Again, if a Fourier transform is carried out, the frequency spectrum will be broadened. The emitted photons, along with the photon emitted by spontaneous emission, are the fluorescence signal we see. Depending on the pressure the collision de-excitation can occur at rates much faster than the rate at which spontaneous emission occurs.

Case (IV) is the nonradiative inelastic collision. Just like case (III), the sodium atom is de-excited but the energy goes into the vibrational, rotational, and translational states of the nitrogen molecules. This phenomenon is called quenching. This phenomenon will be discussed in the next section. Again this action ends the wave train of the excited sodium atom and causes line broadening.

All these collisions will broaden the spectral lines. From the analysis given by Ref. 19, the collision broadening is given by

$$\Delta\nu_c = 2/\tau_c = 2Z_b)_{Na\text{-}N_2} = 2N\sigma_b\bar{v}_{rel}$$

$$= 2N\sigma_b\sqrt{8\tilde{R}T/\pi m^*} \qquad \text{(II-1)}$$

where τ_c = collision time, i.e., averaged time between two successive collisions

Z = collision frequency

N = number density of nitrogen

σ_b = broadening collision cross section

$\bar{v}_{rel}$ = mean relative velocity between Na and N_2

$\tilde{R}$ = universal gas constant

T = absolute temperature

m^* = reduced mass

Besides broadening the lines, the existence of a foreign gas will also cause a shift of the sodium spectral line(19). The so-called pressure shift is due to the fact that, when nitrogen molecule approaches the sodium atom, it

will perturb the sodium energy levels (as shown in Figure 3).

How far the frequency will shift, and in which way it will shift, depend on the charge distribution of the interacting particles. For sodium and nitrogen collisions, it always shifts to the red(19). The amount of the shift is

$$\Delta\nu_s)_p = Z_s)_{Na-N_2} = N\sigma_s\bar{v}_{rel}$$

where σ_s = shift collision cross section

The broadening and shift cross sections are determined by the intermolecular potential. One should note that normally these cross sections are much larger than gas kinetics collision cross sections. Thus these optical collisions do not have to involve momentum transfer. These cross sections are normally temperature dependent because the collision process depends on the relative particle velocity, but, except for very high pressures, they are independent of the pressure. The temperature dependence can be seen from the impact theories proposed by Lindholm(44) and by Anderson(16).

$$\sigma_s = 2\pi\int_0^\infty r\sin\eta(r)dr$$
$$\sigma_b = 2\pi\int_0^\infty r\{1-\cos\eta(r)\}dr$$

where $\eta(r) = 2\pi\int_{-\infty}^{\infty}\Delta\nu(r)dt \approx 2\pi\Delta\nu(r)\frac{r}{v}$

$$\Delta\nu(r) = \begin{cases} -C_6/r^6 & \text{for van der Waals potential} \\ C_{12}/r^{12} - C_6/r^6 & \text{for Lennard-Jones potential} \end{cases}$$

r = intermolecular distance

Figure 3: Pressure Shift

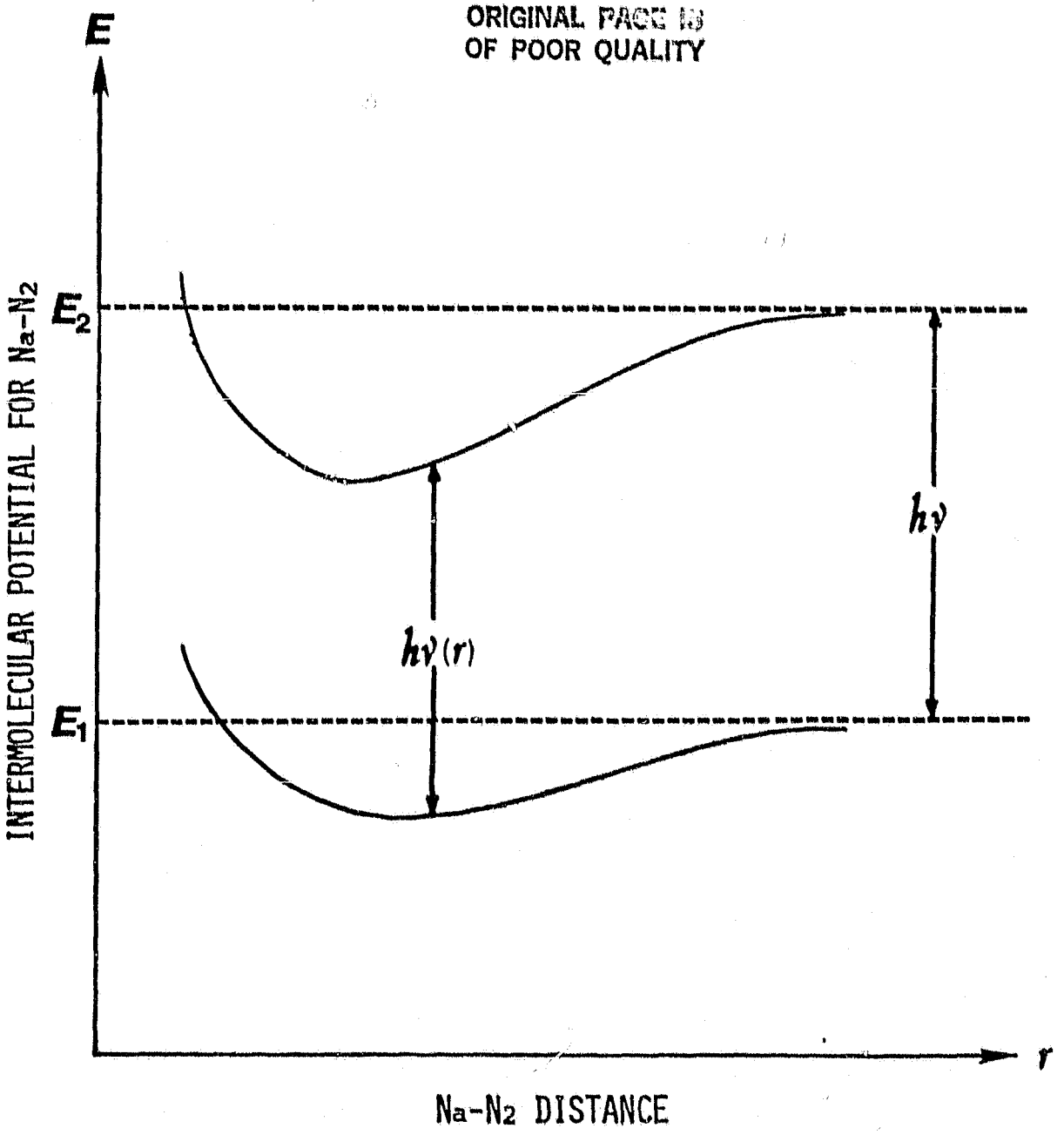

C_6, C_{12} = Constants

For the van der Waals potential(44),

$$\sigma_b = 4.08(C_6/\hbar)^{2/5}(\bar{v})^{-2/5} \propto T^{-0.2}$$
$$\sigma_s = -2.96(C_6/\hbar)^{2/5}(\bar{v})^{-2/5} \propto T^{-0.2}$$
$$\sigma_b/\sigma_s = -1.4$$

For the Lennard-Jones potential(44),

$$\sigma_b = 13.42\times(C_6/\hbar)^{2/5}\bar{v}^{-2/5}B(\alpha)$$
$$\sigma_s = 3.35\times(C_6/\hbar)^{2/5}\bar{v}^{-2/5}S(\alpha)$$

where $\alpha = 1.11\times\bar{v}^{6/5}C_{12}\hbar^{6/5}/C_6^{11/5}$

$$B(\alpha) = \int_0^\infty x\sin^2\{\tfrac{1}{2}(\alpha x^{-11} - x^{-5})\}dx$$

$$S(\alpha) = \int_0^\infty x\sin(\alpha x^{-11} - x^{-5})dx$$

Further discussions on this subject are given in Appendix D.

2.3 QUENCHING PHENOMENA

As was mentioned in the last section, quenching is a nonradiative, inelastic collision. Two different types of quenching may occur. Resonant quenching occurs when the colliding particles have close-lying energy levels; energy can be easily transferred, i.e., the quenching cross section is very large. Sodium and nitrogen collisions are very likely to be resonant quenching collisions, because of the close match between the v=8 vibrational state of nitrogen

and the sodium $3^2P_{3/2}$ state(only 0.1 ev apart). But all the experiments (20 - 22) and theoretical analyses (23 - 29) indicate that such a resonant transfer does not happen. The most probable vibrational state for energy to be channeled into is v=3 or 4, not v=8. Although it has been confirmed that the quenching process is nonresonant, the experimental quenching cross sections are much larger than predicted by nonresonant quenching mechanism(30 - 26). The large cross sections can best be explained on the basis of a "harpooning" mechanism, in which a strongly attractive ionic intermediate state provides the coupling between upper and lower covalent states.

The major features of this potential curve crossing quenching model for diatomic molecules are depicted schematically in Figure 4. The process is a combination of case (I) and (IV) in Section 2 of this chapter:

$$Na^* + N_2(0) \longrightarrow Na^+N_2^- \longrightarrow Na + N_2(v_f) + K.E.$$

As one can see from Figure 4, whether the inelastic transition will happen, and what the final state will be, both depend on the probabilities of the transition at each curve crossing point. Andreev(36) concluded that the probabilities of the process did not depend upon the initial kinetic energy of the collisional partners. Thus the dependence of the quenching cross section on temperature is determined mainly by the cross section of the system passing through

Figure 4: Potential Energy Curves for Quenching Collisions (a) Schematic (b) $Na-N_2$ System(24).

(a)

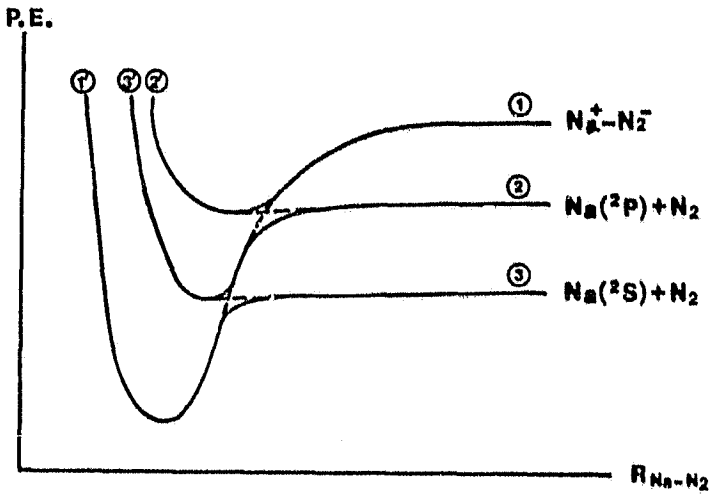

(b)

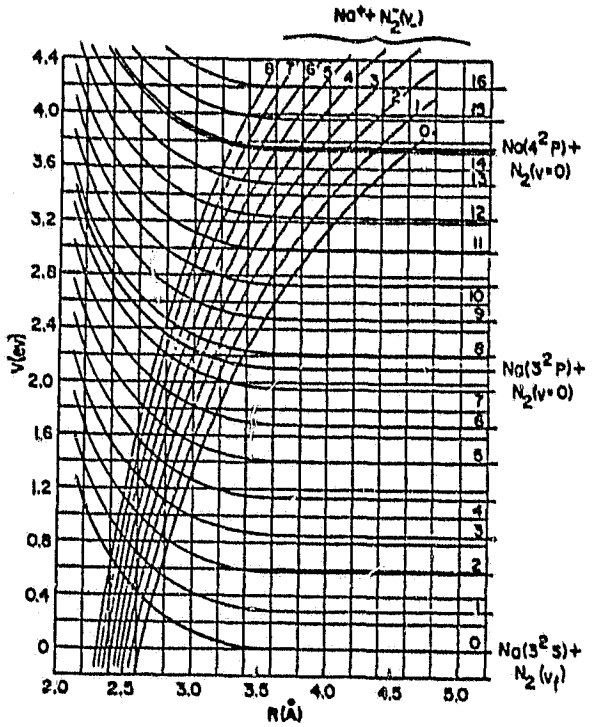

the nonadiabatic region. By using a Lennard-Jones potential, he calculated the total quenching probability to be 44.3%, and found that this probability depended on temperature to a very small degree. Lijnse(38) reached a similar conclusion about the temperature dependence by modifying Fisher's model(24,25). By including van der Waals attraction potential, he found

$$\sigma_q(T) = P_q \pi \cdot R_c^2 (1 - V(R_c)/KT)$$

where P_q = quenching probability

When he fitted the experimental results with this equation, he found that P_q = 45%, R_c = 3.5 Å, and $V(R_c)$ = -0.05 ev.

According to the study of Hollander and Alkemade(37), frequency-dependent quenching does not occur in the core and near wings of the sodium D doublet. Thus a constant quenching factor can be applied through the sodium D_2 spectra.

2.4 DOPPLER BROADENING AND DOPPLER SHIFT

Doppler broadening and shift are the results of the well known "Doppler effect", which is the apparent change in frequency of a signal due to the relative motion of the signal source and receiver.

From Figure 5, one can easily derive the Doppler shift to be

$$\frac{\Delta\nu}{\nu} = \frac{\nu' - \nu}{\nu} = \frac{\frac{U_z}{C}}{1 - \frac{U_z}{C}} = \frac{U_z}{C} + \left(\frac{U_z}{C}\right)^2 + \ldots$$

where C = speed of light

θ = angle between the wavevector $\vec{K}$ and the velocity $\vec{U}$

For the case we are dealing with ($U_z \ll C$), we can neglect terms of second and higher order(also relativistic Doppler effect).

Doppler broadening is caused by thermal motion. Because thermal motion is random, it follows the Maxwell distribution:

$$\frac{dN_u}{N} = \frac{1}{\bar{u}\cdot\sqrt{\pi}} e^{-u^2/\bar{u}^2} \cdot du$$

= fraction of atoms having velocity between u and u+du along laser direction

where $\bar{u} = \sqrt{2KT/M}$

= most probable velocity

M = mass of the molecule

K = Boltzmann constant

Since we are using laser as our light source, we have a well defined direction for the light wave. So we only need to consider the velocity distribution in one dimension, i.e., in the laser beam direction.

$$\frac{dN_\nu}{N} = \frac{1}{\sqrt{\pi}\bar{u}} \cdot e^{-\frac{C^2(\Delta\nu)^2}{\nu_o^2 \bar{u}^2}} \cdot \frac{C}{\nu} d\nu$$

= fraction of atoms with Doppler frequency shift $\Delta\nu$

Figure 5: Doppler Frequency Shift

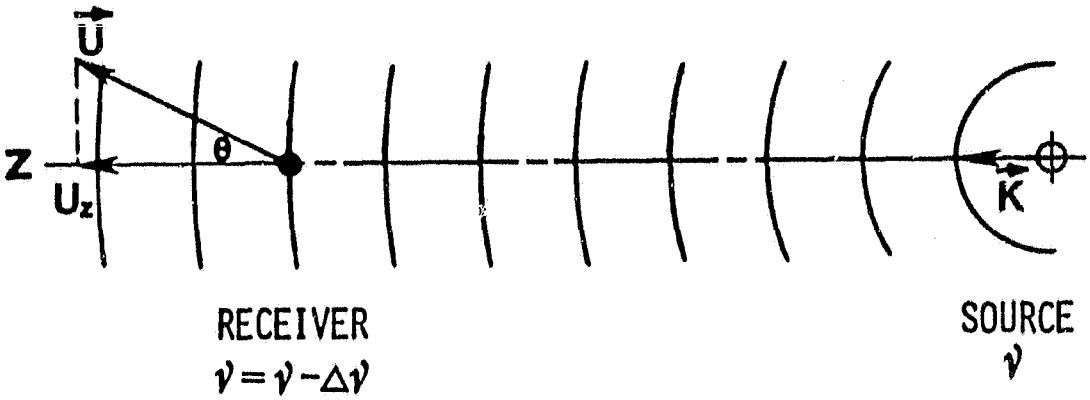

$$\Delta\nu = \nu \cdot \frac{U \cdot \cos\theta}{C}$$

where ν_o = resonant frequency

$\Delta\nu = \nu_o - \nu$

$$dN_\nu = dN_{\nu_o} \cdot \exp\{-\frac{c^2(\nu_o - \nu)^2}{\nu_o^2 \bar{u}^2}\}$$

This type of weighted shift broadens the spectral line. The Doppler broadening width is defined as the linewidth corresponding to $dN_\nu = 1/2\ dN_{\nu_o}$, that is,

$$\Delta\nu_G = 2(\nu_o \bar{u})\ \sqrt{\ln 2}/C \propto \sqrt{T} \qquad \text{(II-2)}$$

Note that the Doppler broadening originates from the Doppler shift and it has nothing to do with the collision process. With the fixed atomic species we have chosen, i.e., sodium, it depends only on the kinetic temperature.

For gas flow, besides a random motion, there is also a mean motion:

$\vec{V} = \vec{v} + \vec{u}$ = total velocity

where $\vec{v}$ = mean motion velocity

$\vec{u}$ = random motion velocity

The mean velocity will shift the whole spectral line by

$$(\Delta\nu_s)_D = \nu_o \cdot (v/C) \cdot \cos\theta \qquad \text{(II-3)}$$

where θ = the angle between v and laser beam direction

Henceforth, the term "Doppler shift" will be used to specify the frequency shift caused by the bulk mean velocity of the gas, and "Thermal broadening" will specify the broadening.

2.5 OTHER BROADENINGS

2.5.1 Transition Time Broadening

The sodium atom with mean velocity v will be exposed to the laser field for only a finite time. By applying the uncertainty principle, the line broadening width is(40)

$$\Delta\nu_T = v/(2\pi d)$$

where d = beam diameter

This is called transition time broadening.

2.5.2 Power Broadening

At high laser intensity, a substantial change in the population distribution of an atomic system can occur. For a two-level system, one can derive that the population difference becomes(41)

$$\left(\frac{N_1}{g_1} - \frac{N_2}{g_2}\right)_s = \left(\frac{N_1}{g_1} - \frac{N_2}{g_2}\right)_e/(1 + 2W_{21}\tau_{21})$$

where N_i = No. density of state i

g_i = degeneracy of state i

W_{21} = probability of stimulated transition

τ_{21} = natural life time

s : steady state

e : equilibrium state

In other words, the atomic systems are not thermally in equilibrium. Note that the denominator is a function of the laser frequency.

$$2W_{21}\tau_{21} = I/I_{sat}$$

where $I_{sat} = h\nu_{21}/2\sigma_{21}\tau_{21}$ = saturation intensity

ν_{21} = resonant frequency

σ_{21} = absorption cross section at frequency ν_{21}

This mechanism will broaden the spectral line by an amount(41):

$$\Delta\nu_p = \Delta\nu_L \cdot (\sqrt{1+I/I_{sat}} - 1)$$

where $\Delta\nu_L$ = total homogeneous broadening width

2.5.3 Instrument Broadening

The laser is not single-frequency light. Thus, though it is very narrow, the frequency bandwidth of the laser light is not zero. Furthermore, since the laser frequency is not absolutly stable, small frequency fluctuations about the mean laser frequency will make the apparent laser linewidth even broader.

Thus the instrumental broadening is the convolution of the laser line profile and the laser frequency jitter.

2.5.4 Turbulence Broadening

Turbulence motion leads to fluctuations in the mean velocity. Due to the randomness in the Doppler frequency shift, the spectral line profile is broadened. One should note that turbulence motion is a motion of an ensemble of fluid molecules and is therefore different from thermal motion.

2.5.5 Other Broadenings

Other broadening mechanisms, such as second order Doppler effect, wall collision broadening, self resonance broadening, direction broadening, recoil broadening, etc., are not important in our experiments and will not be discussed here. These broadenings and those discussed above are summarized in table 2.

2.6 LINE SHAPE

The study of spectral line shape is a well known tool to obtain knowledge of the physical properties of the medium containing the line-absorbing or line-emitting atoms. Because it is an indirect method, it is necessary to rely on the validity of line-broadening theories. These theories relate the characteristics of the line shape to the specific force laws governing the interaction between emitter and perturber. For our operating conditions, the impact theory(16), developed by Lorentz(42), Weisskopf(43), Lin-

TABLE 2

Source of Spectral Line Broadening in Gases

TYPE	SOURCES	FWHM
****** HOMOGENEOUS BROADENING ******		
NATURAL BROADENING	SPONTANEOUS EMISSION	$\Delta\nu_N = \frac{1}{2\pi\tau_2}$
PRESSURE BROADENING	COLLISIONS WITH FOREIGN GASES DEPHASING RADIATIVE QUENCHING CHEMICAL REACTION	$\Delta\nu_C = \Delta\nu_E + \Delta\nu_R + \Delta\nu_Q + \Delta\nu_{CH}$ $\Delta\nu_E$ $\Delta\nu_R$ $\Delta\nu_Q$ $\Delta\nu_{CH}$
SELF BROADENING	COLLISION WITH SAME SPECIES	$\Delta\nu_h = \frac{2}{2\pi}(N\sigma_h\bar{v}_{REL})$
TRANSIT TIME BROADENING	FINITE EXPOSURE TIME TO LASER FIELD	$\Delta\nu_T = \frac{v}{2\pi d}$
POWER BROADENING	POPULATION REDISTRIBUTION DUE TO LASER PUMPING	$\Delta\nu_P = \Delta\nu_L \cdot \left(\sqrt{1+\frac{I}{I_{SAT}}} - 1\right)$
INSTRUMENT BROADENING	LASER BANDWIDTH AND LASER FREQUENCY JITTER	$\Delta\nu_I$
GEOMETRICAL BROADENING	CURVATURE OF LASER WAVE FRONT	$\Delta\nu_{GE} = \frac{1}{2\pi}\sqrt{\frac{K v_0}{K r}} - \Delta\nu_T$
WALL COLLISION BROADENING	COLLISIONS WITH CONTAINER	$\Delta\nu_W = \frac{2}{2\pi\tau_W}$
RECOIL BROADENING	PHOTON RECOIL	$\Delta\nu_{PR}$
****** INHOMOGENEOUS BROADENING ******		
DOPPLER BROADENING	DOPPLER EFFECT THERMAL MOTION	$\Delta\nu_G = \nu_0\left[\frac{\vec{K}\cdot\vec{V}}{C} + \left(\frac{\vec{K}\cdot\vec{V}}{C}\right)^2 + \ldots\right]$
TURBULENCE BROADENING	DOPPLER SHIFT TURBULENCE FLUCTUATION	$\Delta\nu_{TU}$

dholm(44), and Anderson (45), holds quite well. The homogeneously broadened spectral line shape, known as the Lorentzian line shape, can be expressed as :

$$I_\nu = I_o \cdot \frac{(\Delta\nu_L/2)}{(\nu - \nu_o - \Delta\nu_s)^2 + (\Delta\nu_L/2)^2}$$

where $\Delta\nu_s$ = frequency shift = $(\Delta\nu_s)_p + (\Delta\nu_s)_D$

$\Delta\nu_L$ = total homogeneous line broadening

= $\Delta\nu_N + \Delta\nu_p + \Delta\nu_L + \Delta\nu_T + \cdots$

I_o = line intensity at line center

For inhomogeneous broadening, as we derived previously for Doppler broadening, the line shape is a Gaussian profile:

$$I_\nu = I_o \cdot \exp\{-c^2(\nu-\nu_o)^2/\nu^2\bar{u}^2\}$$

The actual line shape is obtained by convoluting these two profiles together (See Figure 6); this is equivalent to the weighted summation over the velocities of the Doppler shifted (due to thermal motion) Lorentzisn line shape, which is associated with active (emitting or absorbing) atoms moving with velocity $\vec{v}$. The weighting factor is the velocity distribution of the atoms. The convoluted profile, known as the Voigt profile, is given by(18)

$$V(x) = \frac{2\sqrt{\ln 2}}{\pi^{3/2}} \cdot \frac{a^2}{\Delta\nu_L} \int_{-\infty}^{\infty} \frac{e^{-\ln 2 \cdot y^2}}{(x - y)^2 + a^2}$$

where $x = 2[\nu - \nu_o - (\Delta\nu_s)_p]/\Delta\nu_G$

Figure 6: Convolution of Lorentzian & Gaussian Profiles

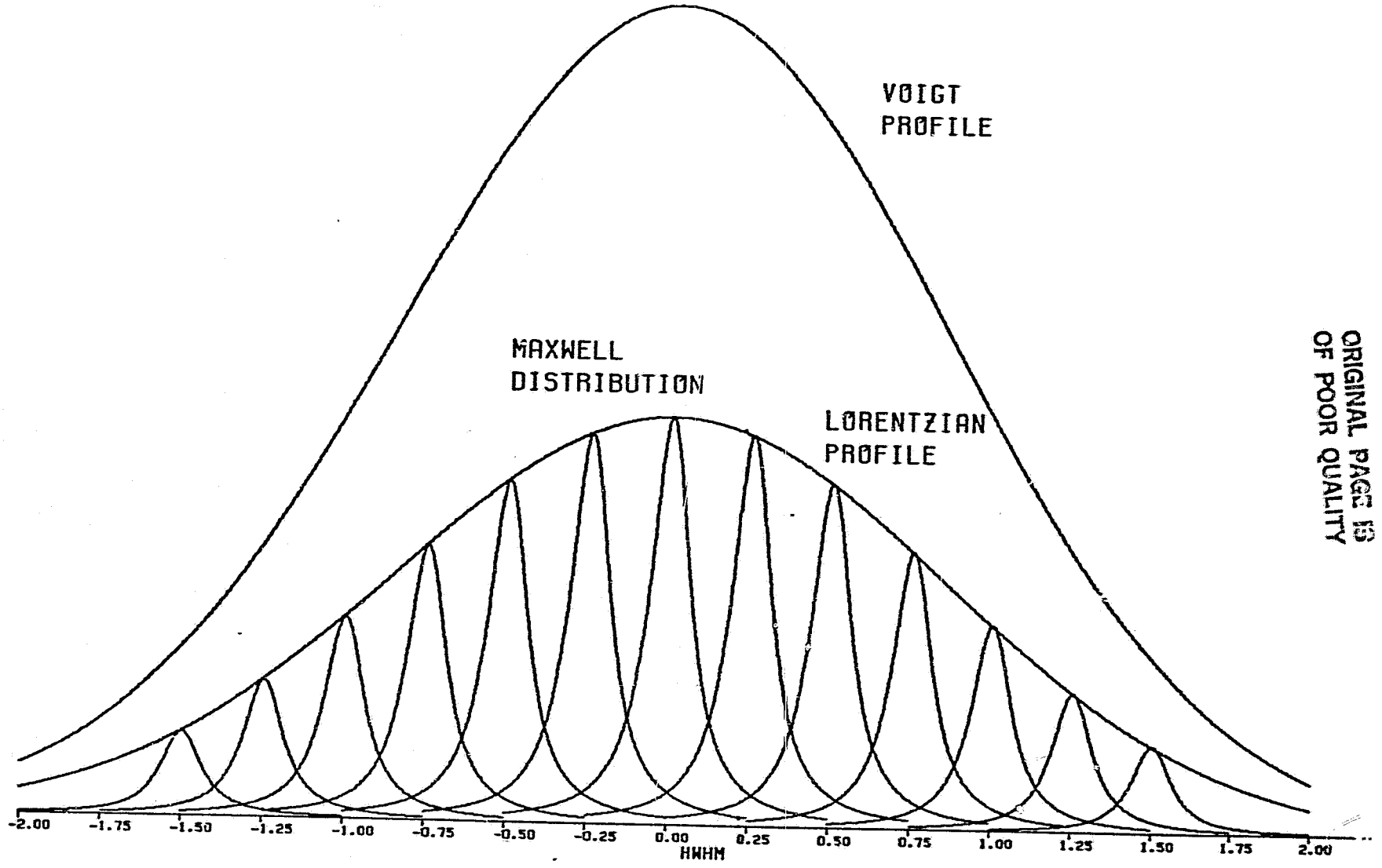

$$y = 2(\nu_o \cdot u/C)/\Delta\nu_G$$

$$a = \Delta\nu_L/\Delta\nu_G$$

These different profiles, with the same linewidth and line center intensity, are shown in Figure 7. It can be easily observed in this figure that the Gaussian profile drops off much faster than the Lorentzian profile. The slowly decaying wings, which are characteristic of the Lorentzian curve, are very important for accurate deconvolution of the data required in our experiments.

2.7 SATURATION AND TRAPPING

2.7.1 Saturation

For the RDV all the information is extracted from the line shape and shift. The absolute line intensity does not seem to be too important. However, if we want a good signal-to-noise ratio, we should make the laser intensity as high as possible. Unfortunately, as we increase the laser intensity, saturation effect will change the line shape, and we will lose the information we want.

The origin of saturation is the same as that of power broadening. The laser field redistributes the population which, in turn, reduces the absorption cross section, reduces the signal intensity, and broadens the homogeneous linewidth. The saturation effect is not uniform along the spec-

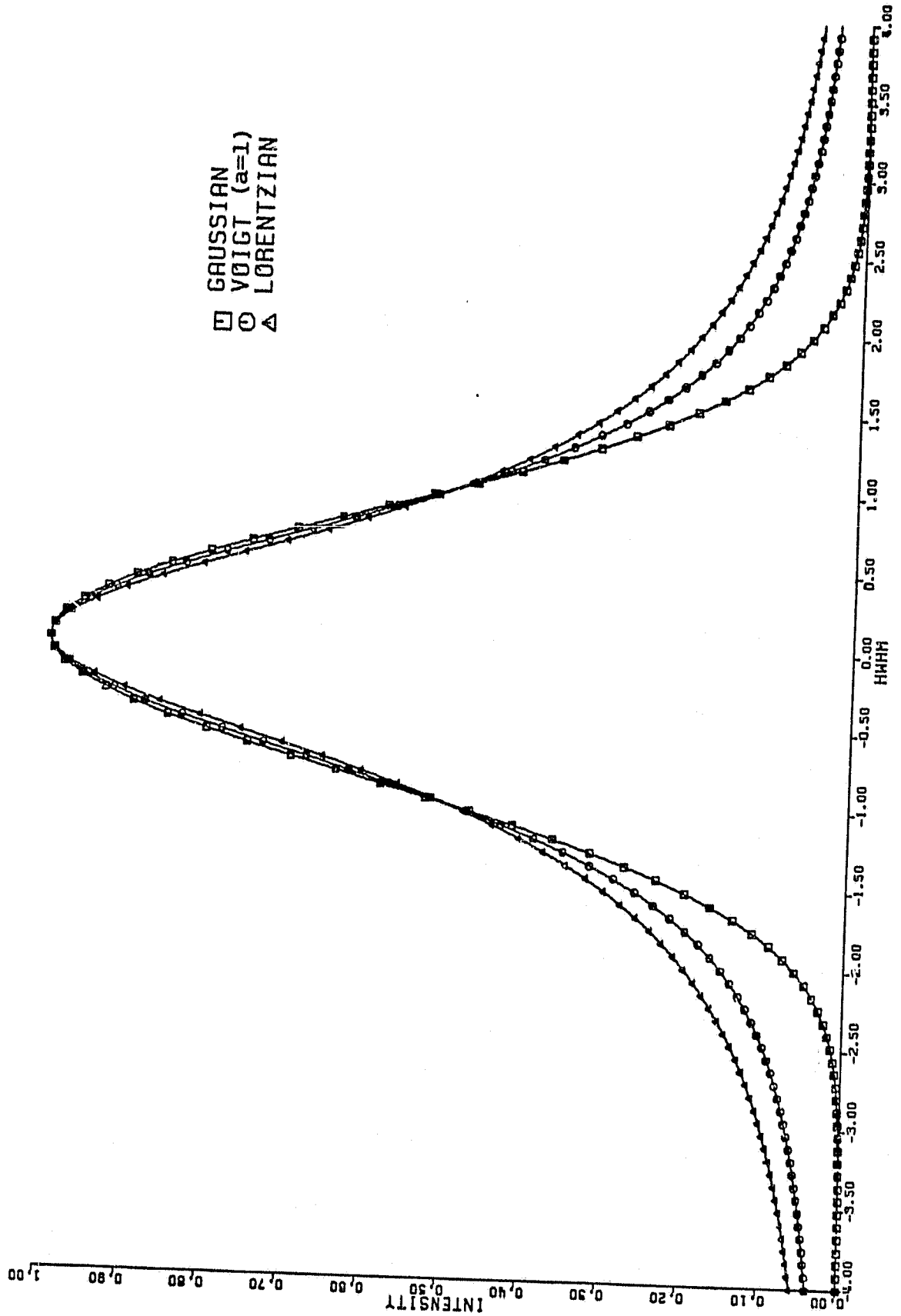

Figure 7: Lorentzian, Gaussian & Voigt Profiles

tral line. It is much easier to saturate the line center than to saturate the line wings, and different hyperfine lines have different saturation intensities. For ease in data reduction, saturation is an unwanted effect, consequently the laser intensity is kept well below saturation intensity $I_{sat}(\nu_o)$.

2.7.2 Trapping

When the line-absorbing or line-emitting medium is not optically thin, the photon emitted by one sodium atom may be absorbed by other atoms, in the same medium. The general differential equation describing the radiation intensity in such a medium is(46)

$$\frac{dI_\nu}{dx} = \varepsilon_\nu - K_\nu I_\nu$$

where ε_ν = volume emission coefficient

K_ν = absorption coefficient

Multiplying with the integrating factor $\exp(K_\nu x)$, and integrating from x=0 to x=L, this equation can be solved to give the result:

$$I_\nu(L) = I_\nu(0)\exp(-\int_0^L K_\nu dx) + \frac{\varepsilon_\nu}{K_\nu}(1-\exp(-\int_0^L K_\nu dx))$$

When the laser beam is shone into the gas medium containing the line-absorbing atoms, the laser intensity will be attenuated by the absorption along the passage towards the probe volume(Figure 8). Since the emission intensity is

much smaller than the laser intensity, the emission term can be neglected, and the laser intensity seen by the atoms in the probe volume is

$$I_\nu(L_1) \approx I_\nu(0)\exp(-\int_0^L K_\nu dx)$$

Similarly, when the emitted radiation leaves the probe volume, it is possible that it will be reabsorbed or trapped by sodium atoms along the path to the collection optics.

$$I_\nu(L_2) = I_\nu'(L_1)\exp(-\int_0^{L_2} K_\nu dx) + \frac{\varepsilon_\nu}{K_\nu}(1-\exp(-\int_0^{L_2} K_\nu dx)) \qquad \text{(II-4)}$$

where $I_\nu'(L_1)$= intensity of fluorescent light emitted in the direction of the collection optics

$$= \text{const} \cdot I_\nu(L_1)$$

For an optically thin medium,

$$\exp(-\int_0^L K_\nu dx) \approx \exp(-K_\nu L) \approx 1 - K_\nu L$$

Since the reabsorption can be neglected, the second term in equation (II-3) can be omitted. Thus,

$$I_\nu(L_2) \propto I_\nu(0)\{1-K_\nu(L_1+L_2)\}$$

Therefore, the fluorescence intensity collected by the collection optics is proportional to the absorption coefficient.

In the other extreme, for the optically thick medium, the exponential relation and the emission terms in Equation

Figure 8: Trapping

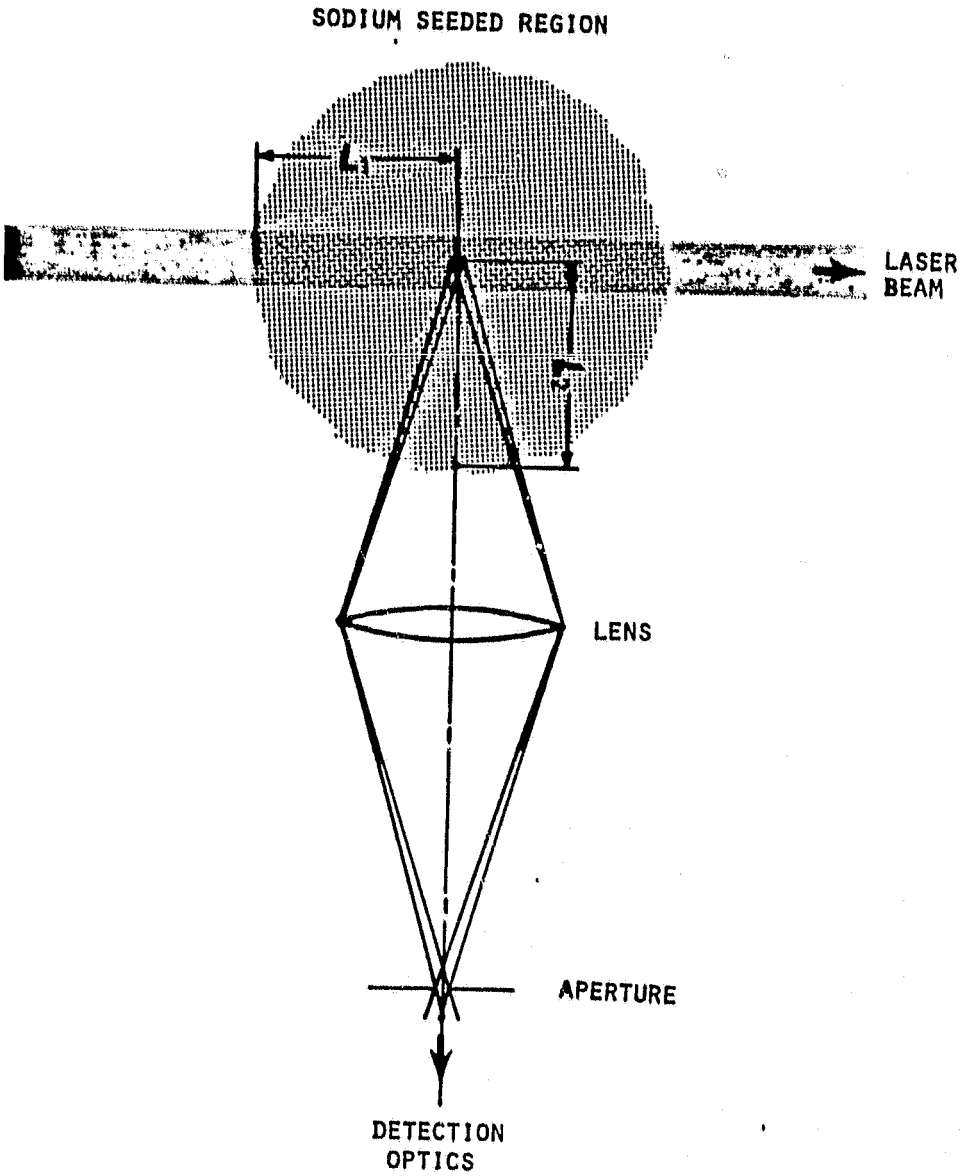

II-4 will complicate the intensity relation. Consequently the fluorescence line profile will no longer represent the absorption line profile faithfully.

2.8 OPTICAL PUMPING

The optical pumping process has been extensively discussed elsewhere(6, 47, and 48). Due to the selection rule for hyperfine transitions($\Delta F=0, \pm 1$), the selected excitation of one ground hyperfine state may mean that most of the population is in another ground hyperfine state. For example, exciting the transition $3^2S_{1/2}$, F=1 --> $3^2P_{3/2}$, F=1, allows a decay channel into the $3^2S_{1/2}$, F=2 state. After a few excitation cycles, most of the atoms in $3^2S_{1/2}$, F=1 state will be pumped into $3^2S_{1/2}$, state and not be available for excitation. But if the excited transition is $3^2S_{1/2}$, F=2 --> $3^2P_{3/2}$, F=3, such optical pumping phenomena will not appear, because only one decay channel exists back to the original state $\Delta F=-1$.

Since the laser intensity required for optical pumping is much lower than that required to produce saturation, optical pumping has a significant effect on the line shape, as discussed in detail by Walkup, et al.(49). As they found, the only way to avoid this type of line shape distortion is to keep the laser power low.

Chapter III

EXPERIMENTAL SETUP

The experimental setup is quite complicated. In order to make the discussion easier and clearer, the system will be discussed under three subdivisions entitled: the gas flow system, the laser and optics system, and the data acquisition system.

3.1 GAS FLOW SYSTEM

A schematic diagram of the basic facility is shown in Figure 9. The nitrogen gas used is commercially available bottled nitrogen. The stagnation chamber pressure was regulated by two pressure regulators in the main flow supply line. After the flow entered the stagnation chamber, it passed through a fine mesh. It was then mixed with the purge nitrogen flow which had passed through the sodium seeding device. The flow, containing the entrained sodium vapor, was then accelerated through an axisymmetric supersonic nozzle to about 700 m/sec. On the downstream side of the plenum chamber, an adjustable throttling needle was used to regulate the plenum chamber pressure. Most of the measurements were done at 5 nozzle diameters (exit diameter of the nozzle) downstream of the nozzle exit. Beyond the nee-

dle throat, the flow was evacuated by a 140 CFM Stoke vacuum pump.

The nozzle was conical with an area ratio of 0.14. The nozzle parameters are shown in Table 3. In most of our flow cases, the system was run with 12.96 psi stagnation pressure, and the pressure of the downstream side of the nozzle was controlled to match the exit jet pressure(12.7 torr). The Mach number calculated from these pressures was 3.2. The diameter of the plenum chamber was 5 inch. Thus the interference of the chamber wall on the flow was negliigible. The stagnation temperature of the mixture was measured by a total temperature probe to be about 350°K. However, from the total temperature survey, it was found that the temperature distribution was not symmetrical. This is because the seeding needle was not exactly centered.

The flow pressure in the seeding device was controlled by a differential pressure regulator to keep it higher than the pressure in the stagnation chamber by a fixed amount. Normally it is 10 psi higher. Since the flow rate through the seeding device was only a small fraction of the main flow, the higher total pressure in the seeding device did not noticeably affect the total pressure of the flow. This was checked with a pitot probe at downstream side of the nozzle. The total pressure with the purge gas pressure 10 psi higher than that of the main flow is only two percent higher than that of the equal pressure case. In the seeding

Figure 9: Gas Flow System

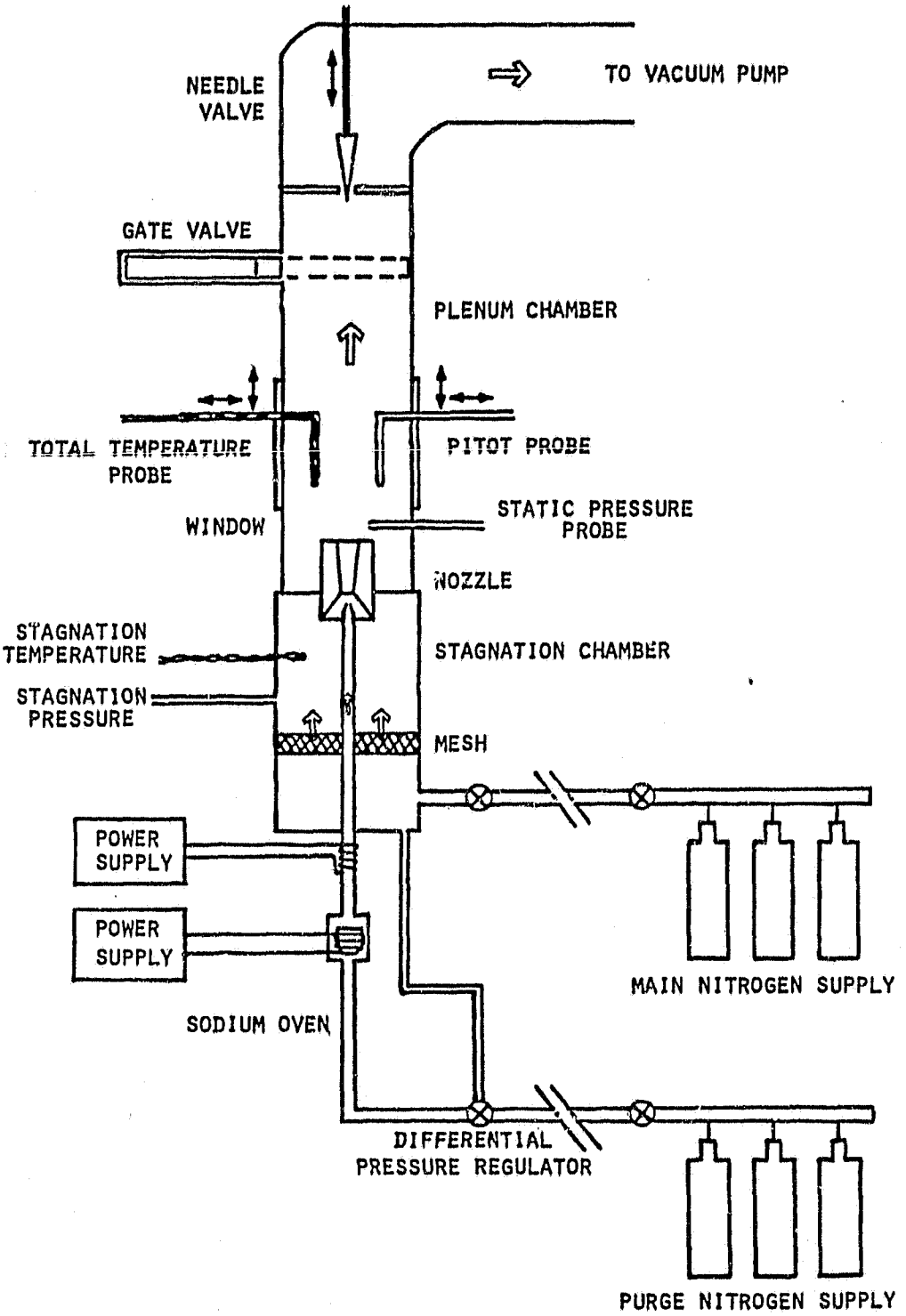

TABLE 3

Nozzle Properties

Throat diameter(in.)	0.086
Exit diameter(in.)	0.23
Constant nozzle divergent angle(deg.)	4
Expansion length(in.)	2.0

device, the sodium was contained in an oven heated by an electrical power supply to a temperature between 200°C and 300°C. The purge nitrogen flow was fed into the stagnation chamber through a needle which was heated by a separate power supply to about 700°C. This high needle temperature is required to reduce sodium condensation on the needle wall. The tip of the needle was positioned 0.5 inch upstream of the throat of the nozzle.

3.2 LASER AND OPTICS SYSTEM

Figure 10 depicts the schematic diagram of the optical system. The dye laser we used was a Spectra-Physics 580 tunable single frequency laser modified to include a jet stream dye cell. It was pumped by a Coherent Radiation model 53A argon ion laser. Some of the operating conditions of the dye laser are listed in Table 4. The frequency scanning was accomplished by applying proportional voltages to piezoelectric crystals attached to the etalon, the prism, and one

of the end mirrors in the cavity. The linear tunable range is about 5 GHz.

TABLE 4

Dye Laser Properties

Dye	Rodemine 6G
Input	1 Watt at 5145Å
Output	30-80 mWatt
Tuning range	4-5 GHz
Scan linearity	2% over 4 GHz scan
Linewidth	+7 MHz
Noise	3% RMS

The dye laser output beam was split in several directions. Part of the laser light was used by a feedback loop to stabilize the dye laser intensity. The laser light was also monitored by a Spex 1700 Czerny-Turner monochromator, a sealed pyrex sodium cell, and a Jodon model SA-1500 confocal spectrum analyzer. The purpose of using the monochromator and the sodium cell was to position the dye laser frequency at the sodium D_2 line. This was the spectral line used for all analyses. The spectrometer had a resolution of 10 GHz and was used for coarse adjustment. The cell had a resolution of about 3.5 GHz and was used for fine adjustment. The spectrum analyzer, with a free spectral range of 150 MHz and a linewidth of 7 MHz, was used to check the mode structure and frequency stability. Frequency calibration was also ac-

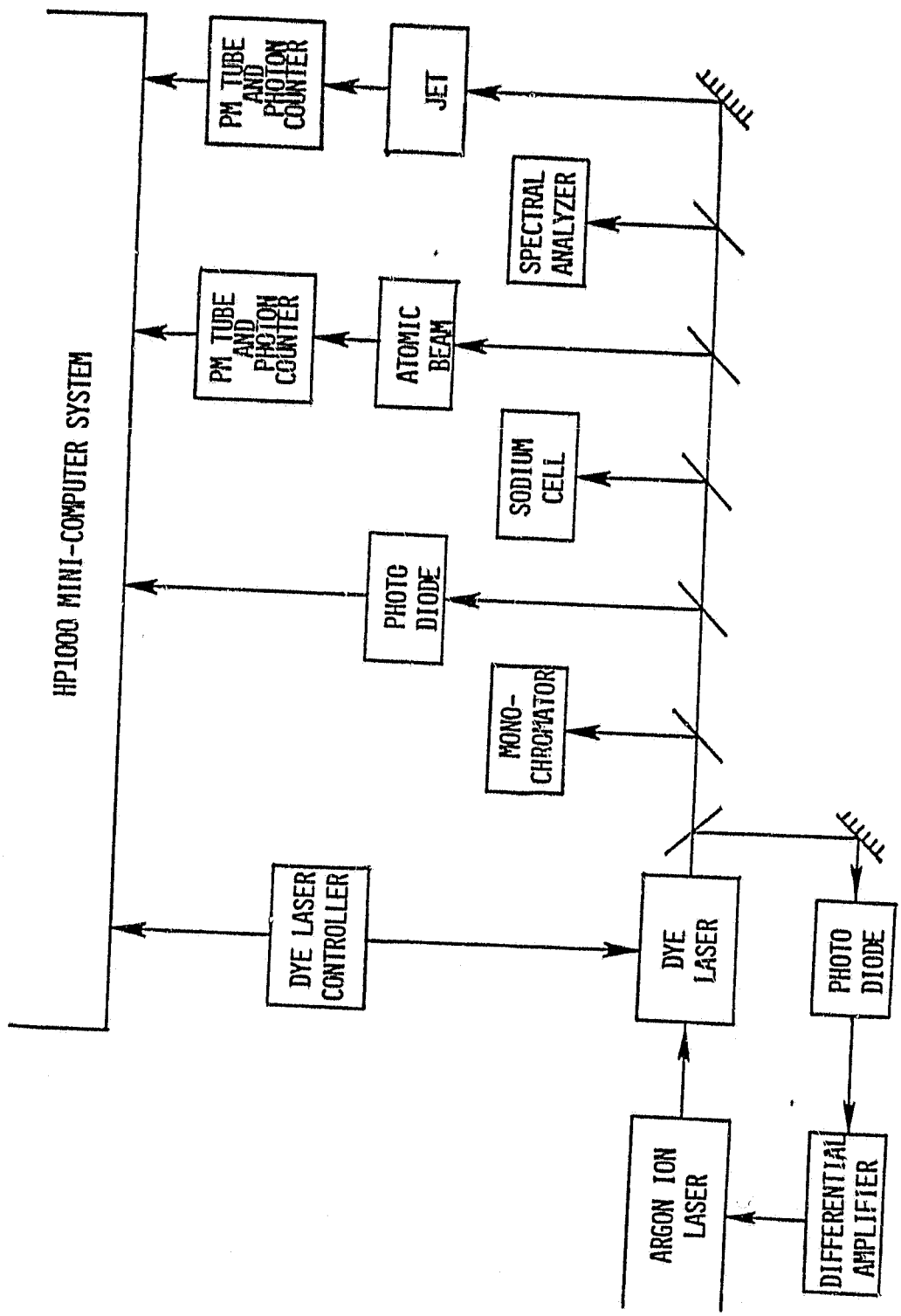

Figure 10: Schematic Diagram of the Optic System

complished with this device. In addition, a photodiode was used to detect the dye laser intensity.

A frequency reference was provided by an atomic beam device(Figure 11). At the bottom of the device, there was a small piece of pure sodium electrically heated to about 140°C. The vaporized sodium atoms were collimated by two pinholes. The downstream side of the pinholes was evacuated by a Vactronic Econovac model 20 diffusion pump until the pressure measured with a Norton Vacuum Equipment model NRC831 ion gauge(using a NRC507 tube) was about 2×10^{-6} torr. Since the atomic beam was highly collimated, the static temperature there was extremely low. With such a low temperature and low pressure, the spectral line is very narrow. The dye laser light was then shone perpendicular to the atomic beam to elimate the Doppler shift. The narrow spectral lines serve as a good frequency reference. The fluorescence signal from the atomic beam was imaged by two lenses onto a thermo-electrically cooled RCA model C31034 photomultiplier tube which was positioned perpendicular to both the laser light and the atomic beam. The signal was further processed with a SSR 1120 amplifier-discriminator and a SSR 1110 photon counter.

The remaining laser light was directed at an angle into the nitrogen jet. The fluorescence signal was detected by signal collection optics which were positioned perpendicular to the plane formed by the jet and the laser light. Before

Figure 11: Schematic Diagram of the Atomic Beam Device

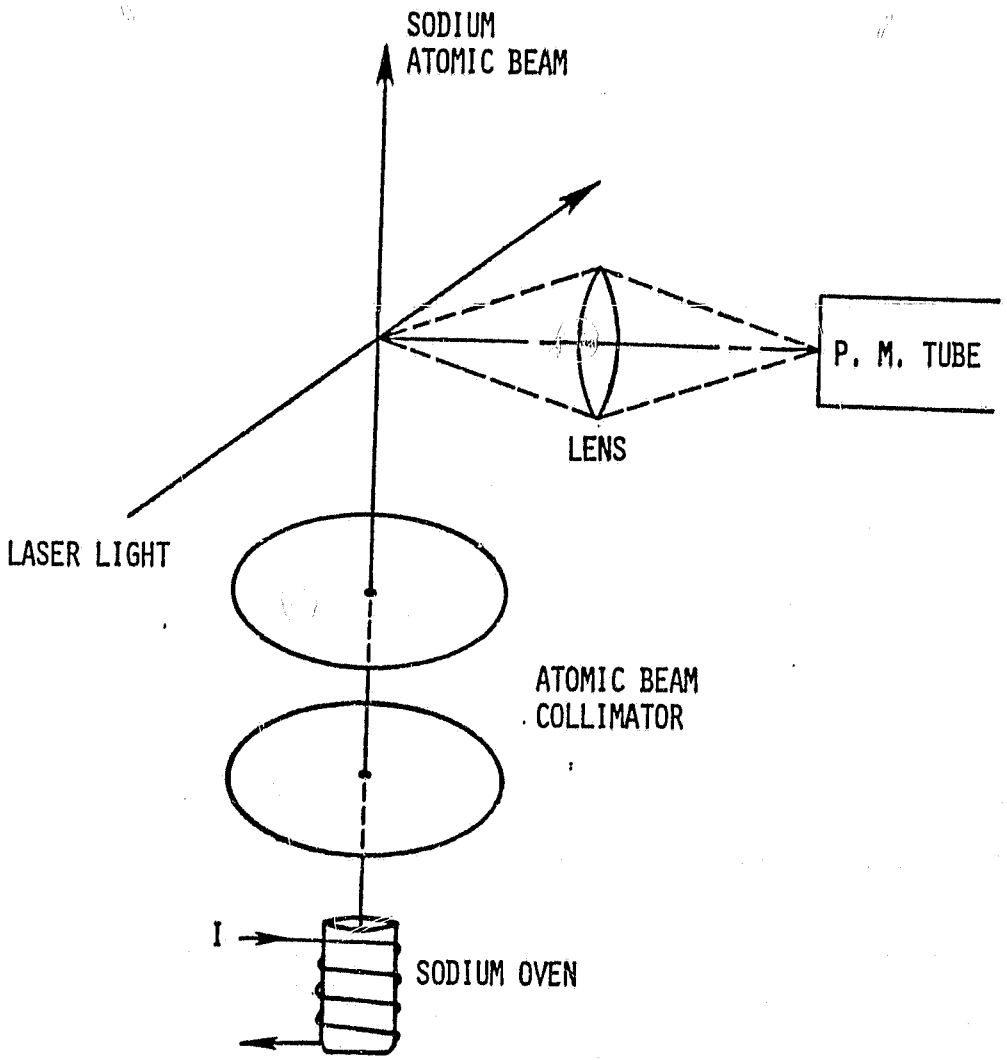

the laser beam was directed into the tunnel, it went through a translational-tracking optical system so that the laser beam movement tracked the movement of the signal collecting optics(6).

The signal collection optics are shown in Figure 12. The signal collected by lens L1 was spatially filtered by a circular aperture of 0.343 mm diameter. Then the signal was collimated and passed through a Corion SS5300 optical frequency filter. The spatially and frequency filtered signal was focused by lens L3 onto a RCA C31034-02 GaAs photomultiplier, which was thermo-electrically cooled and had a response time of 2 nsec. The spatial resolution of the system was determined by the aperture size and the laser beam diameter. Some parameters of the signal-collecting optics are tabulated in Table 5, using the assumption that the laser beam diameter is 2 mm.

The photomultiplier signal was preamplified and discriminated by an EG&G/PAR model 1120 amplifier-discriminator and then processed by an EG&G/PAR model 1109 photon counter. The photon counting improves the signal-to-noise ratio.

3.3 THE DATA ACQUISITION SYSTEM

Nine channels of data were sent to a Hewlett Packard 1000 mini-computer system. Five of these channels were connected to a 14 bit Preston model GMAD4 A/D converter which has a fixed total sampling rate of 1750 Hz and samples sequentially. These five channels were

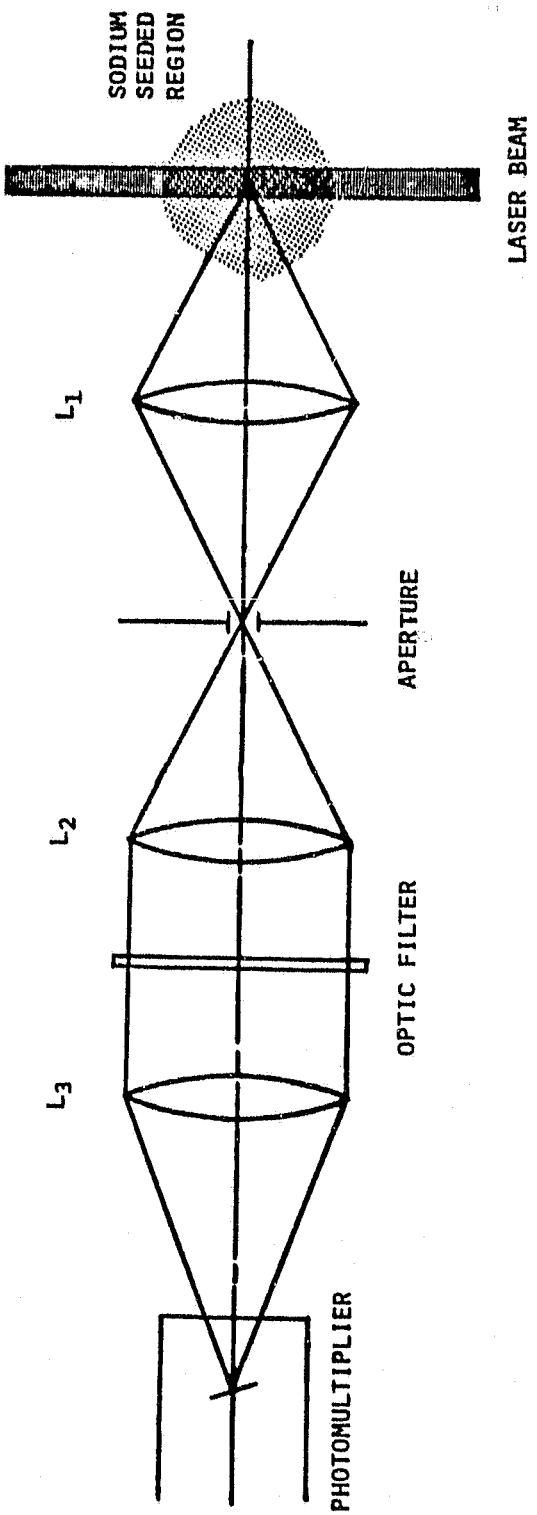

Figure 12: Signal Collecting Optics

TABLE 5

Parameters of the Signal Collecting Optics

Aperture size(mm)	0.34
Laser beam diameter(mm)	2.0
f number of the collecting lens	0.98
lens collection efficiency(%)	1.54
PM tube quantum efficiency(%)	23.23

1. position of the probe point translator
2. stagnation pressure
3. plenum chamber pressure
4. stagnation chamber temperature
5. jet temperature at nozzle exit

These supplementary information was sampled only at the beginning and at the end of each data set.

The other four channels were

1. the voltage ramp applied to the piezo-electric crystal which was attached to one of the end mirrors in the cavity
2. the dye laser intensity monitored by the photodiode
3. the output of the photon counter(a) which counts the photons of the fluorescence signal from the atomic beam device
4. the output of the photon counter(b) which counts the photons of the fluorescence signal from the jet

These four channels were sampled simultaneously through the Preston model GMAD/1 A/D converter which has a maximum sampling rate of 500 KHz. The data acquisition scheme is shown in Figure 13. First, the computer sends out a pulse and commands the photon counters to count. The photon counters count the photons collected by the photomultipliers for a time period set by the photon counter. At the end of the counting period, the photon counter sends a pulse back to the computer to inform the computer that the data are ready. Then the computer samples the four channels of data and stores them on a magnetic tape. At the same time, a pulse is sent to a pulse counter. The pulse counter counts one, and moves the dye laser one frequency step. Then, the computer sends another pulse, and the whole process starts again. Two hundred and fifty six frequency steps were used for each frequency scan.

The raw data sampled by this scheme are shown in Figure 14. As one can easily see, the sodium frequency spectrum from the jet is much broader than that from the atomic beam device. The shift in the frequency, which is caused by Doppler shift and pressure shift, is very obvious. The voltage ramp can be converted into laser frequency through the calibration process described in the next chapter. The laser intensity is used to normalize the sodium spectrum when the raw data are processed.

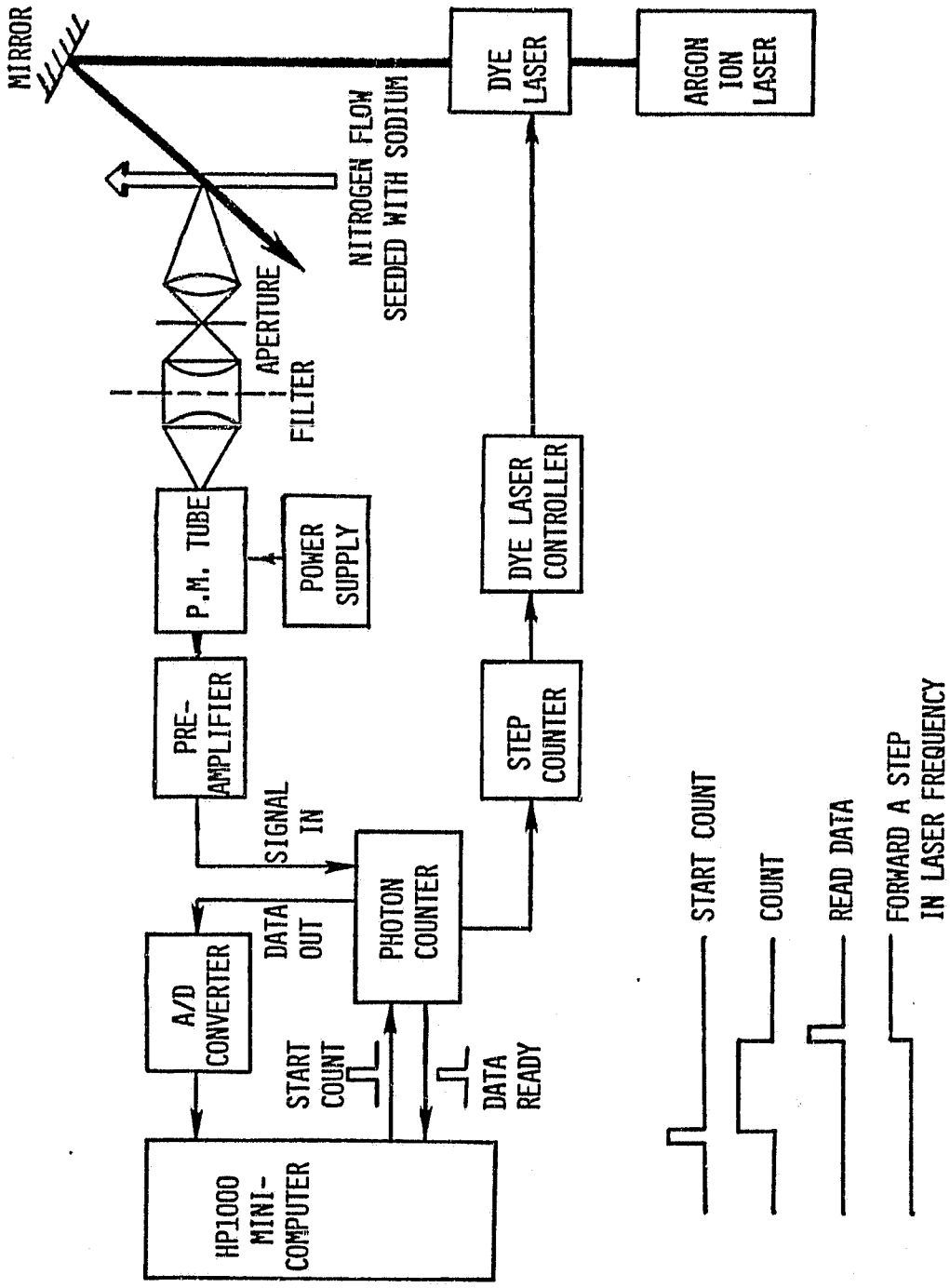

Figure 13: Data Acquisition Scheme

Figure 14: Raw Data Sampled by the Computer

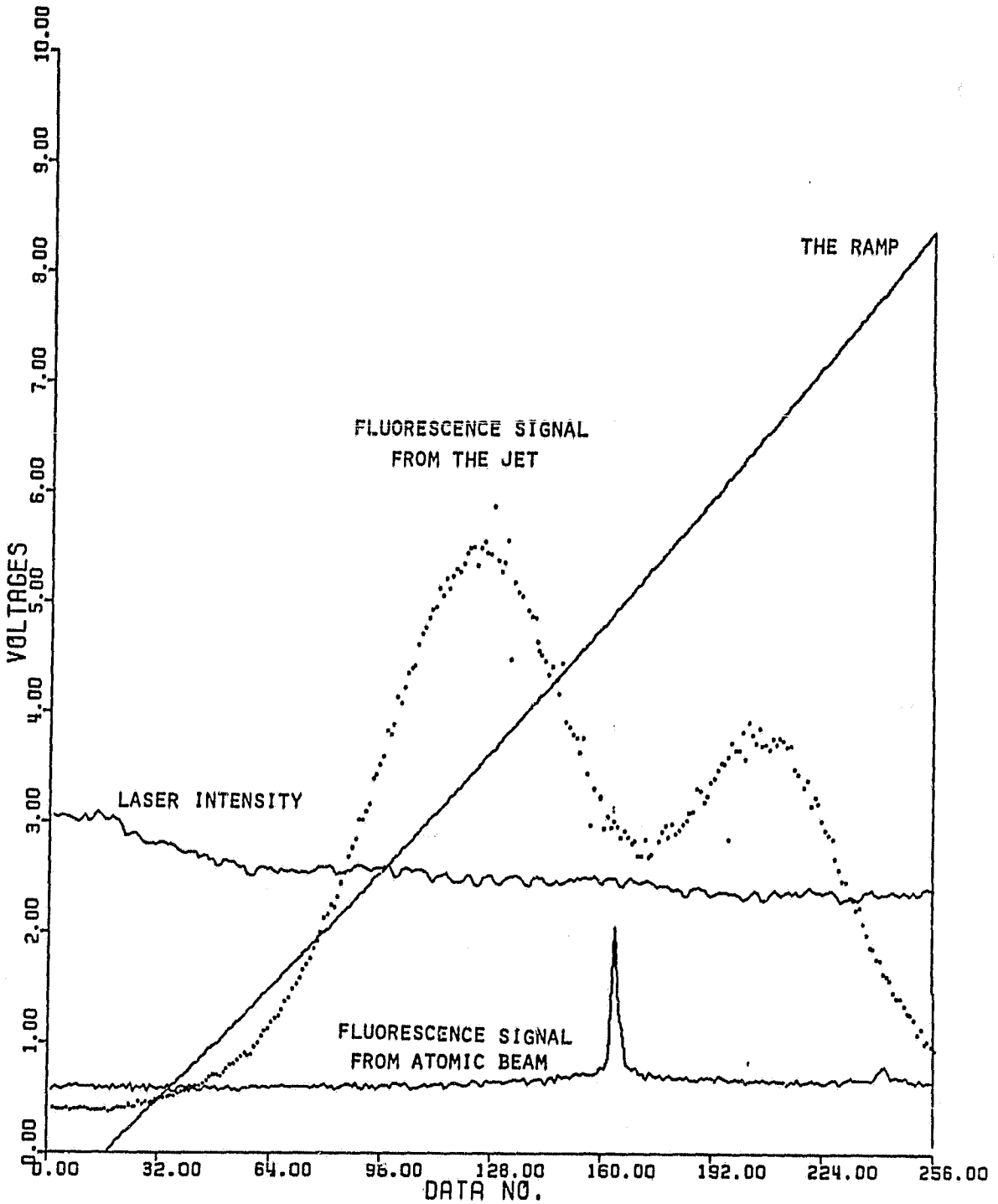

Chapter IV

EXPERIMENTAL PROCEDURE AND DATA PROCESSING

In this chapter, the frequency calibration procedure and the methods of the data analysis are presented. They are presented in largely the same sequence that the experiments were conducted.

4.1 LASER FREQUENCY CALIBRATION

For the RDV technique, all the information is extracted from the parameters in the form of frequency, e.g., Doppler shift and linewidth. Hence an accurate frequency scale is vital. The laser frequency is not measured directly. It is deduced from the voltage which is applied to a piezo-electric crystal attached to one of the end mirrors in the laser cavity. Since the frequency-voltage relation is nonlinear, it has to be calibrated. The calibration was accomplished by using the Jodon spectral analyzer. Since this spectral analyzer had a free spectral range of 1500 MHz, we got 3 peaks across the 5 GHz dye laser frequency scanning range. To make the calibration more reliable, the dye laser was run simultaneously at two frequency modes. Figure 15 shows the voltage ramp and the output of the spectral analyzer. Similar scans were made more than 20 times, and the accumulated

calibration values were fitted with a second-order polynomial. The fitted result is shown in Figure 16.

4.2 COLLISION CROSS SECTIONS

As described in the introduction, one of the major differences between the nitrogen-sodium system and the helium-sodium system is that the pressure shift is not negligible. Therefore, to make the velocity measurements meaningful, we need the pressure shift cross section for collisions between sodium atoms and nitrogen molecules. Similarly, we need information on the broadening cross sections to calculate the pressure. Unfortunately, the necessary cross sections are not available in the literature. Table 6 lists the broadening and shift cross sections that are available from the literature. Many of the measurements were done without the use of a tunable laser, which means these cross sections are not very reliable. Other more recent measurements were measured under the flame condition. As was mentioned in Chapter II, these cross sections are temperature dependent. Therefore, we needed to find the broadening and shift cross sections which were appropriate for our low-temperature conditions. These cross sections were measured by shining the laser beam perpendicular to the nitrogen jet. In this way, there is a negligible Doppler shift caused by the mean flow motion. Any shift in the spectral line frequency is mainly from the pressure shift effect. The plenum chamber pressure

Figure 15: Laser Frequency Calibration

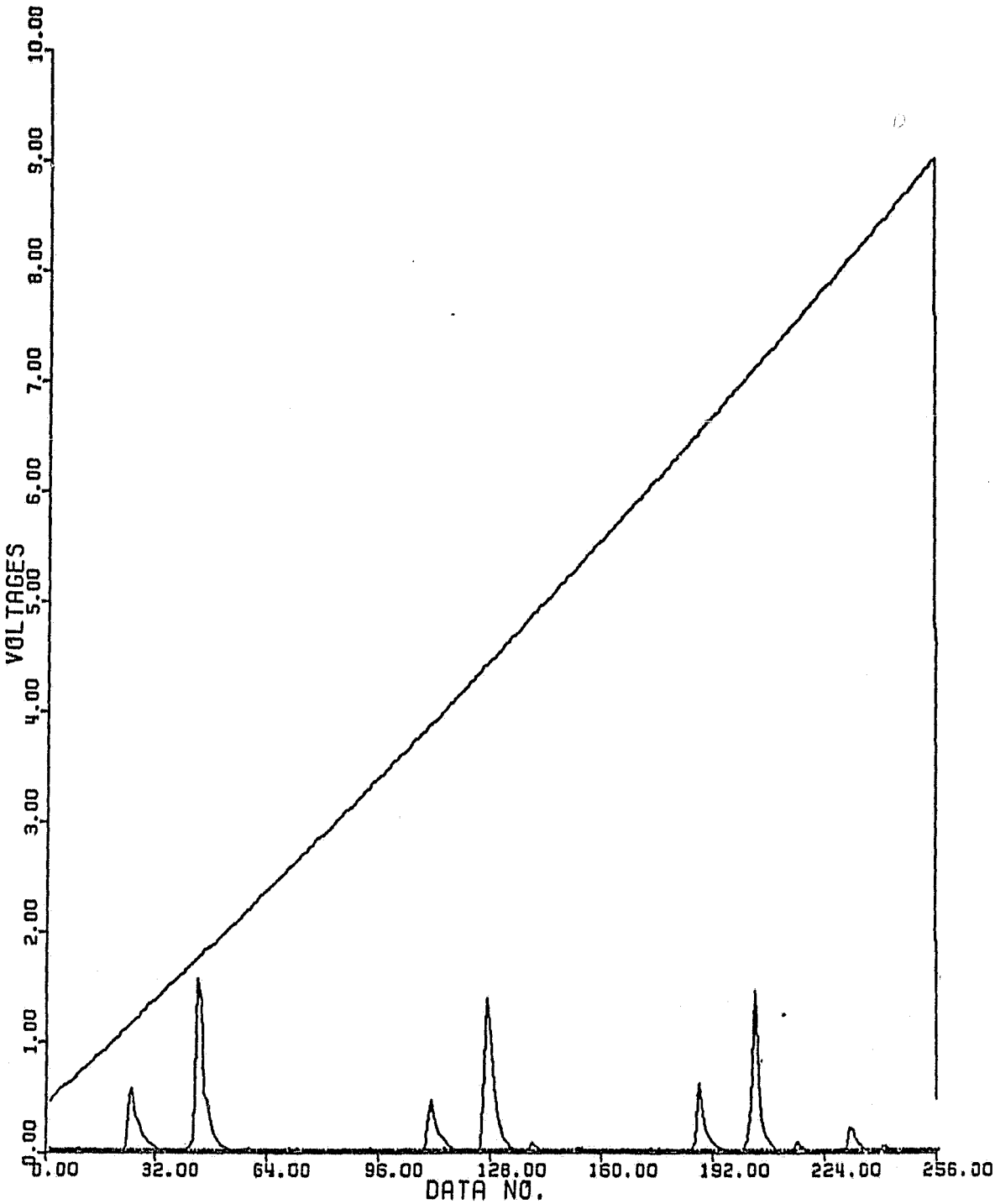

Figure 16: Fitted Laser Frequency Calibration Curve

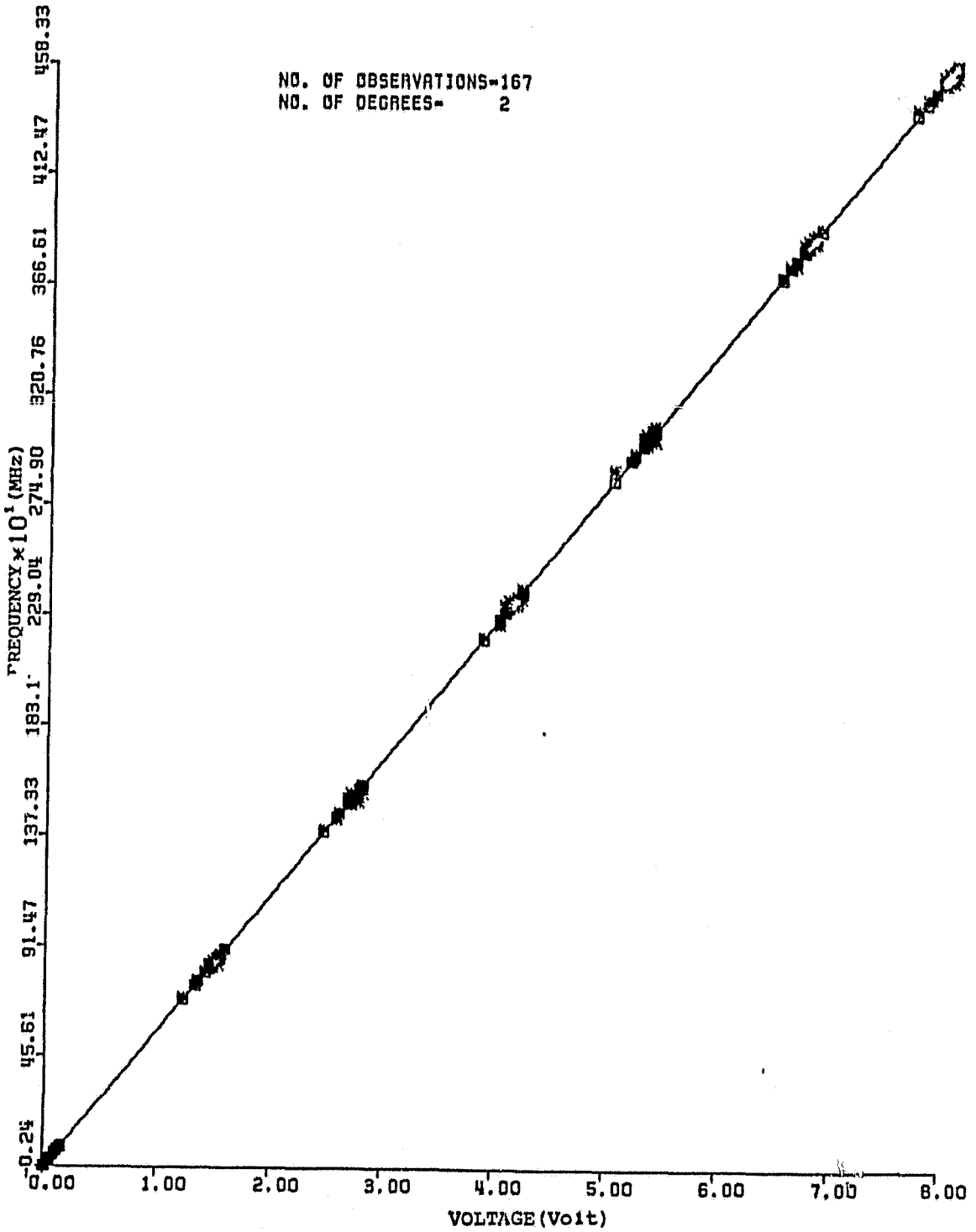

was adjusted by adjusting the needle valve at the downstream side of the plenum chamber until uniform pitot pressure distributions at several different downstream distances from the nozzle in the core region of the jet were obtained. It was then believed that the jet was nearly ideally expanded, and a uniform static pressure distribution was assumed. Then the static pressure was determined by measuring the pitot pressure outside the jet. With this pressure and the temperature determined by the least squares curve fitting technique discussed in the next section, the pressure shift cross sections and pressure broadening cross sections were calculated from the following relationships which were derived from Equation II-1:

$$\sigma_b(\mathring{A}^2) = 6.6346 \times 10^{-4} \left(\frac{P_o}{P}\right) \sqrt{T}\, \Delta\nu_c$$

$$\sigma_s(\mathring{A}^2) = -6.6346 \times 10^{-4} \left(\frac{P_o}{P}\right) \sqrt{T}\, \Delta\nu_s$$

where P_o = 760 torr

$\Delta\nu_c$ = collisional linewidth(MHz)

$\Delta\nu_s$ = pressure shift(MHz)

T = static temperature (^oK)

The temperature dependence of these cross sections was obtained independently by moving the probe point across the jet since the static temperature distribution was not uniform across the jet. Results are presented in Chapter V.

TABLE 6

Broadening & Shift Cross Sections

Milieu	Temperature (^oK)	σ_b ($Å^2$)	σ_s ($Å^2$)	Reference
Vapour Bulb	<1000	59	--	(a)
Vapour Bulb	580	69	--	(b)
City Gas Flame	2080	33	--	(c)
Vapour Bulb	473	42	18.34	(d)
Air-C_2H_2 Flame	2500	85	--	(e)
Air-C_2H_2 Flame	2180	34	--	(f)
Air-C_2H_2 Flame	2500	59.3	--	(g)
Air-C_2H_2 Flame	2500	53.5	26.89	(h)
Air-CO Flame	1964	27	--	(i)
Air-CO Flame	2450	25	--	(i)
Air-CO Flame	2389	30	--	(i)
Vapour Bulb	580	83.2	--	(j)
H_2-O_2-N_2 Flame	2000	27.07	9.92	(k)
Vapour Bulb	500	38.57	12.26	(k)

(a) R. Minkowsky, Z Phys 36, 839 (1926).
(b) W. Schut, Z Phys 45, 30 (1927).
(c) E. F. M. van der Held, Z Phys 70, 508(1931).
(d) H. Margenau & W. W. Watson, Phys. Rev. 44, 92(1933).
(e) N. N. Sobolev, E. M. Metzheritscher & G. M. Rodin, Zh. Eksp., Teor. Fiz. 21, 350 (1951).
(f) C. Th. J. Alkemade, Thesis, Utrecht, (1954).
(g) F. W. Hofmann & H. Kohn, J. Opt. Soc. Amer., 51, 512 (1961).
(h) W. Behmenburg, H. Korn & M. Mailander, JQSRT 4, 149, 163 & 177 (1964).
(i) C. van Trig, Tj. Hollander & C. T. J. Alkemade, JQSRT 5, 813 (1965).
(j) K. G. Popov & V. P. Ruzov, Opt. Spectrosc.(USSR), 48, 4, 372 (1980).
(k) M. J. Jongerius, A. R. D. Van Bergen, Tj. Hollander & C. Th. J. Alkemade, JQSRT 25, 1 (1981).

4.3 DATA PROCESSING

After the cross sections, and their temperature dependences were determined, we proceeded to measure the flow properties in an ideally expanded jet, and in an underexpanded jet. Pitot probe measurements and total temperature surveys were also made for comparison.

The spectral lines obtained from the experiments were analyzed by a curve fitting technique. An IMSL(International Mathematical & Statistical Library) least-squares curve-fitting subroutine was used to do the curve fitting. The theoretical Voigt profile was provided by the Kielkopf approximation(50). Although there are many approximations to the Voigt function (51 - 60), the Kielkopf approximation is considered the best if accuracy, simplicity, and computing time are all taken into account(61).

Five parameters were used in the fitting process. These five parameters were

1. intensity normalization factor, I_1, which determines the intensity scale of the theoretical spectral line
2. the background intensity, I_o, which determines the base line
3. the Half Width at Half Maximum(HWHM) of the Voigt profile
4. the ratio of Lorentzian HWHM over Gaussian HWHM, a, which affects the spectral lineshape

5. the frequency of the $3^2S_{1/2}$, F=2 --> $3^2P_{3/2}$, F=1 transition, ν_{f_1}

From an initial guess at the values of these parameters, the Voigt profile for each of the six hyperfine lines can be calculated. Then, using the frequency spacings and intensity weighting factors shown in Figure 2, the sodium D_2 spectra can be constructed by superposing these six hyperfine lines. Then the IMSL subroutine will iterate until an acceptable fit is obtained. A typical fitted result is shown in Figure 17. The abscissa is the relative laser frequency in MHz and the ordinate is the fluorescence intensity in arbitrary units. The crosses in the figure represent the experimental data points. The solid line through the crosses is the least-squares fitted sodium D_2 line. The hyperfine structure is indicated by the vertical bars.

The IMSL least-squares curve-fitting subroutine also provides the uncertainties for the fitting parameters, which can be used to calculate the uncertainties of the measured quantities. These uncertainties are mainly due to laser frequency jitter, photon statistics, and electronic noise. Dark current of the photomultiplier is negligible in this investigation because a cooled PM tube housing, and a photon counter with a discriminator were used for the signal detection.

The goodness of the fit was tested by calculating the sum of squares of the residues and by drawing the histogram

Figure 17: Fitted Sodium Spectrum

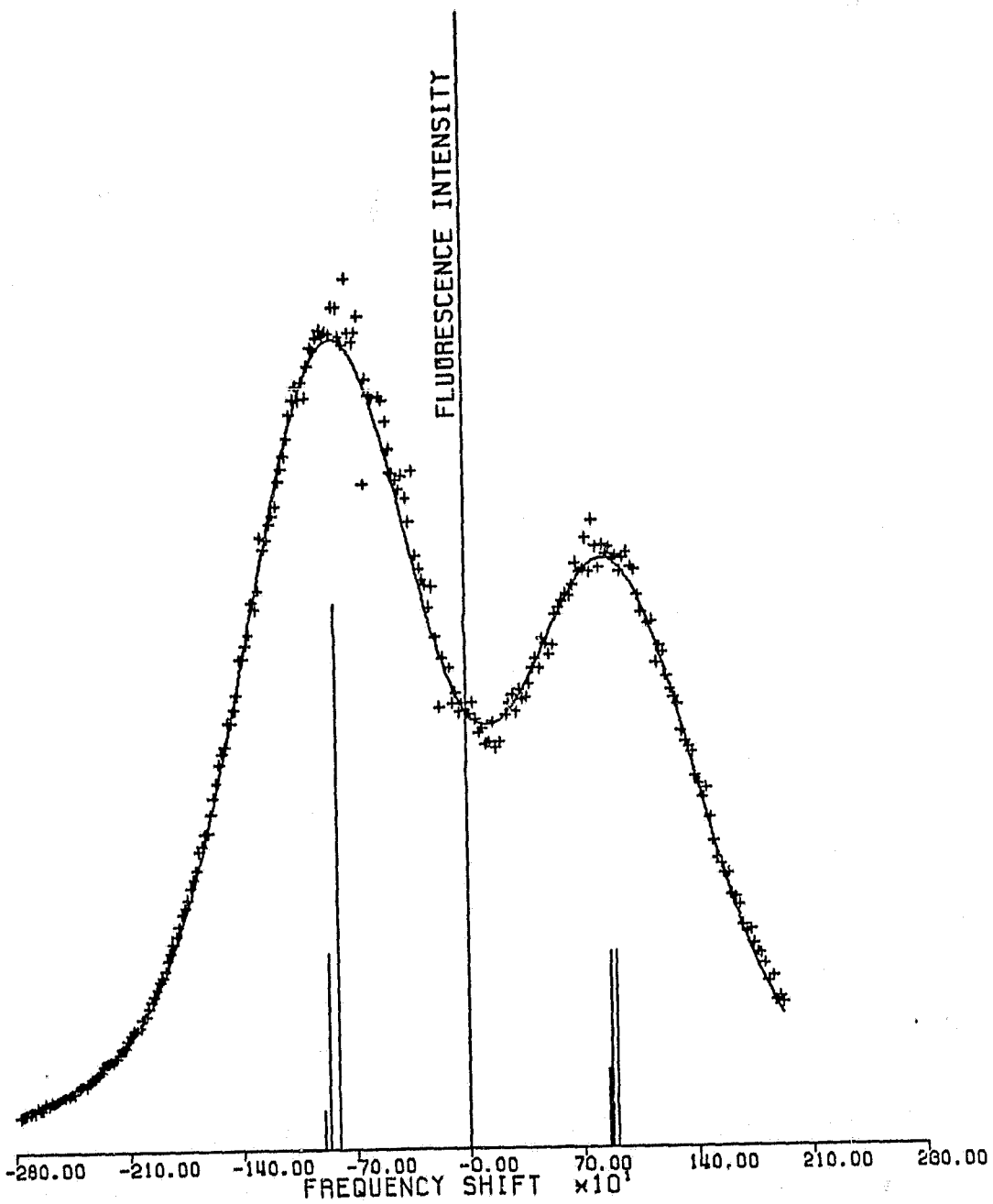

of the residues. Details of the error analysis can be found in Ref. 6, and the theory can be found elsewhere (63).

Once the spectrum has been fitted and the optimal fitting parameters have been established, we can calculate the flow properties. Since broadening and pressure shift cross sections are temperature dependent, the first flow property to be determined is the static temperature.

From Kielkopf's approximation, the Gaussian linewidth and Lorentzian linewidth can be calculated from the parameters a and HWHM by using the following relations:

$$\varepsilon = 0.099$$

$$\ell = \frac{2}{1+\varepsilon\ln 2+\sqrt{(1-\varepsilon\ln 2)^2+\frac{4\ln 2}{a^2}}}$$

$$g^2 = \frac{1-(1+\varepsilon\ln 2)\ell+\varepsilon\ln 2\cdot\ell^2}{\ln 2}$$

$$\Delta\nu_L = 2\cdot\ell\cdot \text{HWHM}$$

$$= 2\cdot g\cdot \text{HWHM}\cdot\sqrt{\ln 2}\cdot a$$

From Equation II-2, the temperature is given by

$$\Delta\nu_G = 7.16\times 10^{-7}\times\nu_o\sqrt{T/M}$$

$$= 75.7\sqrt{T} \quad (\text{MHz})$$

After the temperature is determined, the collision cross sections of the broadening and the shift can be determined.

Before determining the pressure, the collisional linewidth must be determined. As mentioned in Chapter II, there are many homogeneous line broadening mechanisms which will contribute to the Lorentzian linewidth. For the sodium-nitrogen system, only collisional broadening, natural broadening, and instrumental broadening need to be taken into account. Since the natural broadening and the instrumentaion broadening are much smaller than the Lorentzian linewidth, a simple subtraction is used here.

$$\Delta\nu_c = \Delta\nu_L - \Delta\nu_N - \Delta\nu_I$$

The instrumental broadening $\Delta\nu_I$ is mainly caused by laser jitter. It was estimated to be 10 MHz. The natural linewidth $\Delta\nu_N$ is shown in Table 1. We can now calculate the pressure.

The static pressure, P, is related to the collisional linewidth by

$$\begin{aligned}\Delta\nu_c &= 2N\sigma_b\bar{v}_{rel} \\ &= 2\cdot\frac{P}{\tilde{R}T}\cdot\sigma_b\cdot\sqrt{\frac{8\tilde{R}T}{\pi M^*}} \\ &= 6.029\times10^3\left(\frac{P}{P_o}\right)\cdot\sigma_b\cdot\frac{1}{\sqrt{T}} \qquad \text{(MHz)}\end{aligned}$$

where P_o = 760 torr

$\tilde{R}$ = universal gas constant

Thus,

$$P = (6.6346\times10^{-4})\Delta\nu_c P_o\sqrt{T}/\sigma_b \qquad \text{(torr)}$$

To calculate the velocity, we need the frequency shift of the sodium D_2 line. This can be calculated from

$$\Delta\nu_f = \nu_{f_1} - \nu_{ref}$$

where ν_{ref} is the reference frequency of $3^2S_{1/2}$, F=2 to $3^2P_{3/2}$, F=1 transition. This reference frequency can be obtained from the position of the large spike in the atomic beam spectrum. The velocity component, U_z, in the laser beam direction can be found from

$$U_z = \frac{C}{\nu_o}(\Delta\nu_f - \Delta\nu_s)$$

where $\Delta\nu_s$(MHz) = pressure shift

$$= -6.029\times 10^3(\frac{P}{P_o})\sigma_s\cdot\frac{1}{\sqrt{T}} \qquad \text{(IV-4)}$$

If the angle between the probing laser beam and the axis of the jet is known, the flow velocity in the direction of the jet is given by

$$U = U_z/\cos\theta$$

The Mach number can be determined from the relation:

$$M = U/\sqrt{\gamma RT}$$

where R = specific gas constant

Also, the total temperature can be found from:

$$T^t = T + U^2/2C_p \qquad \text{(IV-5)}$$

where C_p = specific heat at constant pressure

Uncertainties for these derived variables were determined by applying Kline and McClintock's expression(64):

$$\text{if } Y = Y(x_1, x_2, x_3, \ldots, x_N),$$

$$\text{then } \frac{\Delta Y}{Y} = \left\{ \sum_{i=1}^{N} \left(\frac{\partial \ln Y}{\partial \ln x_i} \cdot \frac{\Delta x_i}{x_i} \right)^2 \right\}^{1/2}$$

4.4 PITOT SURVEY AND TOTAL TEMPERATURE PROBE

To compare the result obtained from the RDV with some conventional measurement techniques, a pitot survey and a total temperature probe were used in the same jet. Since the flow is supersonic, a bow shock forms in front of the probe. Thus the pitot pressure is smaller than the stagnation pressure. If the jet is perfectly expanded, there should not be any loss in total pressure except for the losses associated with the pitot shock mentioned above. The flow Mach number can then be determined from the normal shock relations(65):

$$\frac{P_{pitot}}{P_{stag}} = \left\{1+\frac{2\gamma}{\gamma+1}(M^2-1)\right\}^{-\frac{1}{\gamma-1}} \left\{\frac{(\gamma+1)M^2}{(\gamma-1)M^2+2}\right\}^{\frac{\gamma}{\gamma-1}}$$

However, since the nozzle is a conical nozzle, the flow in the jet at the exit of the nozzle is not parallel to the center line of the nozzle, some waves and shocks always exist(67). Thus the total pressure at the nozzle exit does

not equal to the stagnation pressure, and the flow properties must be derived from the local static pressure. The Rayleigh supersonic pitot formula can then be used to calculate the Mach number:

$$\frac{P_{static}}{P_{pitot}} = \frac{\left(\frac{2\gamma}{\gamma+1} M^2 - \frac{\gamma-1}{\gamma+1}\right)^{\frac{1}{\gamma-1}}}{\left(\frac{\gamma+1}{2} M^2\right)^{\frac{\gamma}{\gamma-1}}} \qquad \text{(IV-6)}$$

This is the equation which was used in this work for an ideally (in fact nearly ideally) expanded jet. In the perfectly expanded jet, the static pressure is uniformly distributed throughout the jet. Outside the jet, the flow velocity is virtually zero. Therefore, it is assumed that the static pressure is the same as the pitot pressure measured there. The error introduced by this assumption will be discussed in Chapter V. From this pressure and those pitot pressures measured in the jet, the Mach number across the jet can be determined by a numerical bisection scheme.

Since total temperature is not affected by the existence of the shocks or waves, it can be measured with an independent total temperature survey. Then the static temperature can be determined from the Mach number deduced above and the total temperature measured by the total temperature probe:

$$\frac{T_{static}}{T_{total}} = \left(1 + \frac{\gamma-1}{2} M^2\right)^{-1} \qquad \text{(IV-7)}$$

However, the total temperature is not a constant across the jet. Some errors are introduced by using a constant total temperature across the jet. These errors will be discussed in the next chapter.

The velocity can be derived from the definition of the Mach number:

$$U = Ma_o = M\sqrt{\gamma RT_{static}}$$

$$= U_{ulti}\Big/\sqrt{1+\frac{2}{(\gamma-1)\mu^2}} \qquad \text{(IV-8)}$$

where a_o = speed of sound

U_{ulti} = ultimate velocity $= \sqrt{\gamma RT_{total}}\Big/\sqrt{(\gamma-1)/2}$

A similar scheme will not work when the jet is underexpanded because the static pressure is not uniformly distributed across the jet. In that case the static pressure must be measured by a static pressure probe. However, for the small jet that we have, reliable measurements of static pressure are very difficult to conduct. Therefore, only a qualitative analysis is given in this work for the underexpanded case.

One point should be mentioned about the total temperature probe. Since the nitrogen gas has a Prandtle number less than one, the temperature measured by the total temperature probe is always smaller than the stagnation temperature. Therefore, a recovery coefficient must be used to compensate this effect. Here a constant recovery ratio of 0.95 is used(68).

4.5 TURBULENCE MEASUREMENT

To demonstrate that the RDV can be applied to turbulence measurements, the photomultiplier in the signal collecting system was operated in the voltage mode. After being amplified and frequency-filtered, the signal was digitized by the GMAD/1. The laser intensity was sampled simultaneously along with the fluorescence signal. In each data set, more than 32000 data points were sampled for each channel. The frequency spectrum of these data was obtained through Fast Fourier Transformation(FFT). The frequency spectrum of the fluorescence signal was compared with that of the laser intensity to check the effect of laser intensity fluctuation. Afterwards, they were compared with the power spectrum obtained with hot wire probe in the same flow.

The hot wire system that we used was a DISA 55M01 system. The sensor was a 5 μm tungsten wire. The wire length was 2 mm. Various overheat ratios (defined in Appendix B) were used, but most of the measurements were done with $\tau = 0.78$. This is the highest overheat ratio that can be operated in our flow before the tungsten wire starts to be oxidized.

Turbulence measurements with a hot-wire anemometer are difficult because the voltage fluctuations need to be resolved into individual flow property fluctuations. To solve this problem, the sensitivity coefficients must be found by

calibration procedure. Then, by applying different overheat ratios to the hot wire, one may separate the total fluctuations into fluctuations of mass flux and temperature(96).

In the RDV, the same problem can be solved by calculating the sensitivity curves from the spectral profile. Since the velocity will determine the frequency shift of the spectral line, and the pressure and the temperature will each affect the Lorentzian and Gaussian lineshapes, their sensitivities are different at different laser frequencies:

$$I'_\nu = S_V V' + S_T T' + S_P P' + \text{higher order terms} \qquad \text{(IV-9)}$$

where $S_V = (\partial I_\nu / \partial V)_{P,T}$

$S_T = (\partial I_\nu / \partial T)_{V,P}$

$S_P = (\partial I_\nu / \partial P)_{V,T}$

For low turbulence fluctuations, the higher order terms can be neglected. Since S_V, S_T, and S_P are functions of the laser frequency, they are presented as velocity, temperature, and pressure sensitivity curves in Figures 18 - 20. In each of these figures, curves for different Lorentzian-to-Gaussian linewidth ratios are presented. The a=0.227 curves apply for our conditions. The frequency scales were normalized by the half width at half maximum of the spectral line, and the reference zero correspond to the strongest hyperfine line of the sodium D_2 line. As the figures indicate, the velocity fluctuations are most sensitive at the half maximum point, while the temperature and pressure fluc-

tuations are most sensitive at the peaks. Thus, by changing the laser frequency, different turbulence properties may be highlighted. One important feature of the velocity sensitivity curve is that there are three zero crossing points across the sodium spectra. They correspond to the three extremes in the sodium D_2 line. This unique character can be used to identify the existence of velocity fluctuations in the flow. Alternatively, the fluctuations may be separated by saturating the spectral line. In that case the only flow parameter that will affect the fluorescence intensity is the density(79,80). However, when a high laser intensity is used, optical pumping plays a role in determining the spectral line shape. Further investigation is needed if this option is to be employed.

4.6 FLOW VISUALIZATION

For the flow visualization, a cylindrical beam expander was used to expand the laser beam into a thin sheet of light. This thin light sheet was directed at a small angle to the jet(see Figure 21). The orientation of the light sheet was adjusted so that it went through the center of the nozzle. When the jet was nearly ideally expanded, the fluorescence intensity was more or less uniformly distributed. When the jet was underexpanded, the fluorescence intensity was not distributed uniformly, and a diamond-shaped structure could be easily recognized from the light pattern.

Figure 18: Velocity Sensitivity Coefficient as a Function of Laser Frequency

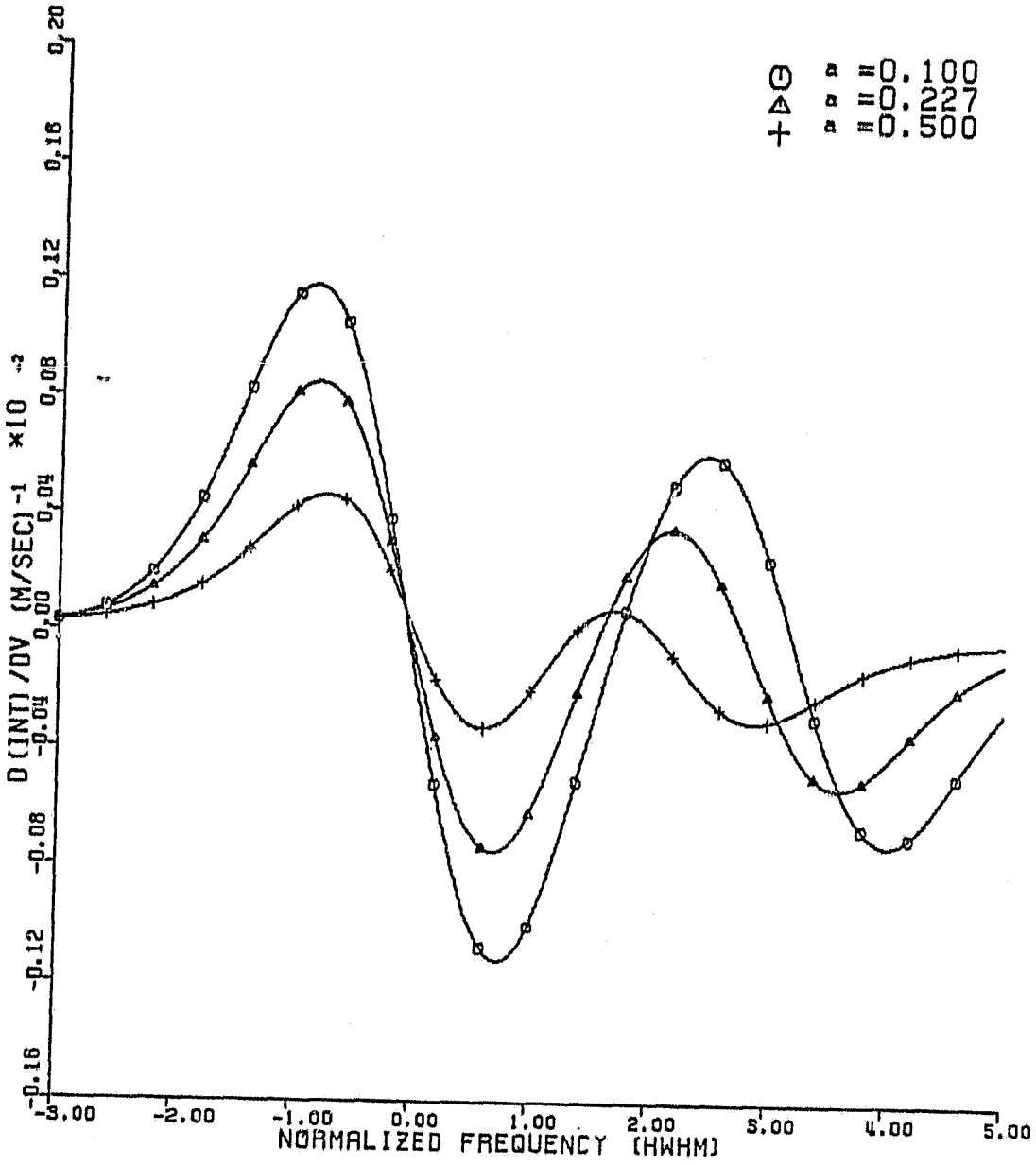

Figure 19: Temperature Sensitivity Coefficient as a Function of Laser Frequency

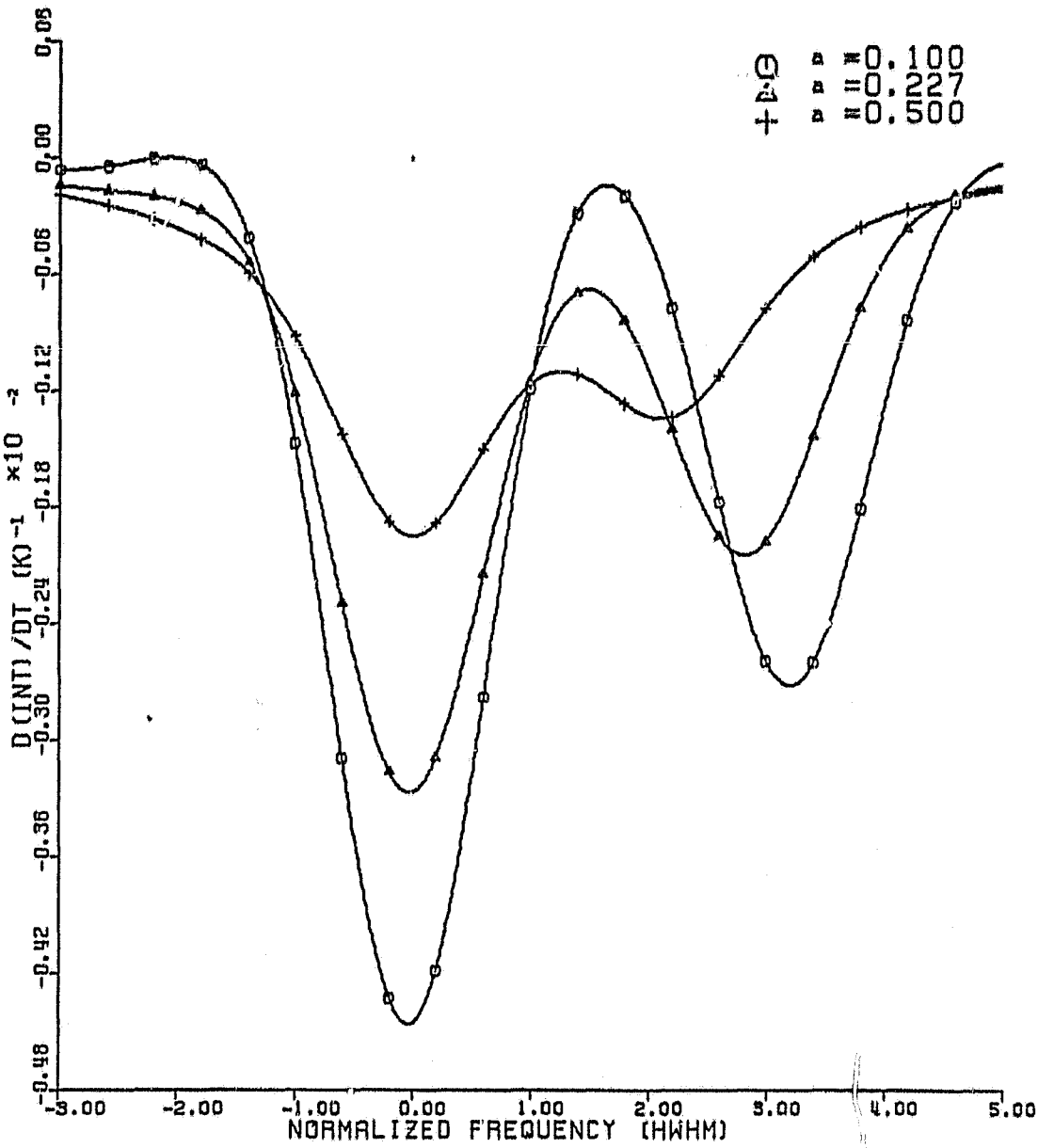

Figure 20: Pressure Sensitivity Coefficient as a Function of Laser Frequency

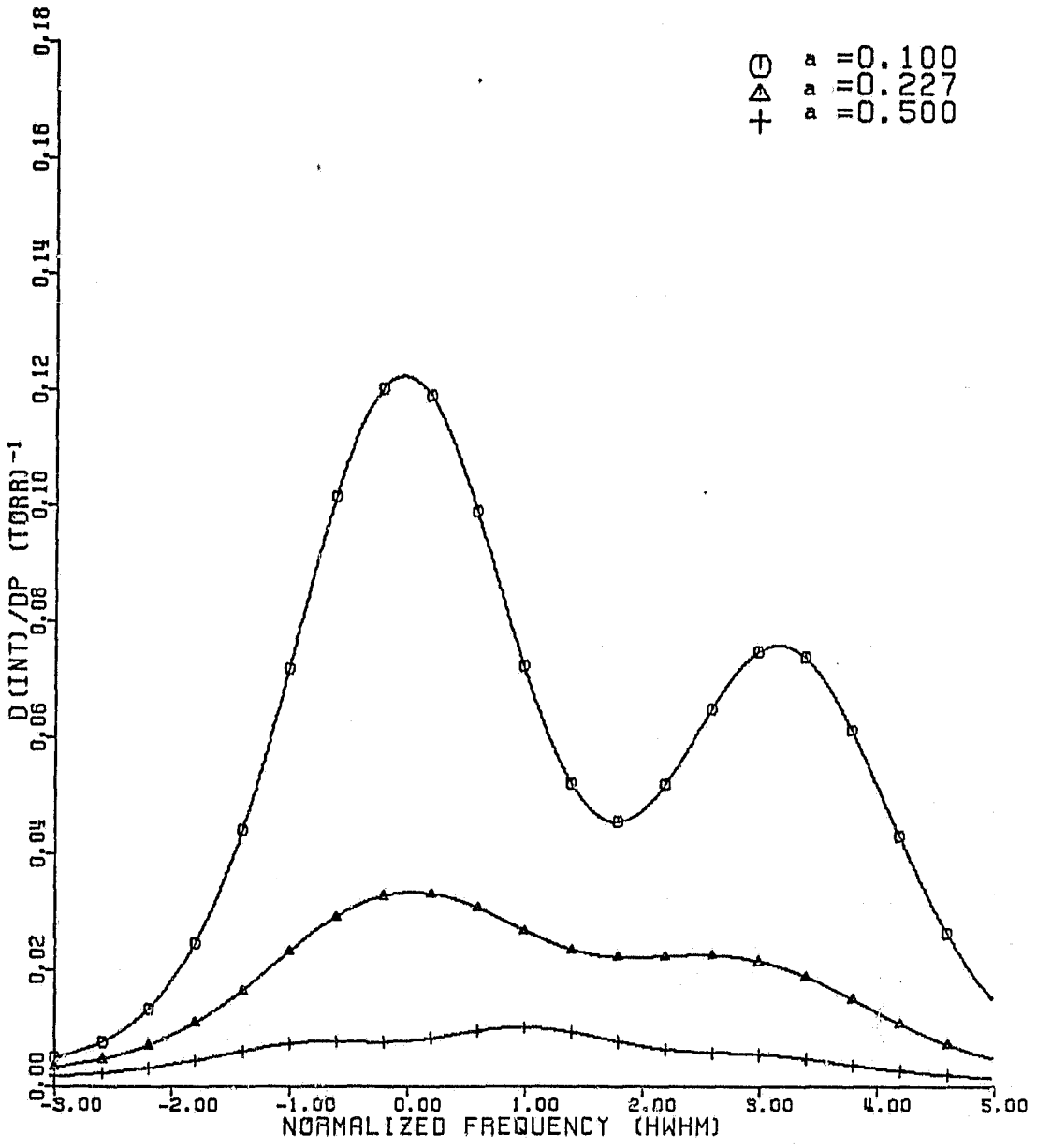

This pattern was photographed by a camera at the photomultiplier position. Then the laser light was directed into the jet from the side window at a large angle to the flow. In this way, an asymmetrical-structured pattern emerged due to the asymmetry of the illumination direction. Some photographs of these patterns are presented in the next chapter.

Figure 21: Laser Light Sheet & Diamond Shaped Structure

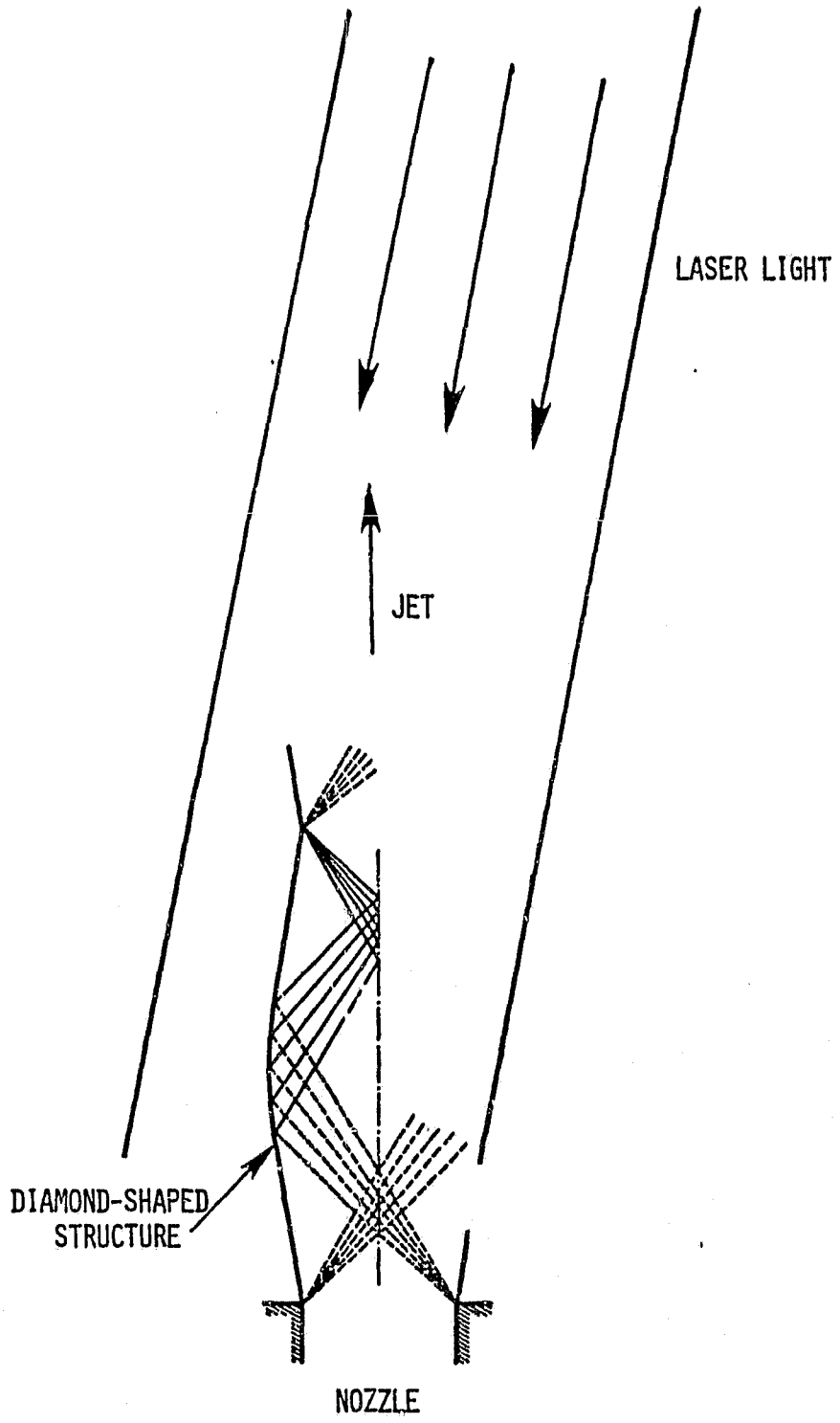

Chapter V

RESULTS AND DISCUSSION

The experimental results are grouped into four parts: cross section measurements, mean flow property measurements, turbulence measurements, and flow visualization. Comparison of the results of the RDV measurements with those of the conventional techniques are also made.

5.1 CROSS SECTION MEASUREMENTS

5.1.1 Broadening Cross Sections

As discussed in Chapter VI, the collision cross sections are determined by shining a laser beam perpendicular to the jet. Figure 22 shows the broadening cross sections obtained in this way. Those cross sections shown in Table 6 are also presented in the same figure. The solid curve is found by least squares fitting our data to the expression

$$\sigma_b = K_b T^{\alpha}$$

Our data correlate well with those cross sections measured after 1965. The temperature scaling of $\alpha = -0.30 \pm 0.05$ indicates that the interaction between the sodium atoms and nitrogen molecules is stronger than van der Waals interaction, and weaker than quadratic Stark interaction(see Appen-

Figure 22: Broadening Cross Sections

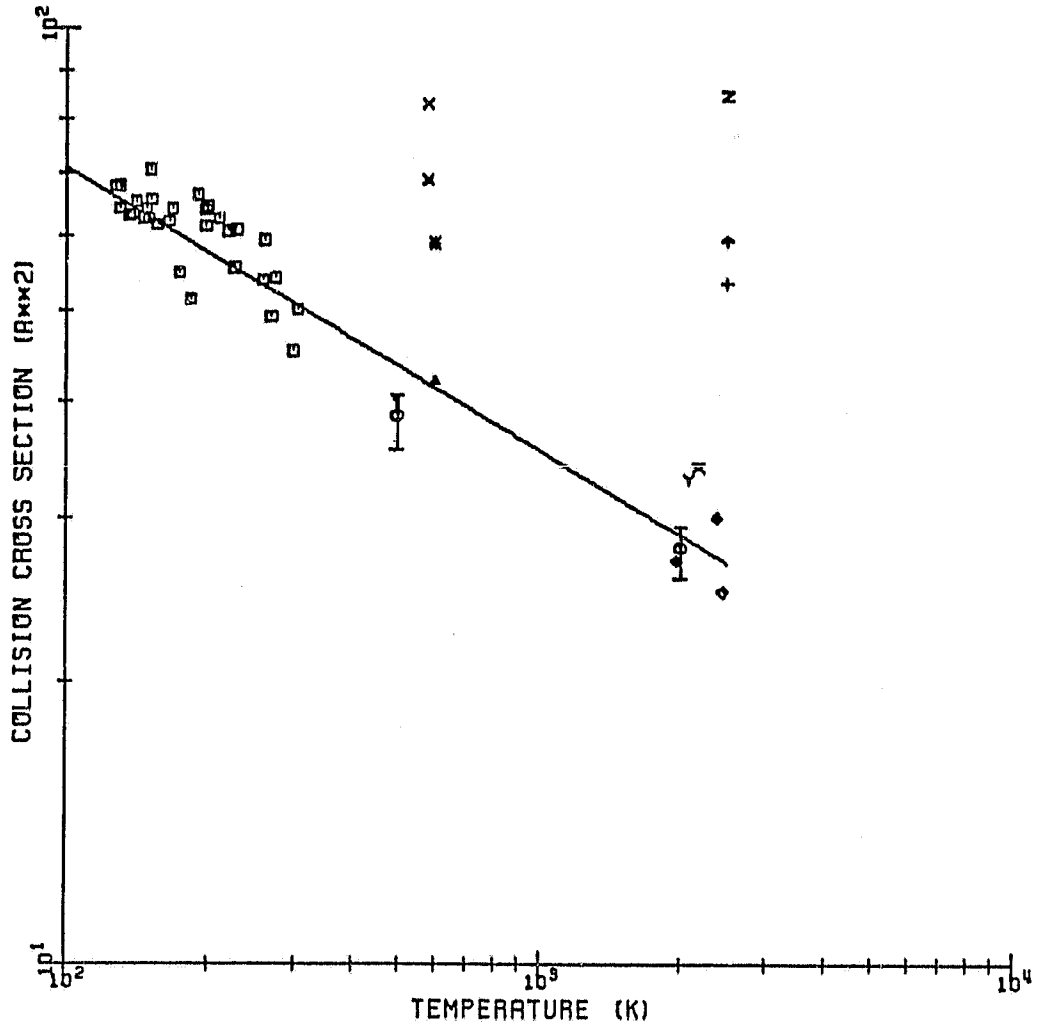

□ CHENG, ZIMMERMANN, & MILES (1982)
○ JONGERIUS, ETC. (1981)
△ POPOV & RUZOV (1980)
+ BEHMENBURG, KORN & MAILANDER (1964)
X MARGENAU & WATSON (1933)
◇ TRIG, HOLLANDER & ALKEMADE (1965)
◆ HOFMANN & KORN (1961)
⋈ ALKEMADE (1954)
N SOBOLEV, METZHERITSCHER & RODIN (1951)
Y HELD (1931)
¤ SCHUT (1927)
* MINKOWSKY (1926)

dix D). If the intermolecular potential is approximated by an inverse power law, the inverse power can be calculated from (Equation D-1):

$$N = 1 - 1/\alpha = 4.31 \pm 0.65$$

The broadening cross sections vary substantially with temperature at low temperatures. At 150°K, the velocity averaged broadening cross section is 70.65 ± 4.15 Å^2. At 250°K, it is 53.82 ± 8.31 Å^2. The much larger uncertainty at 250°K occurs because, as the temperature goes up, the spectral linewidth becomes large. Since the scanning range of the laser frequency is fixed, the uncertainty of the measurement will increase as the spectral linewidth increases.

5.1.2 Pressure Shift Cross Sections

The measurements of pressure shift cross sections are shown in Figure 23. Similar to the case of the broadening cross sections, these data were fitted with power law for the temperature dependence:

$$\sigma_s = K_s T^{\beta}$$

The curve fitting of our data gives $\beta = -1.10 \pm 0.27$. If one derives this temperature dependence from the N obtained above according to the theory in Appendix D, one obtains $\beta = -0.95$. This value is within the uncertainty of the experimental value. Comparing these cross sections with the

Figure 23: Pressure Shift Cross Section

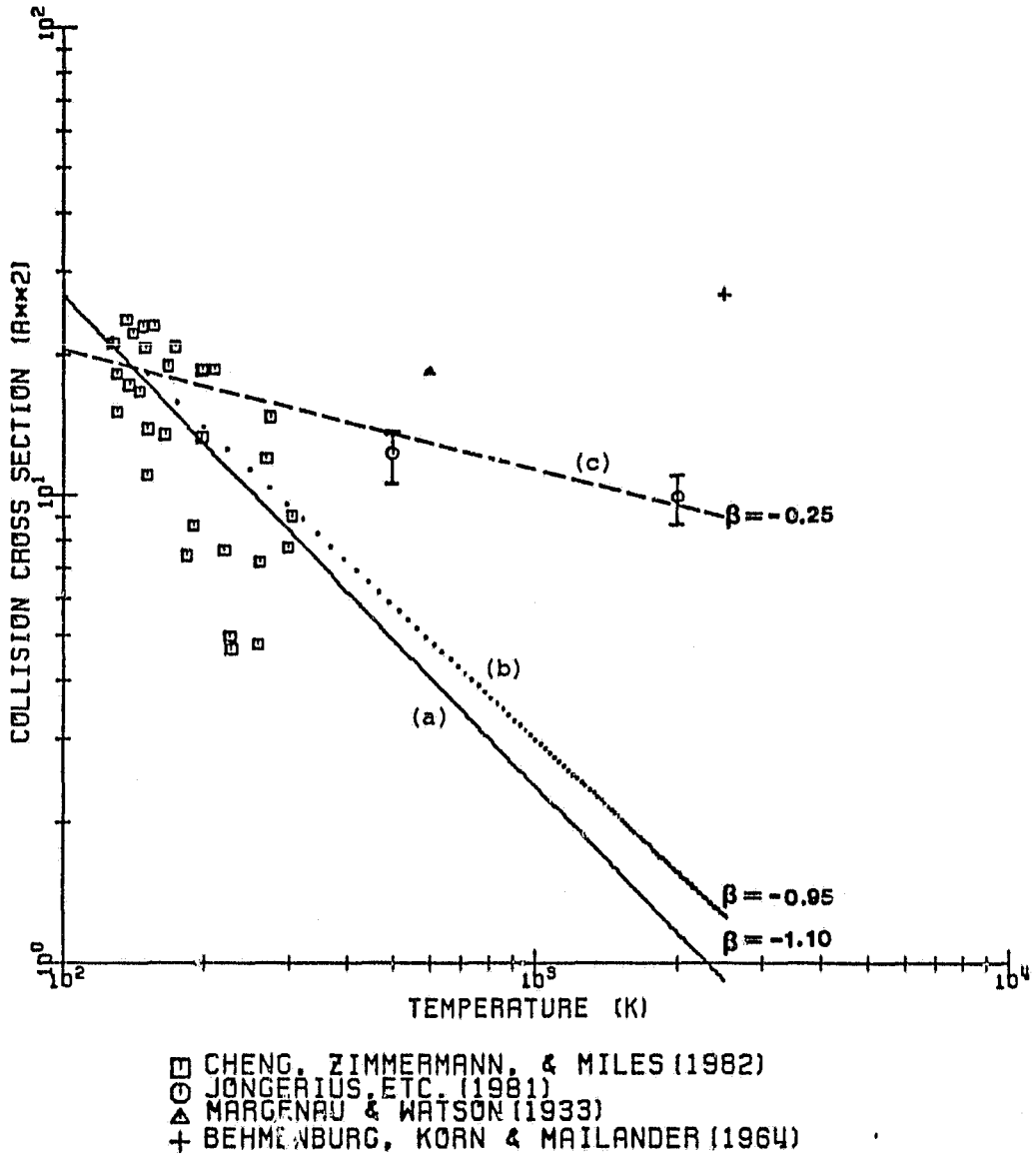

high temperature ones from the literature indicates that the temperature dependence of these cross sections is too strong. If our data points with temperature lower than 170°K, which have relatively low uncertainty, are fitted with the most recent high temperature data, the temperature scaling is $\beta = -0.25 \pm 0.24$. This is appreciably different from the previous β value. This might indicate that the temperature dependence of the pressure shift cross section for the sodium-nitrogen system is more complicated than the simple power law; that is, β is a function of temperature rather than a constant.

The large uncertainty of this temperature scaling may be caused by the relatively large linewidth at the sides of the jet. It may also come from the uncertainty of the angle between the probe beam and the flow direction. Because our nozzle is a conical nozzle, the flow direction is not exactly parallel to the central line of the jet. This is particularly true at the boundary of the jet.

The pressure shift cross sections vary from 23 ± 3.2 Å^2 at 130°K to 7 ± 4.1 Å^2 at 260°K. The uncertainty at the boundary of the jet is larger than 50%.

With the large uncertainty in the pressure shift cross section measured, a serious question is raised about its effect on the velocity measurements. From Equation II-3, the Doppler shift per unit velocity is given by

$$(\Delta\nu_s)_D/v = (\nu_o/C)\cos\theta = 1.696\times\cos\theta \qquad \text{MHz/(m/sec)}$$

From this expression and Equation IV-4, the velocity uncertainty caused by the uncertainty in the pressure shift cross section can be found as

$$\Delta v = -3.56\times10^{3}\frac{1}{\cos\theta}\left(\frac{P}{P_o}\right)\Delta\sigma_s\cdot\frac{1}{\sqrt{T}} \qquad \text{(m/sec)}$$

where $\Delta\sigma_s$ = uncertainty of pressure shift cross section

Δv = uncertainty of velocity induced by $\Delta\sigma_s$

Note that Δv is inversely proportional to $\sqrt{T}$. Thus, though the $\Delta\sigma_s$ is larger at the boundary of the jet than that at the center of the jet, the uncertainty in velocity measurements introduced by $\Delta\sigma_s$ is not larger than that at the the center of the jet. Substituting the following flow conditions of our jet into the last expression:

$\theta = 127.5^{o}$

$P = 12.7$ torr

$\Delta\sigma_s = 3.2$ at $T = 130\ ^{o}K$ (center of the jet)

$\Delta\sigma_s = 4.1$ at $T = 260\ ^{o}K$ (boundary of the jet)

then,

$v = 27.5$ m/sec (at center of the jet)

$v = 24.9$ m/sec (at boundary of the jet)

That is about 4% at the center of the jet, and 6% at the boundary of the jet. Thus, the uncertainty in the pressure shift cross section does not affect the velocity measurement very much. However, the pressure shift itself is not negli-

gible in our system. The pressure shift is about 21% of the Doppler shift at the center of the jet and 10% at the boundary of the jet. The effect of the pressure shift is shown in Figure 24.

5.2 MEAN FLOW PROPERTY MEASUREMENTS

5.2.1 Measurements in a Nearly Ideally Expanded Jet

With an intersection angle of $127.5^{\circ}\pm0.5$ between the jet and the laser beam, measurements across a nearly ideally expanded jet were made. The measured velocity, temperature, pressure, and Mach number profiles are shown in Figure 24 to 27. The velocity and Mach number profiles can be compared with the profiles obtained from a pitot survey across the same jet, Figures 28 and 29. The velocity measured with the RDV at the center of the jet is about 700 ± 43 m/sec which is about 20 m/sec higher than that calculated from the pitot pressure. The systematically higher velocity measured by the RDV may be caused by an error in angle measurement; since the RDV is sensitive to the velocity component along the laser beam, the flow velocity is calculated from the cosine law. Suppose the true angle between the laser beam and the jet is 1.5° smaller than the measured angle, the calculated velocity will be biased by

$$\frac{V_m - V_t}{V_t} = \left(\frac{1}{\cos\theta_m} - \frac{1}{\cos\theta_t}\right)\Big/\left(\frac{1}{\cos\theta_t}\right)$$

$$= (\cos\theta_t/\cos\theta_m) - 1$$

$$= 3.377\%$$

Figure 24: Velocity Profile across an Ideally Expanded Nitrogen Jet Measured with the RDV

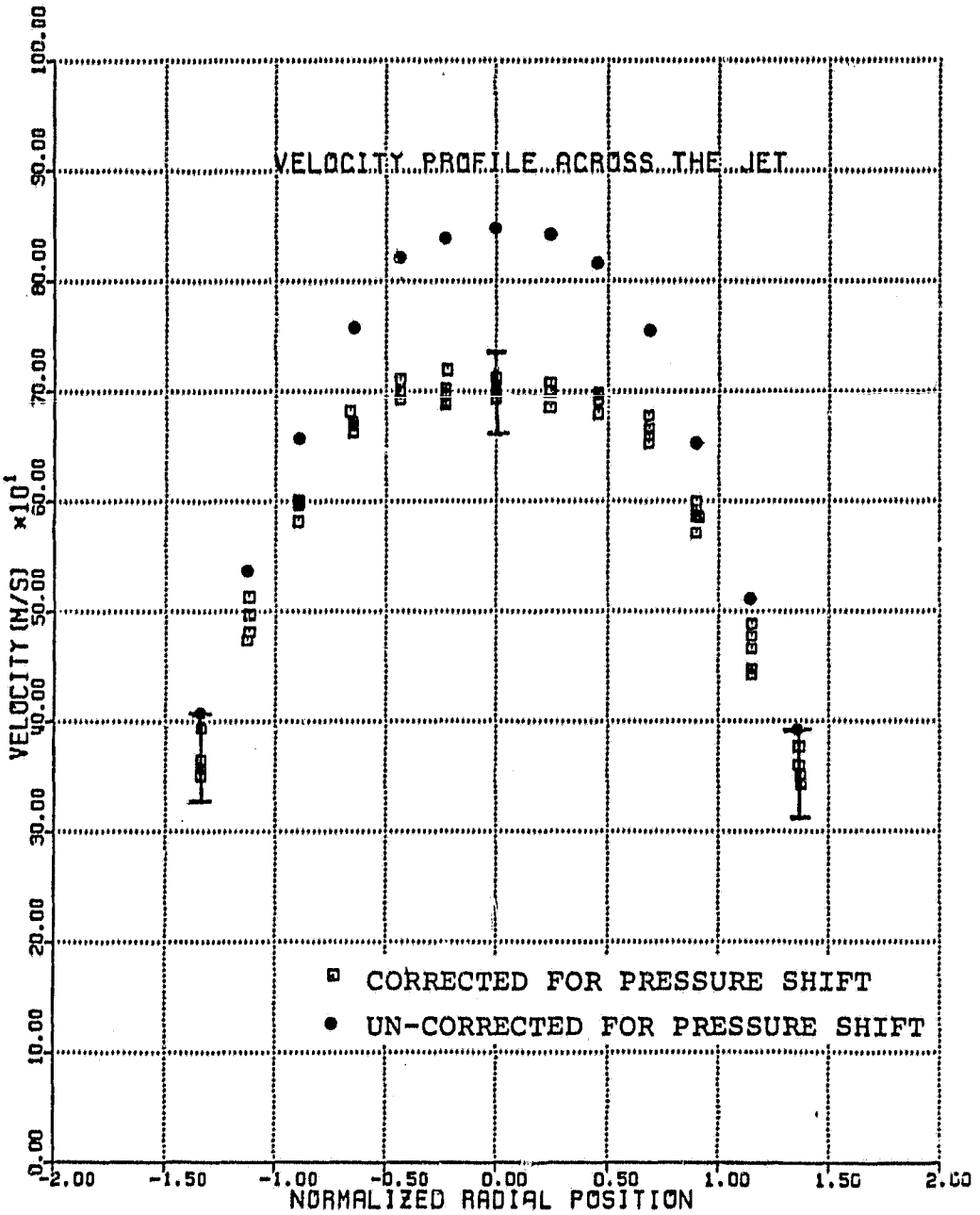

Figure 25: Static Temperature Profile across an Ideally Expanded Nitrogen Jet Measured with the RDV

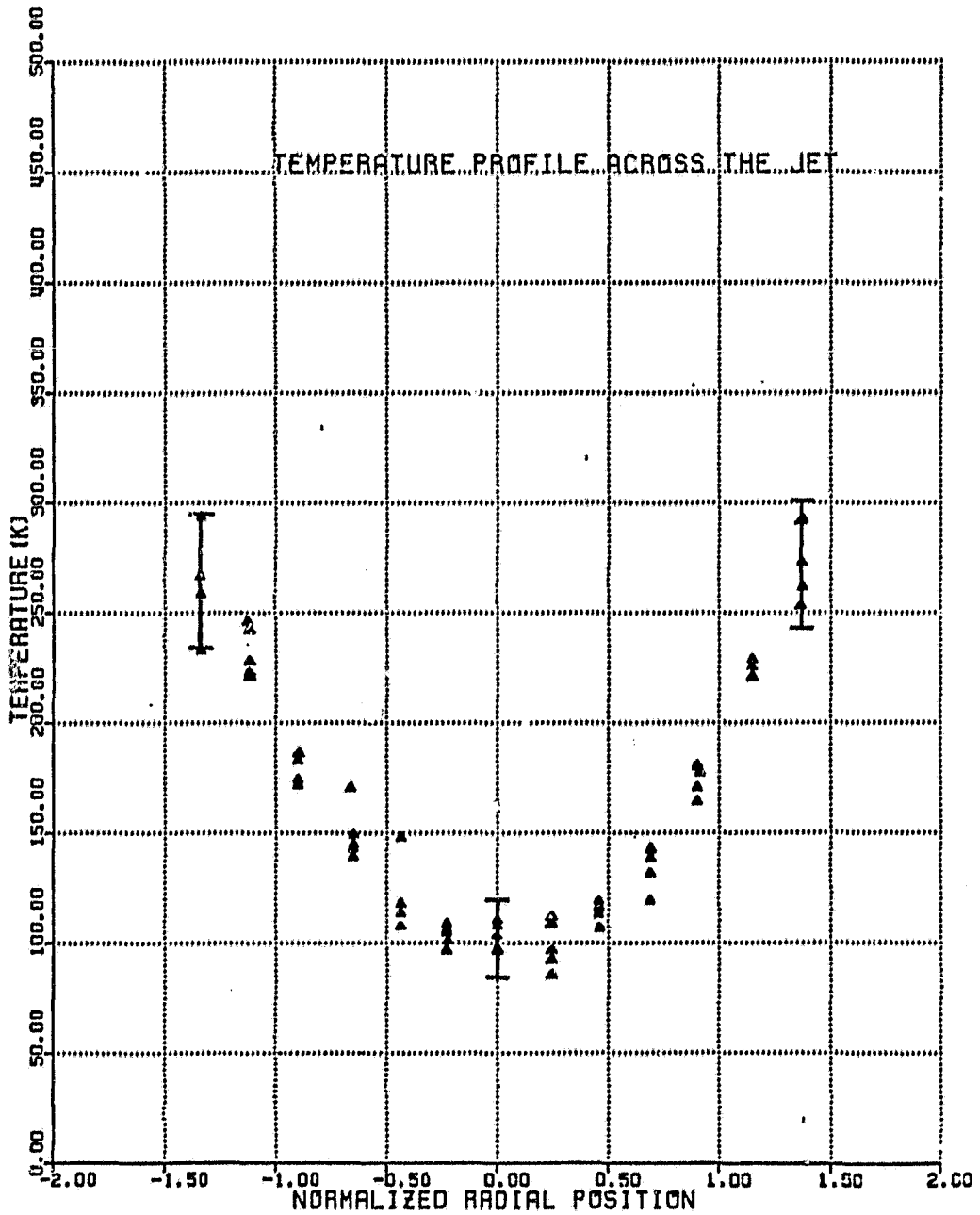

Figure 26: Static Pressure Profile across an Ideally Expanded Nitrogen Jet Measured with the RDV

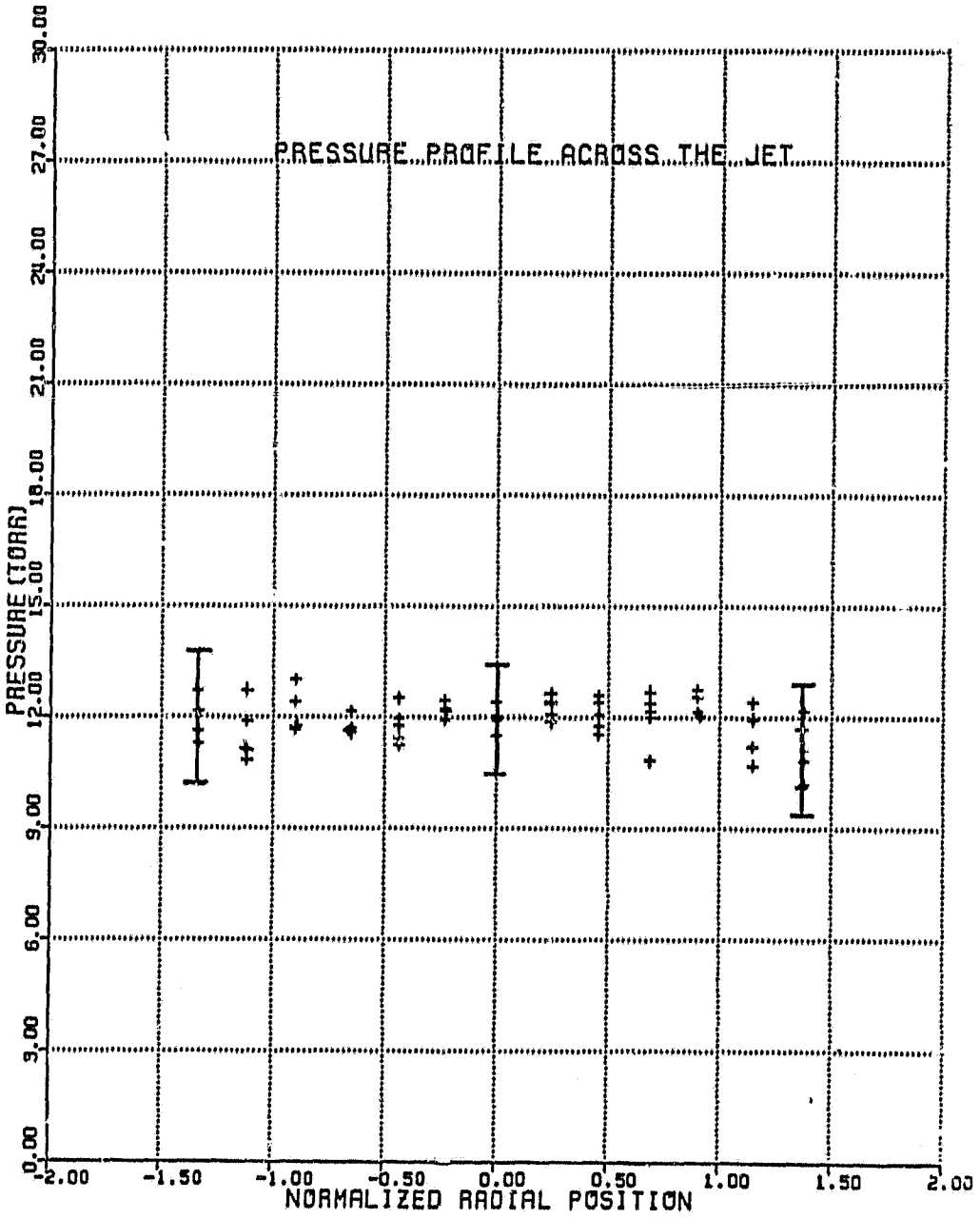

Figure 27: Mach Number Profile across an Ideally Expanded Nitrogen Jet Measured with the RDV

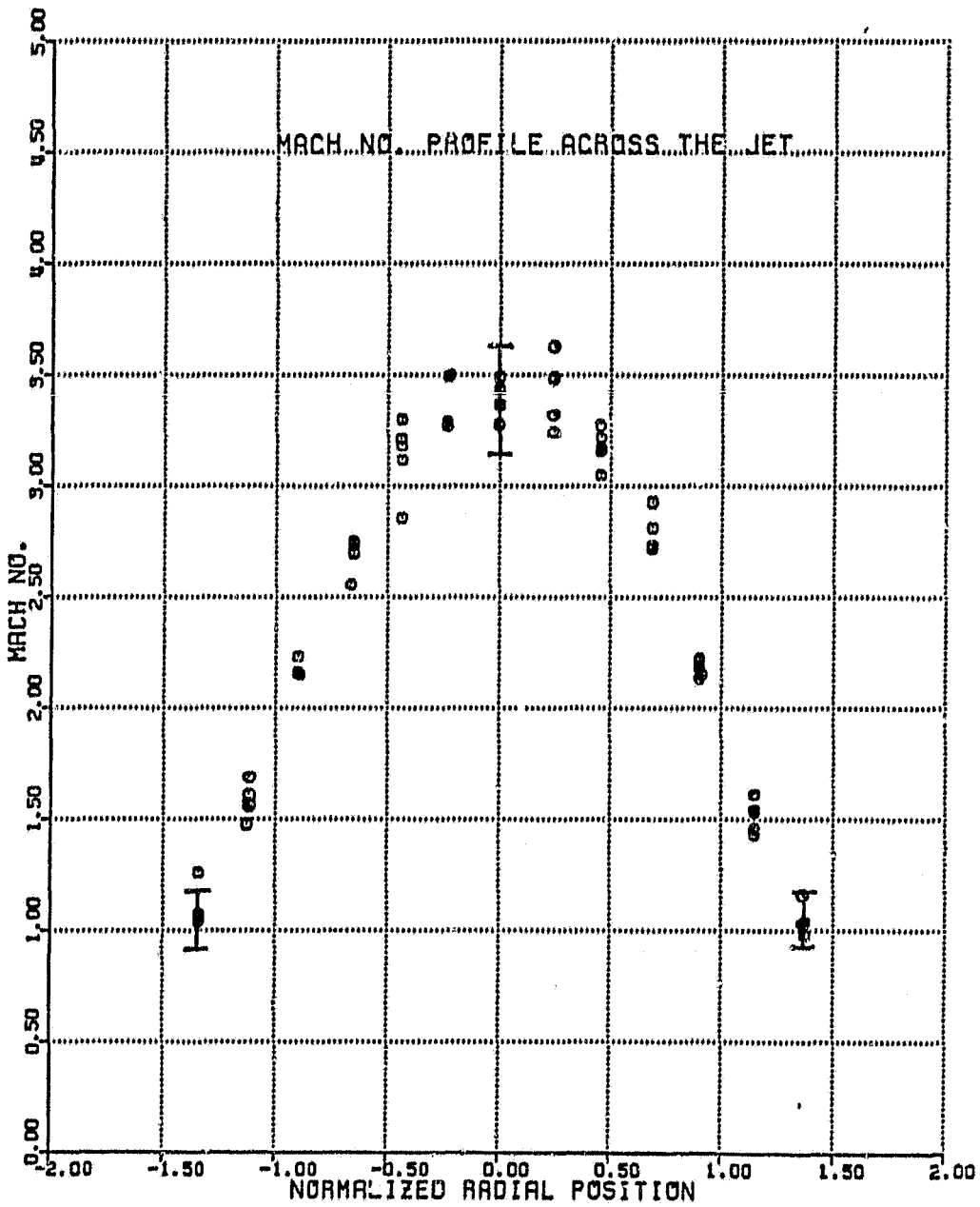

Figure 28: Velocity Profile across an Ideally Expanded Nitrogen Jet Calculated from Pitot Pressure

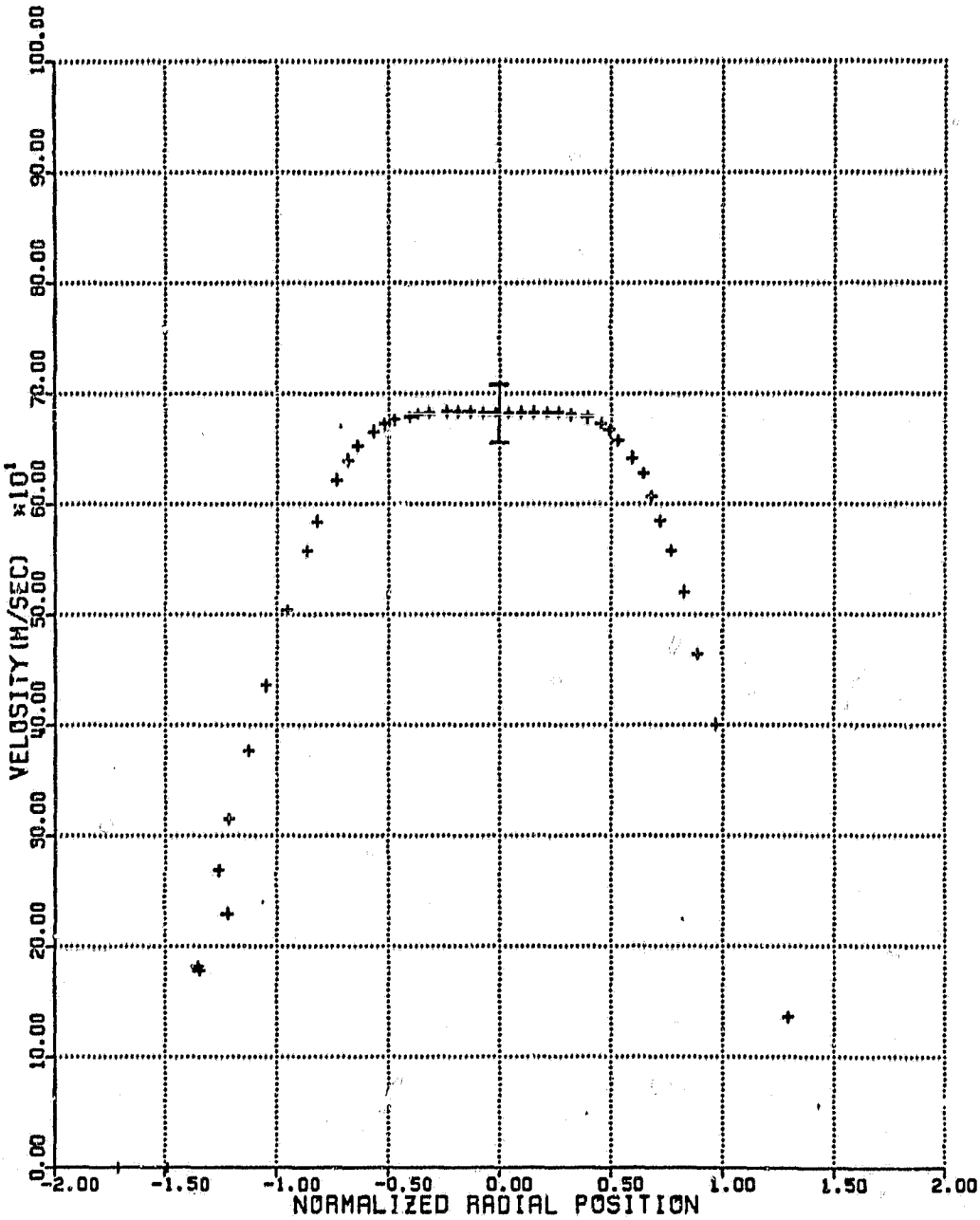

C-2

Figure 29: Mach Number Profile across an Ideally Expanded Nitrogen Jet Calculated from Pitot Pressure

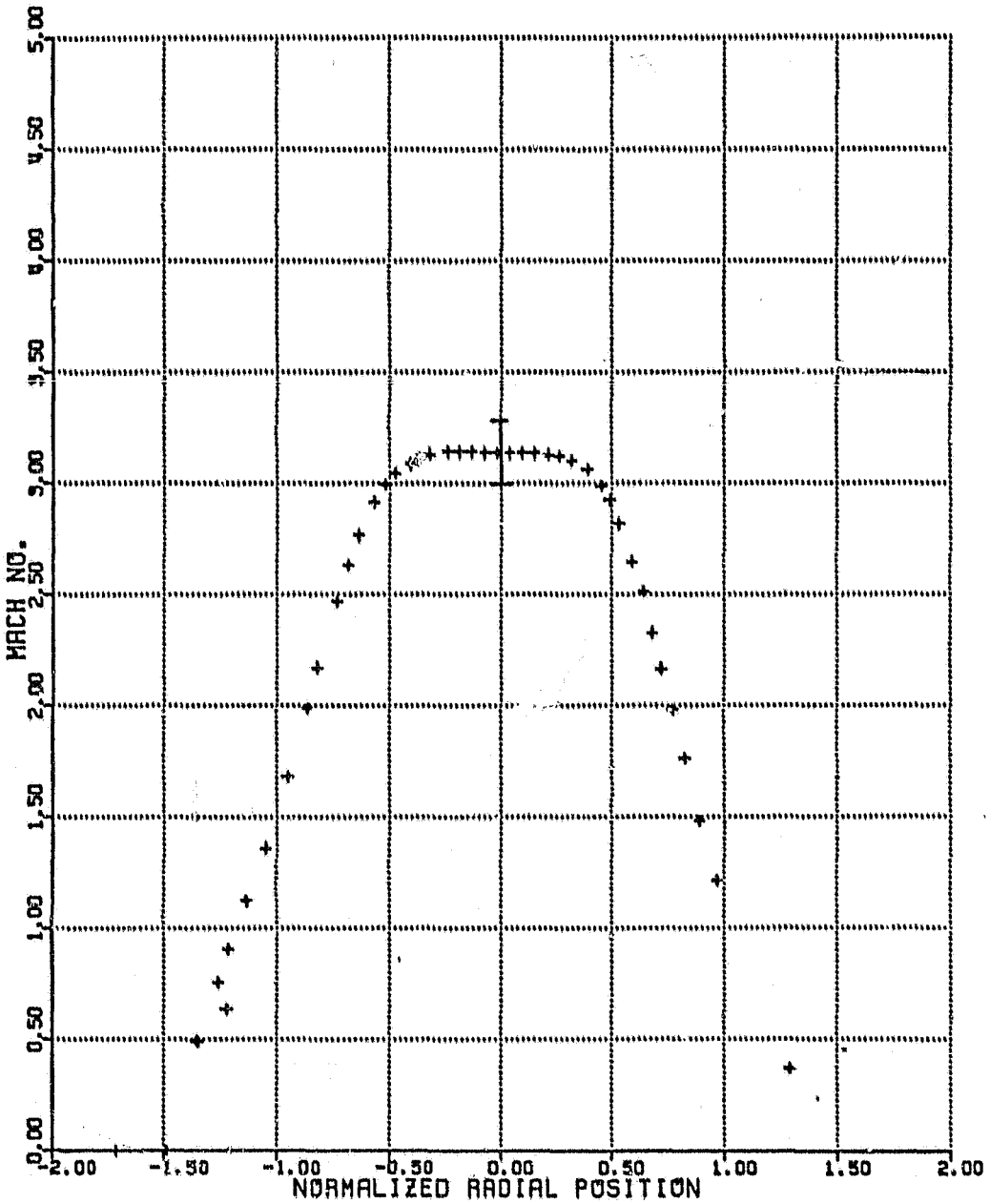

assuming that V_t = 680 m/sec

$$\Delta V = V_t - V_m = 22.96 \text{ m/sec}$$

Thus a small error in the measured angle may cause the systematically higher velocity measured by the RDV. Since the jet direction is not known exactly, it is assumed to be parallel to the side window. The small error in the angle may come from this assumption.

The difference between the measured velocities from the RDV and from the pitot tube becomes larger at the edges of the jet. To explain this discrepancy, one may first question the reliability of the results of the pitot survey. The velocity calculated from the pitot pressure is based on several assumptions. It is assumed that the static pressure is uniformly distributed, and the static pressure is the same as the pitot pressure measured outside of the jet. To estimate the error resulting from these assumptions, a 10% uncertainty in static pressure is assumed. From Equation IV-6, we can deduce that

$$\frac{\Delta P_{static}}{P_{static}} = \left\{\frac{4\gamma M^2}{2(\gamma-1)\gamma M^2-(\gamma-1)^2} - \frac{2\gamma}{\gamma-1}\right\}\frac{\Delta M}{M}$$

take $M = 3.4$ (obtained by the RDV)

$\gamma = 1.405$

$$\frac{\Delta P_{static}}{P_{static}} = 10\%$$

then $\frac{\Delta M}{M} = -5.16\%$

From Equations IV-7 and IV-8, the velocity uncertainty is

$$\frac{\Delta U}{U} = \{1 - \frac{(\gamma-1)M^2}{2(1+\frac{\gamma-1}{2}M^2)}\}\frac{\Delta M}{M}$$

$$= -1.54\%$$

Thus, the velocity uncertainty induced by the assumptions on the static pressure is very small.

The assumption that the total temperature is constant across the jet is obviously not true. Figure 30 indicates that the total temperature varies from 330°K to 370°K. Yet, $T_{total} = 350°K$ was used to calculate the flow velocity. From Equations IV-8 & IV-9, the error introduced by this assumption is

$$\frac{\Delta U}{U} \approx \frac{1}{2}\cdot(\frac{\Delta T_{total}}{T_{total}})$$

take $T_{total} = 350°K$

$\Delta T_{total} = 20°K$

then $\frac{\Delta U}{U} \approx 3\%$

Thus, the error caused by using constant total temperature across the jet is relatively small.

On the other hand, the large discrepancy may be mainly attributed to the fundamental limitation of the RDV since the RDV measures the flow properties through the existence

of the sodium atoms. In the mixing layer, essentially all the sodium atoms, that the RDV sees, come from the center portion of the jet. So, the sampling is biased toward high velocity part of the flow. This is the same problem that the LDV has. This discrepancy may also be attributed to the small pressure shift cross sections used at the edges. However, the pressure shift may count for less than 50 m/sec of the velocity difference. In addition it is posssible that, due to the much larger linewidth from the high temperature at the edges of the jet and the higher laser power used there, the systematic error caused by the limited frequency scan and optical pumping is very large. According to Ref. 7, this error can be as large as 25% under the flow condition at the edges of the jet. The much larger turbulent level and much lower sodium concentration in the shear layer also yield a much larger uncertainty in the velocity measurement.

A similar trend can be seen in the Mach number distribution when compared with the results from the pitot survey. The large uncertainties seen in the derived Mach numbers are mainly due to the uncertainties in the measured temperature, which is about $\pm 20^{\circ}K$ in the center region of the jet, rising to about $\pm 30^{\circ}K$ at the edges of the jet. The resulted Mach number uncertainty is about ± 0.28 at the center of the jet, and ± 0.12 at the boundary of the jet. The relatively small uncertainty of the Mach number at the boundary of the jet is

due to the high static temperature there. Similarly, the uncertainty in the static pressure measurement is quite large, being about ±1.5 torr (which is about 13% of the absolute flow pressure). These uncertainties are mainly due to the limited scanning of the dye laser frequency. As discussed in Chapter II, in order to separate the Lorentzian and Gaussian profiles, we need the spectral profile of the line wing. However, with the limited laser frequency scan of 5 GHz compared to a sodium line HWHM of 600-750 MHz , only limited portion of the line wing profile can be sampled. Thus the curve fitting gave a large uncertainty in the temperature and pressure measurements.

Nevertheless, these measurements agree reasonably well with the pitot probe and total temperature measurements. The pitot pressure measured outside of the jet was 12.7 torr and the pressure obtained from the RDV was centered around 12 torr. The total temperature calculated from the relation IV-5 is presented in Figure 30. This can be compared with the total temperature profile measured by a thermocouple, and corrected with a recovery coefficient of 0.95. This is presented by the crosses in the same figure. The agreement between these two measurements is very good. However, the good agreement at the edge of the jet is somewhat surprising. Because the velocity measured there is biased to a higher value. This indicates that the temperature measured there is lower than it should be(about 35^{o}K lower). This

might be explained by the same argument given to the velocity discrepancy. In the mixing layer, essentially all the sodium atoms seen by the RDV come from the center region of the jet, and carry with them the low static temperature that they experienced there. Therefore, the static temperature measured by the RDV is biased to a lower value at the edge of the jet.

5.2.2 Measurements in an Underexpanded Jet

Measurements in an underexpanded jet were also made. The flow with a diamond-shaped structure was generated by mismatching the plenum chamber pressure and the jet pressure. The measurements across an oblique shock are shown in Figure 31. Similar measurements across an expansion fan are shown in Figure 32. Although these results clearly indicate the flow behavior, they can not be used for quantitative analysis because the structured flow is three-dimensional, and the present RDV measurements are one-dimensional.

5.3 TURBULENCE MEASUREMENTS

The RDV signal was spectrally analyzed to find the frequency component of the fluctuations in the flow properties. Most of the turbulence measurements were done at 6.5 nozzle diameters downstream of the nozzle exit with a sampling rate of 50 KHz and a filter cutoff frequency of 10 KHz. This low sampling rate was used because of the limitation of photon

Figure 70: Total Temperature Profile across an Ideally Expanded Nitrogen Jet

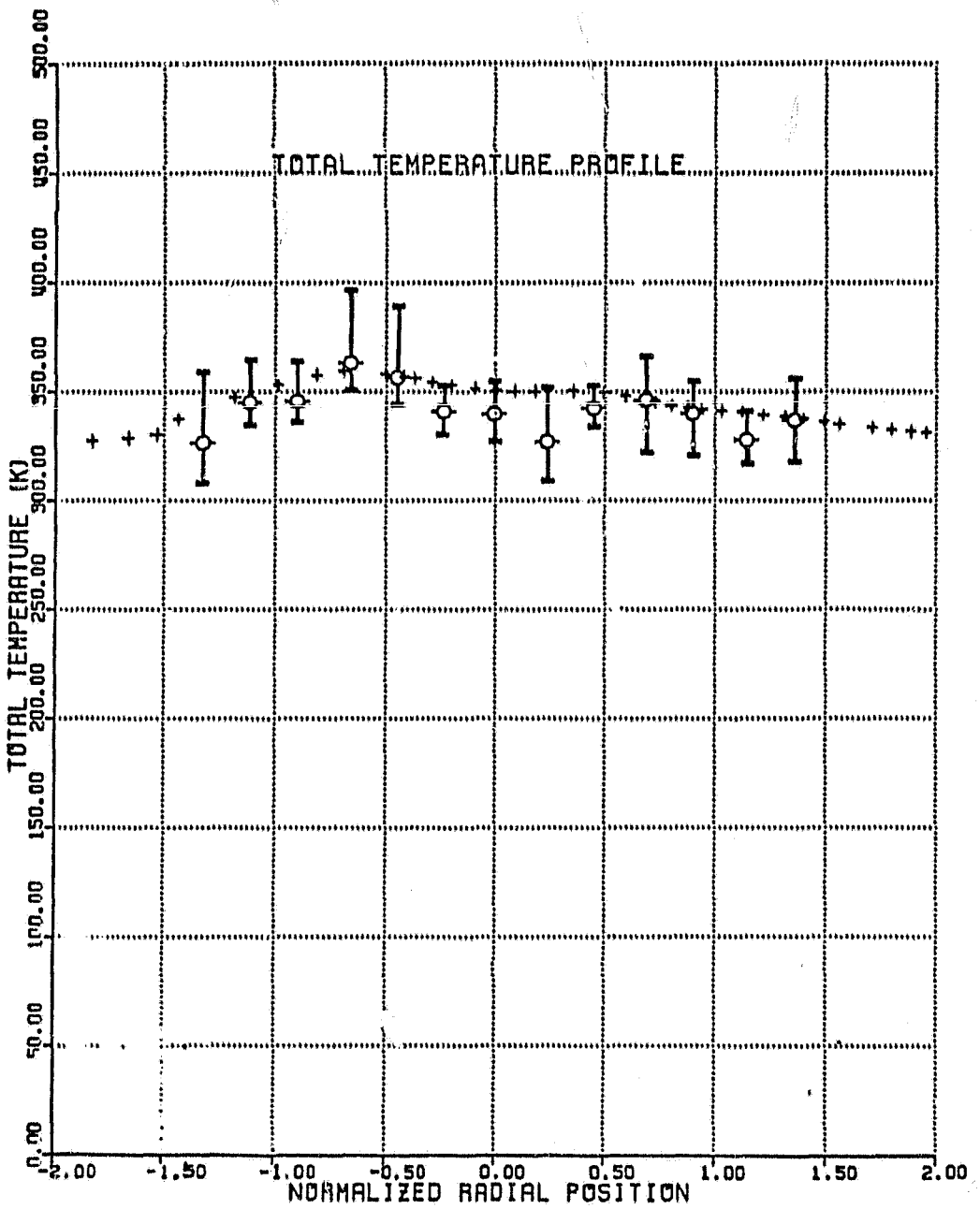

Figure 31: The RDV Measurements in an Underexpended Jet (Oblique Shock)

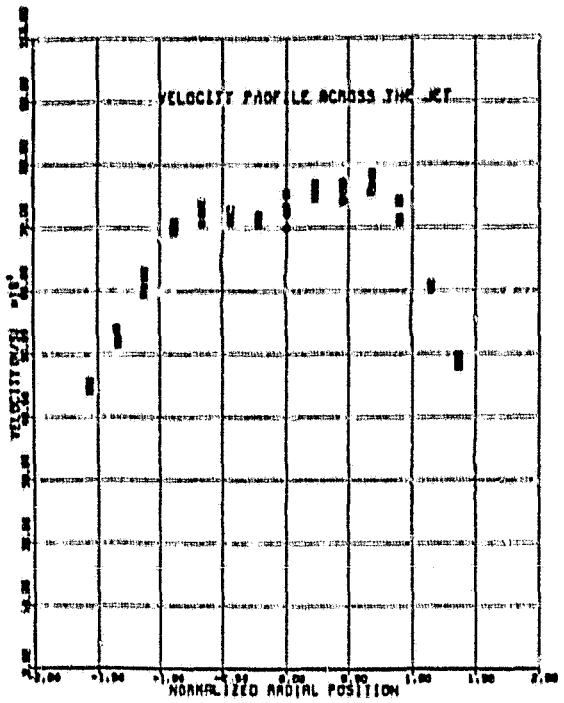

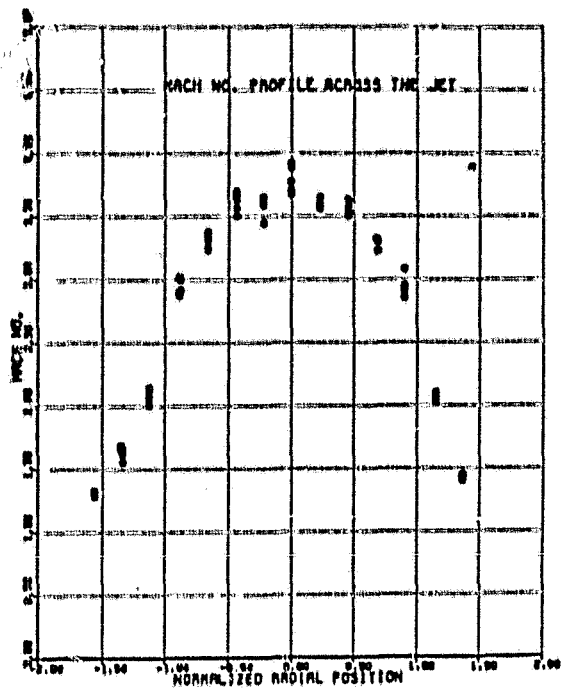

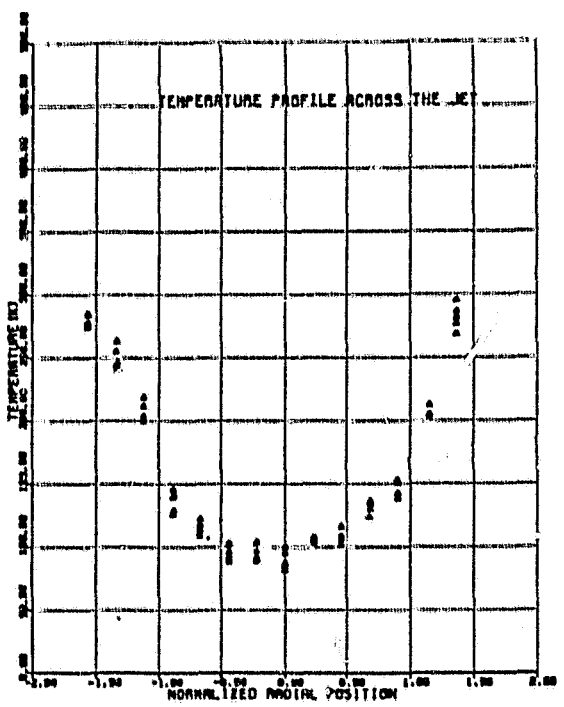

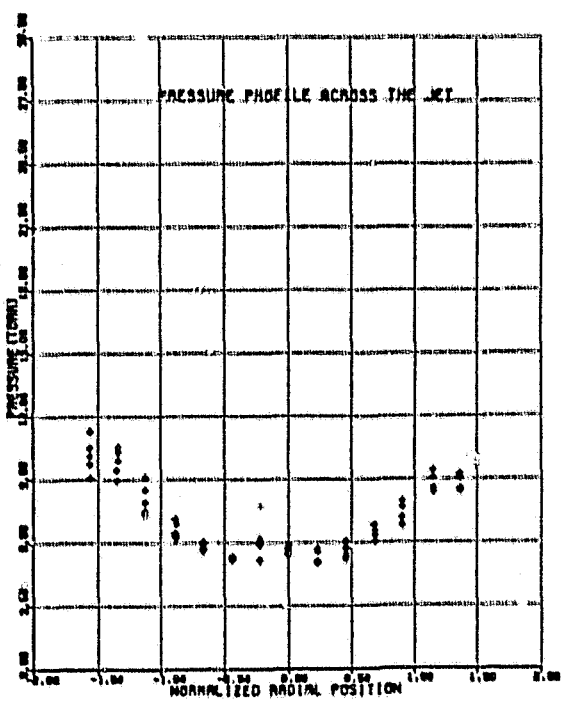

Figure 32: The LDV Measurements in an Underexpended Jet (Expansion Fan)

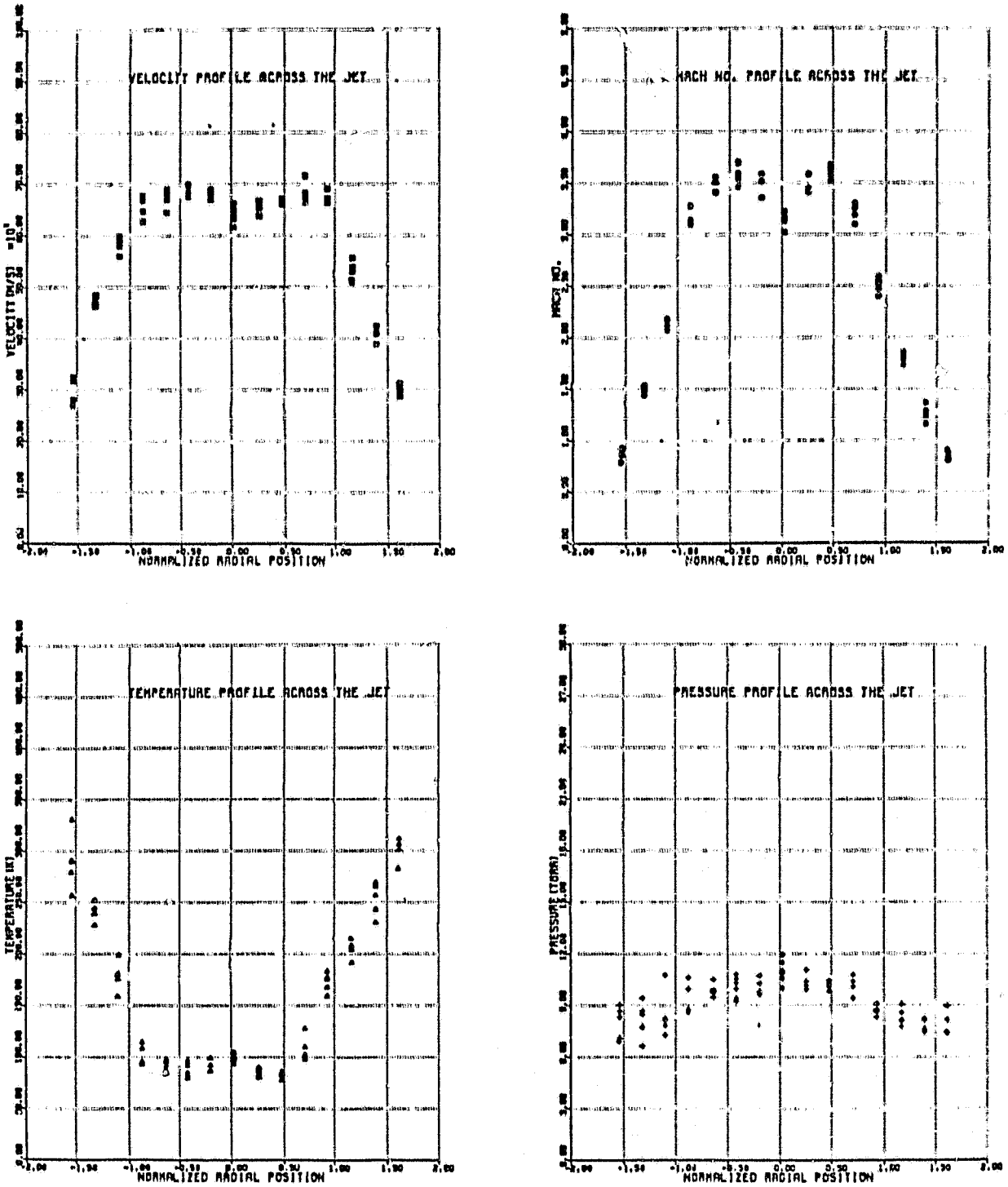

statistics which will be discussed later in this section. Before we examine the turbulence data, we should first examine the fluctuations of the laser intensity(Figure 33). It can be seen that the laser intensity has strong fluctuations only at low frequency part of the spectrum (lower than 200 Hz).

Figure 34 shows the power spectral densities of the fluorescence signal measured across the jet with the laser frequency tuned to the half maximum of the spectral line. Similar spectra were obtained when the laser frequency was tuned to the peak of the spectral line. Notice that there is no special frequency structure in these spectra. The frequency spectra obtained from the hot wire data are shown in Figure 35. The hot wire was operated with an overheat ratio of 0.71. At this overheat ratio the hot wire is sensitive to both mass flux and flow temperature fluctuations(69).

To create a well defined spectral feature in the turbulent flow, a thin metal tab(0.01 in. thick, 0.03 in. wide, 0.5 in. long) was introduced into the jet to generate large scale eddies. As shown in Figure 36, strong 400 Hz and 1050 Hz fluctuations were generated in the flow and could be observed by the RDV. The corresponding frequency spectra of the hot wire signal are shown in Figure 37.

To investigate the cause of the fluctuation, a thicker metal tab with the same width and length was used. No

Figure 33: Power Spectrum Density of the Laser Intensity

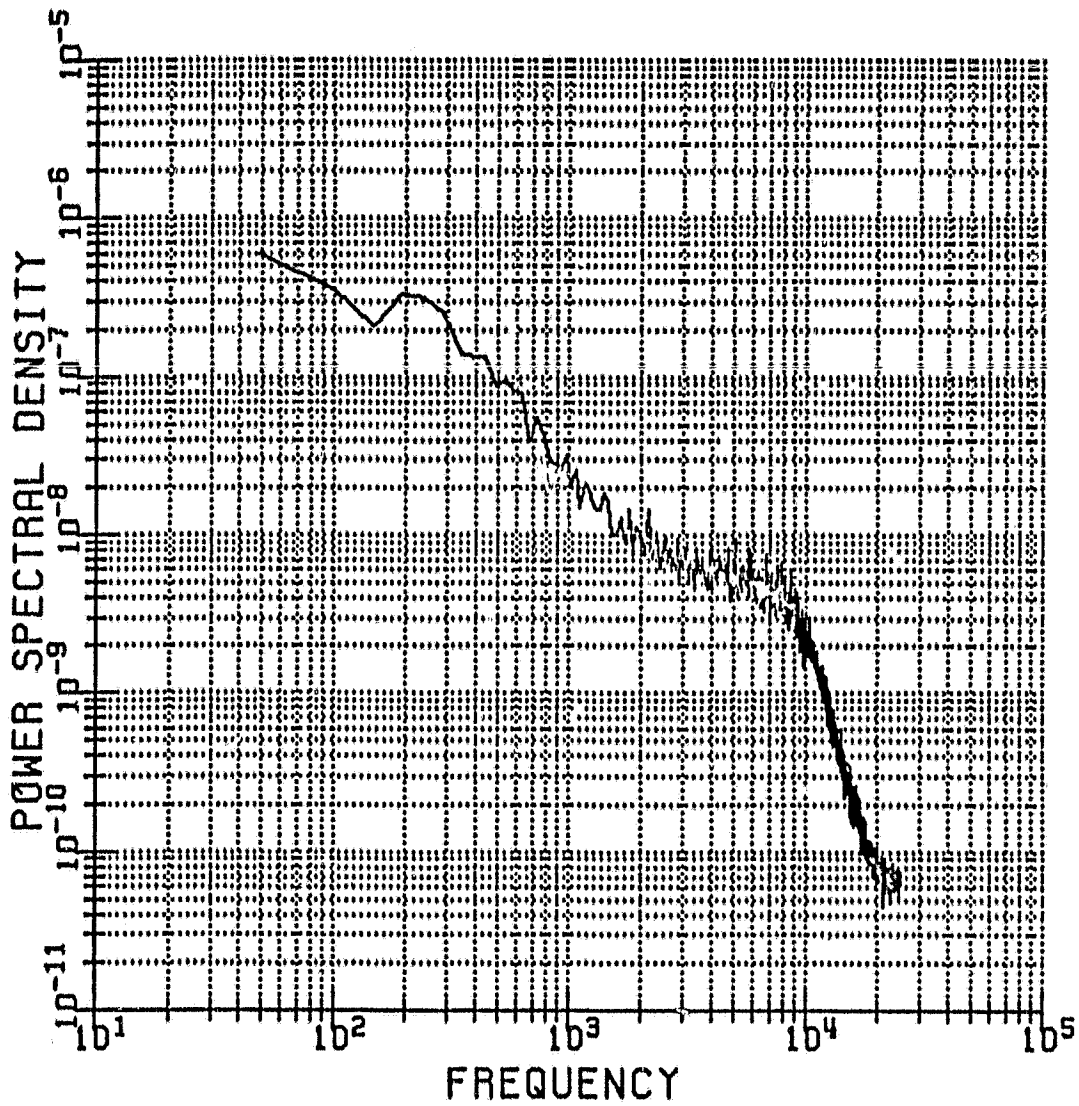

Figure 34: Power Spectra of the RDV Signal from the Free Jet

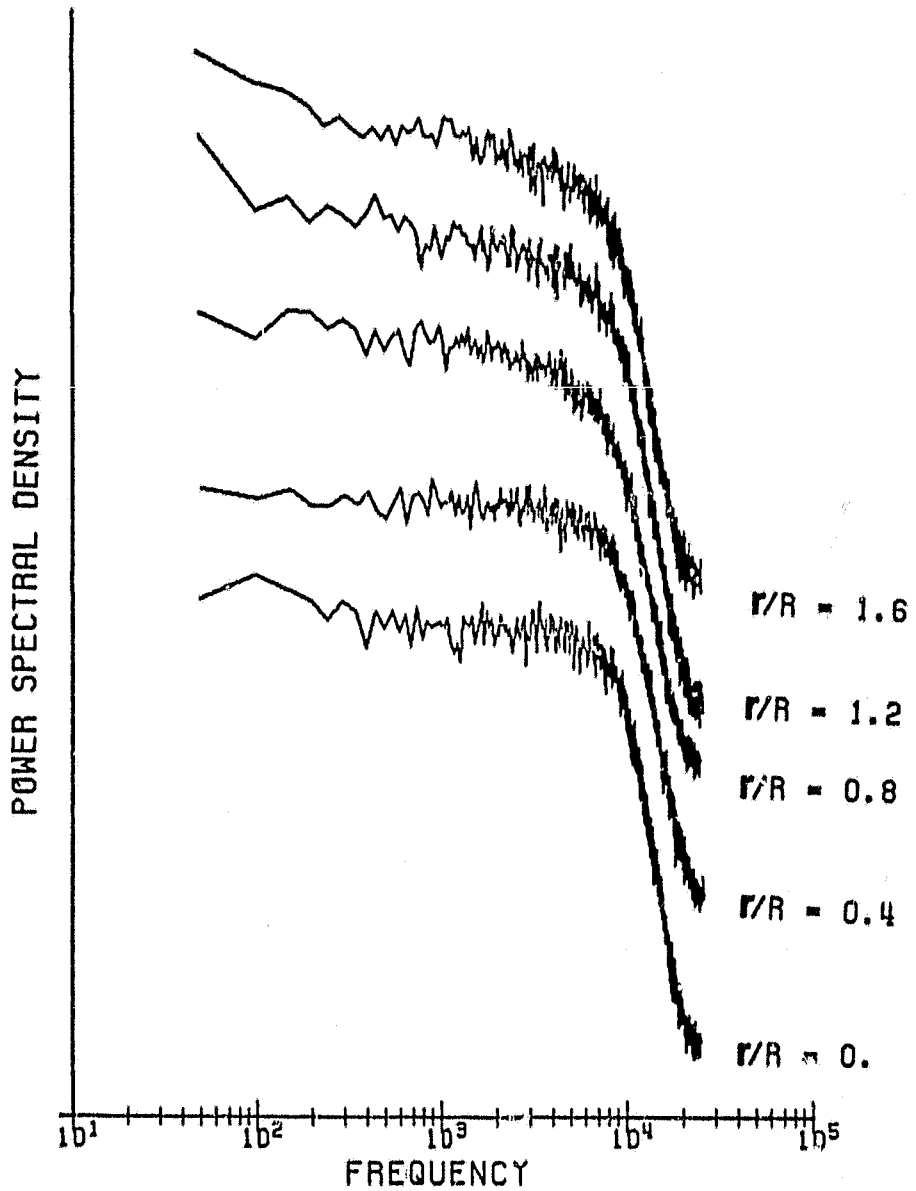

Figure 35: Power Spectra of the Hot Wire Signal from the Free Jet

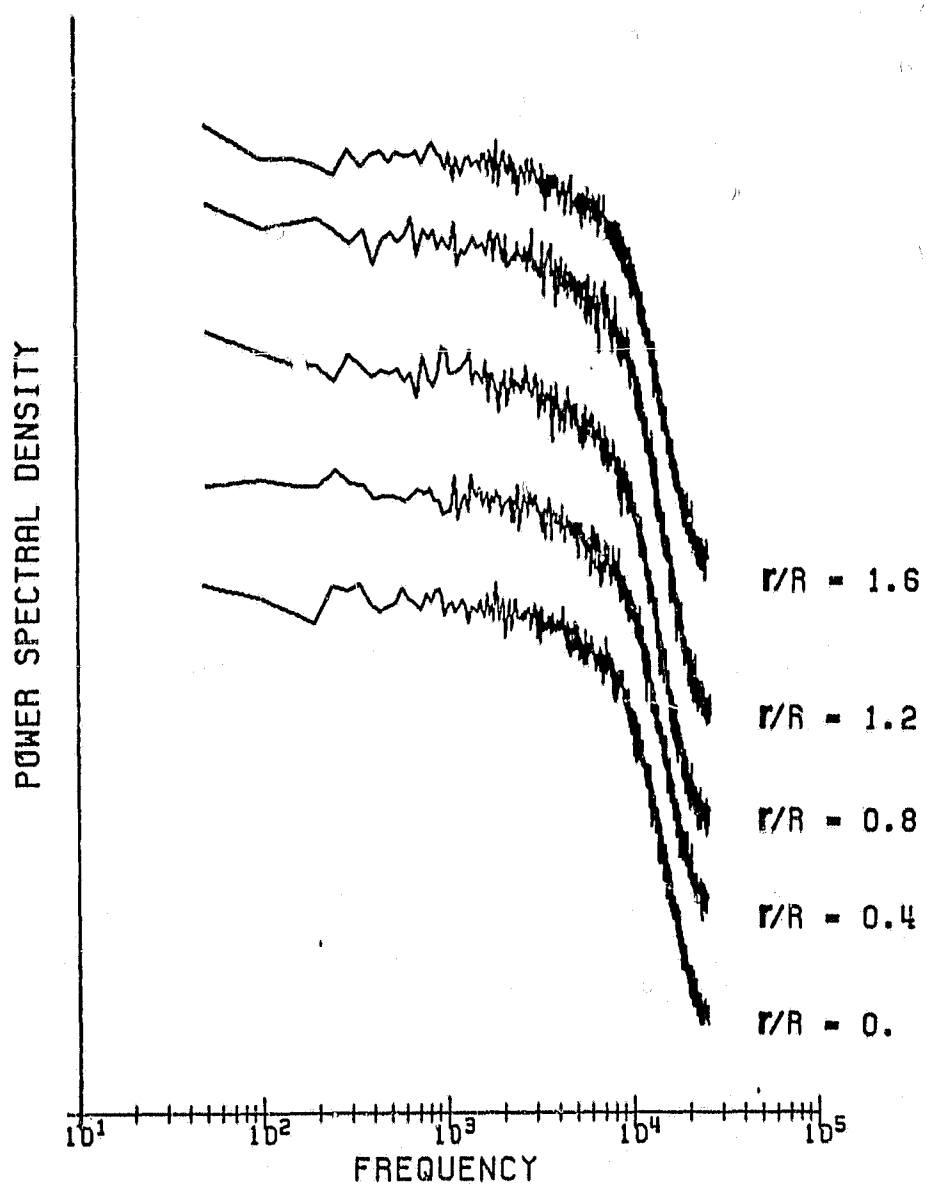

Figure 36: Power Spectra of the RDV Signal from the Jet with a Metal Tab

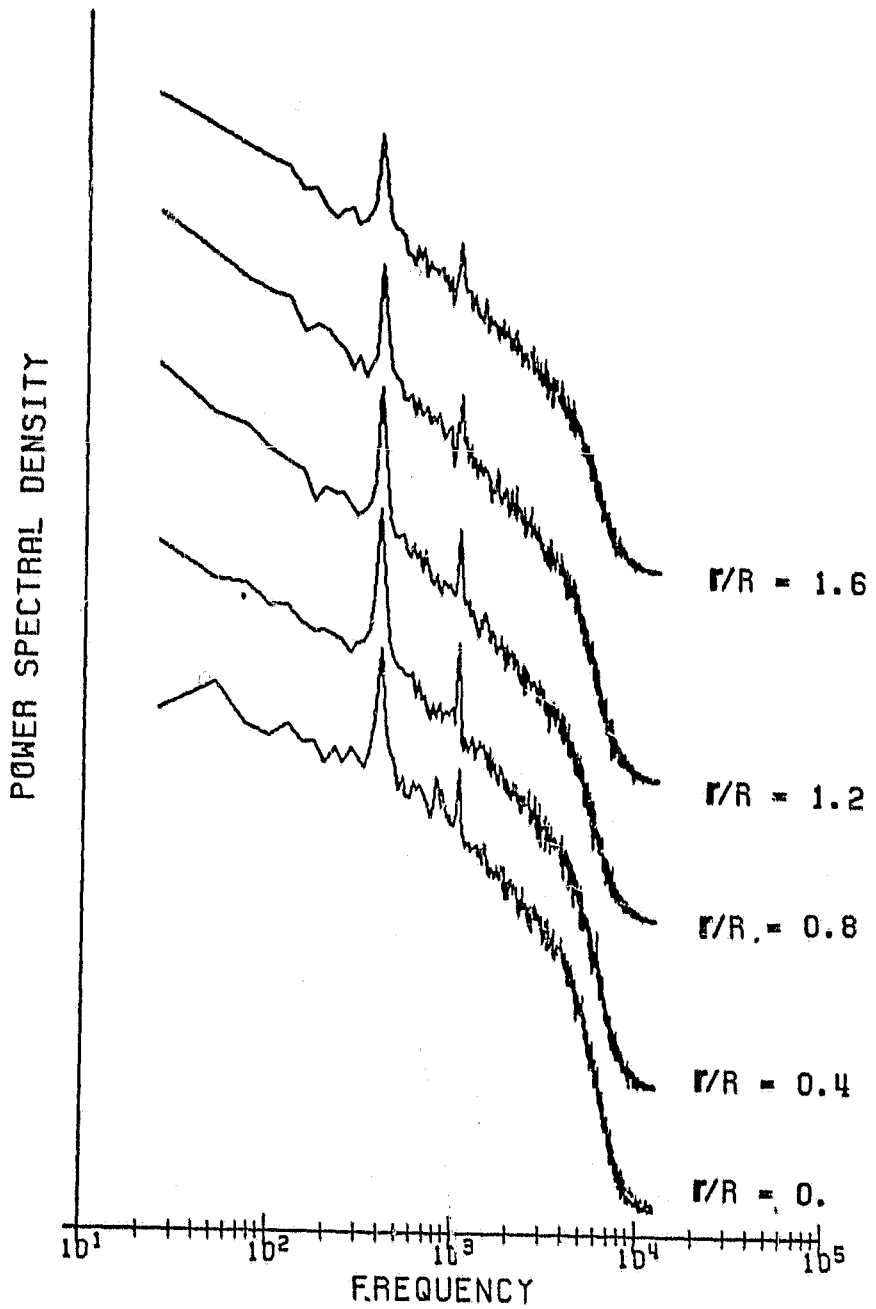

Figure 37: Power Spectra of the Hot Wire Signal from the Jet with a Metal Tab

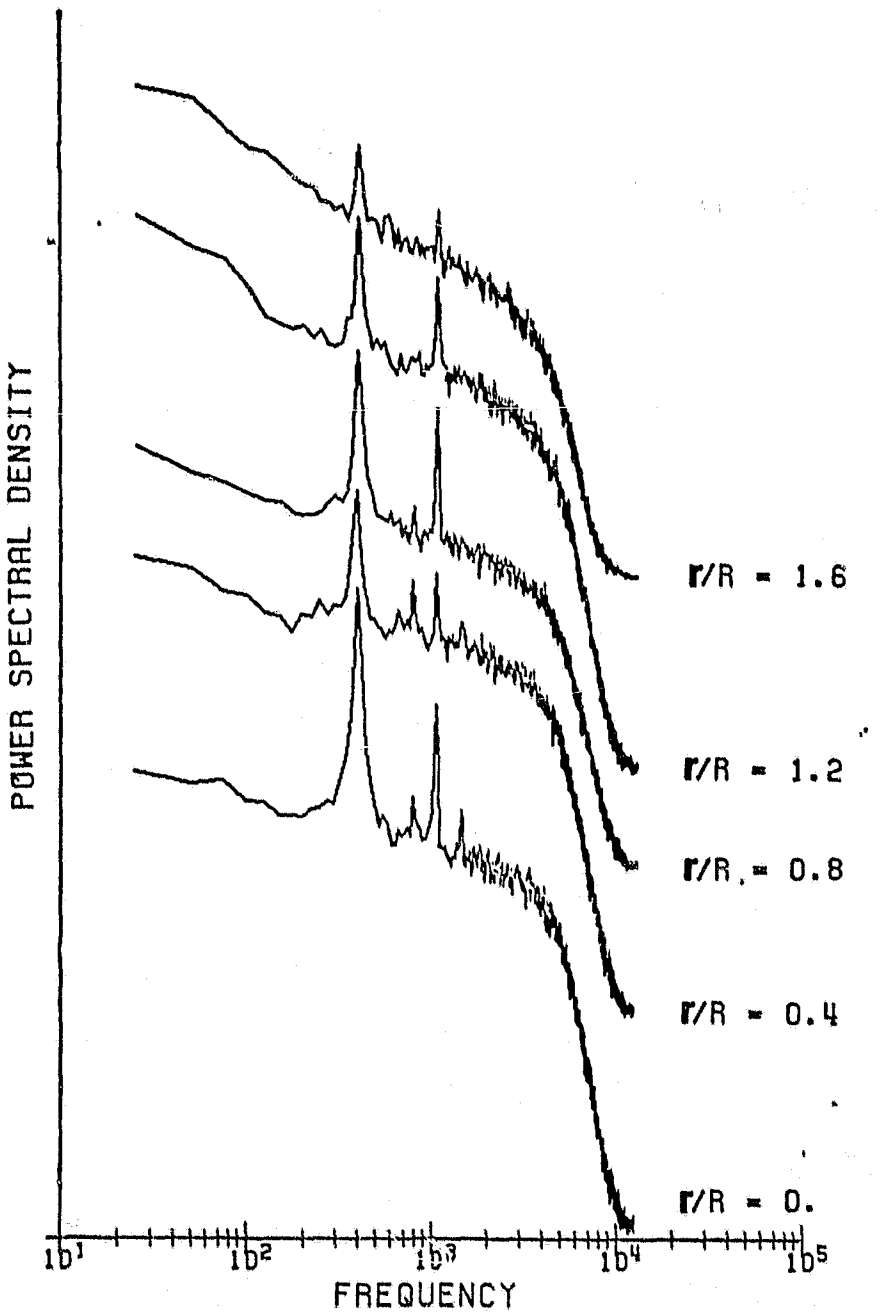

strong peak could be found in the frequency spectrum. Thus, the fluctuations probably arise from the vibration of the metal piece instead of the vortices shed from the metal obstacle. To confirm this, another metal tab shorter than the original one (0.375 in. long, 0.01 in. thick, 0.03 in. wide) was introduced into the jet. It was found that the frequency of the disturbance shifted to 550 Hz. This upshift in frequency is because of reduction in the mass of the oscillating piece. This appears to confirm that the fluctuations are caused by the vibration of the metal tab which was in turn driven by the flow.

By stepwise scanning the laser frequency for 32 steps, and spectrally analyzing the data at each laser frequency step, we can investigate the nature of the 400 Hz fluctuation mentioned above. The 32 laser frequency steps along the spectral lines, and the measured peak power of the 400 Hz components are shown in Figure 38. Three node points can be found, which agrees with the velocity sensitivity curve shown in Figure 18 with a=.316. Thus, the velocity fluctuation must be important in the 400 Hz fluctuation. However, the frequency positions of these nodes are shifted to the right of those predicted by the velocity sensitivity curve. This indicates that the 400 Hz fluctuation is not a pure velocity fluctuation, but is a combination of velocity fluctuations and temperature or pressure fluctuations. This is to be expected in a compressible flow since a velocity fluctua-

tion is always associated with a temperature or density fluctuation. Notice that the second and the fourth peaks in Figure 38 are smaller than those predicted by the velocity sensitivity curve alone(Figure 18). A comparison with Figure 19 indicates that temperature is also fluctuating. Assuming that only the velocity and temperature fluctuations are important, the fluctuation of fluorescence intensity is

$$I_\nu' = S_V V' + S_T T'$$

and

$$\overline{I_\nu'^2} = S_V^2 \overline{V'^2} + S_T^2 \overline{T'^2} + 2 S_V S_T \overline{V'T'}$$

where $I_\nu'^2$ is obtained from the experiment. S_V^2, S_T^2, and $S_V S_T$ are known from the velocity and temperature sensitivity curves. The three unknowns $\overline{V'^2}$, $\overline{T'^2}$, and $\overline{V'T'}$ can be obtained by solving this equation at three different frequencies or by fitting the experimental curve with a least squares curve fitting scheme. In this work, the data are preliminary and there is a rather large uncertainty, so no attempt was made to least squares fit. However, by simply taking the correlation coefficient of V' and T' to be -1, and letting $\sqrt{\overline{T'^2}}/\sqrt{\overline{V'^2}} = 0.15$, the solid curve in Figure 38 can be constructed. Though the fitting is not exact, the special characteristics such as the zeros and the relative peak heights are very similar to the experimental results. The pressure fluctuation may also exist, but in an ideally expanded jet, these are expected to be small.

Figure 38: Variation of the Power of the 400Hz Fluctuation with the Laser Frequency

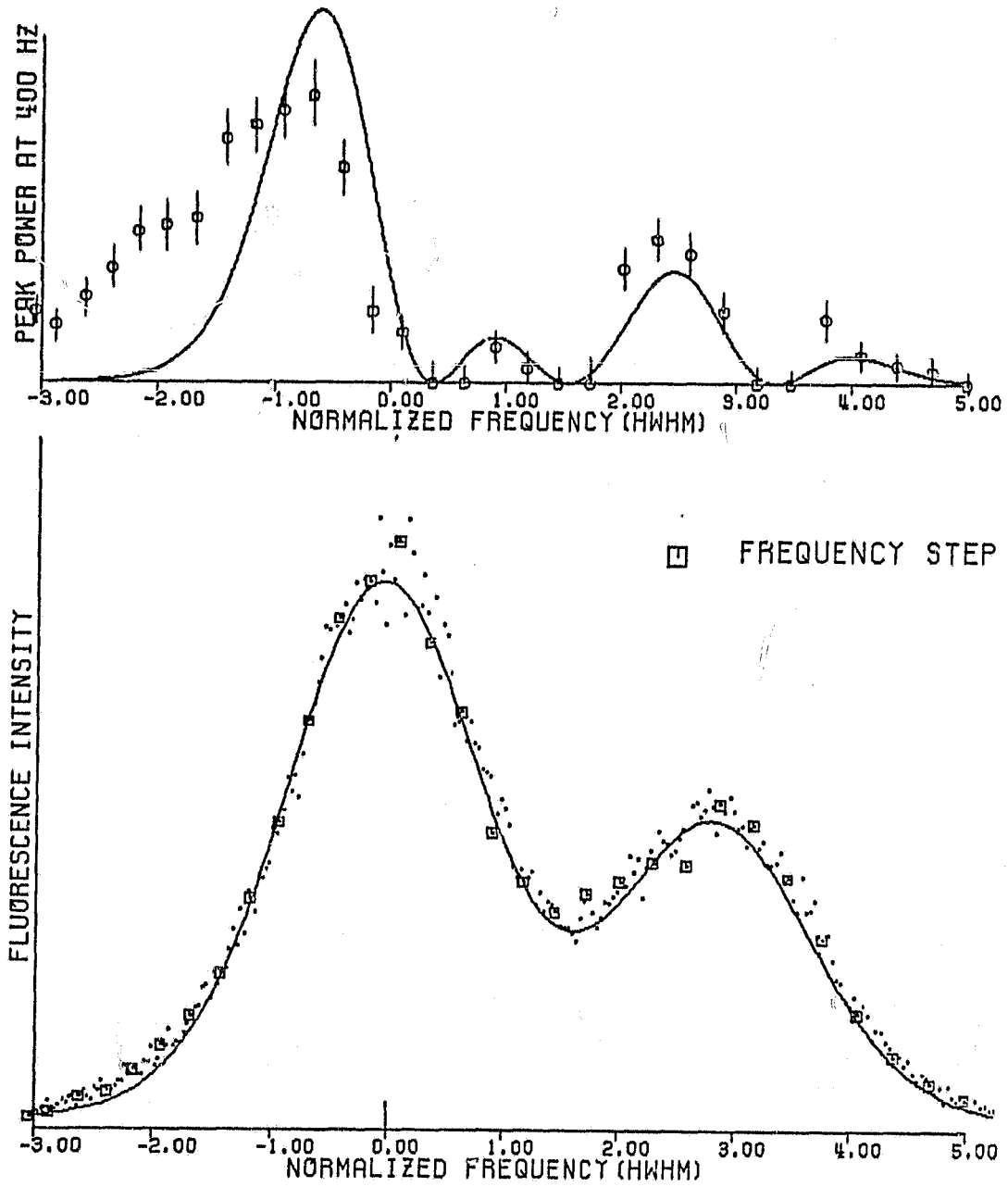

5.3.1 Frequency Response

To check the frequency response of the RDV technique, a EMI 9524S photomultiplier tube, whcih can take 10 times more photons than the RCA C31034 photomultiplier tube, was used. The sampling rate was 250 KHz, and the filter cutoff frequency was 50 KHz. A high frequency distur bance was generated by stretching a thin wire across the flow 2 nozzle diameters downstream of the nozzle. The vibration frequency of the wire was about 410 Hz. High frequency fluctuations were detected 7 nozzle diameters downstream from the wire(Figure 39). These high frequency fluctuations are believed to be jet noise, generated by large scale disturbances which are induced by the thin metal wire vibration. From the theory developed by Tam, et al.(70,71), the frequency of the acoustic radiation can be calculated from the formula

$$\frac{\pi f D}{a_o} = 1.202\left(\frac{M-1}{M+1}\right)^{1/2}\{1.406-0.198(M-1.40627)^{1/2}\}^{-1} - (0.033M^2-0.219M+0.207)$$

where D = diameter of the jet

a_o = ambient speed of sound

M = Mach number

f = frequency of the noise

By substituting the following values into this formula,

M = 3.1

a_o = 381 m/sec at T = 60°C

D = 0.58 cm = exit diameter of the nozzle

Figure 39: High Frequency Jet Noise Measured by the RDV

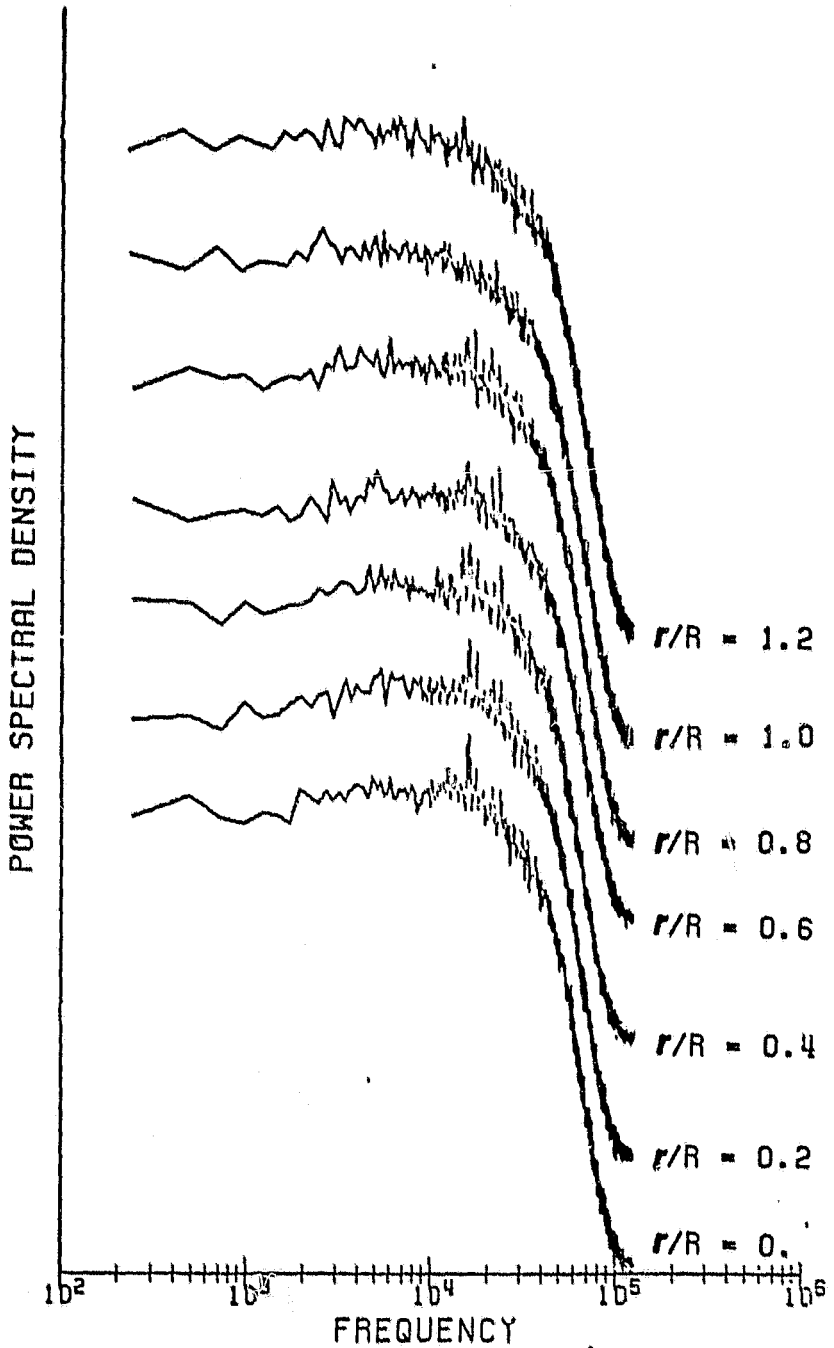

we obtained f=19.05 KHz.

This result is in agreement with the experimentally observed frequencies. As can be seen in Figure 39, there are more frequency peaks scattered around 16 KHz and 22 KHz. These frequencies agree with the experimental result obtained by Trott, et al.(72,73), who found from hot wire and microphone measurements that jet noise contains numerous discrete frequency modes centred around a Strouhal number of 0.18.

Since $S_t = \frac{f}{V/D}$

$V = 700$ m/sec

$D = 0.58$ cm

$S_t = 0.18$

lead to $f = 21.72$ KHz

The multi-frequency structure of the jet noise detected might indicate that there is more than one mode of large scale disturbance in the jet.

The RDV measurements of the high frequency fluctuations can be compared with the hot wire measurements(Figure 40). The comparison shows that the frequency response of the RDV compares favorably with that of the hot wire system. In a constant-temperature hot wire system, the frequency response is determined by the gain and the bandwidth of the amplifier, the overheat ratio, the resistance of the bridge, the fluid velocity, and the thermal properties of the sensor and the fluid. Though the gain-bandwidth product of the modern

amplifier is large, the frequency response is normally limited to about 200 KHz because of the dependence on the flow and sensor properties (96).

The frequency response of the RDV system depends on the frequency response of the photo-detectors and photon statistics. The rise time of the photo-detectors is less than a microsecond (the photomultiplier had a rise time of 2 nsec). Thus the frequency response of the photo-detectors poses no limitation on the frequency response of the RDV measurements. However, the problem of the photon statistics is not that simple. Since the photons are discrete particles, they follow Poisson statistics, and the signal to noise ratio is $1/\sqrt{N}$ where N is the number density of photons detected during the observation time window. One needs at least 100 photons to ensure less than 10% noise. Thus, if we want the frequency bandwidth to be 100 KHz, we have to detect at least 10^7 photon/sec. This is too intense for some photomultipliers. One needs a photo-diode or a photo-transistor to detect the high frequency signal. In that case, the frequency response can be in the order of MHz.

5.3.2 Spatial Resolution

The spatial resolution of the RDV is very good. The laser beam was focused into a small spot($d \approx 0.1$mm). Since the circular aperture in the signal detection optics has a diameter of 0.343 mm, the probe volume is given by

$$V_{probe} = 0.1\pi \cdot (0.343/2)^2 \qquad (mm^3)$$

Figure 40: High Frequency Jet Noise Measured by the Hot Wire

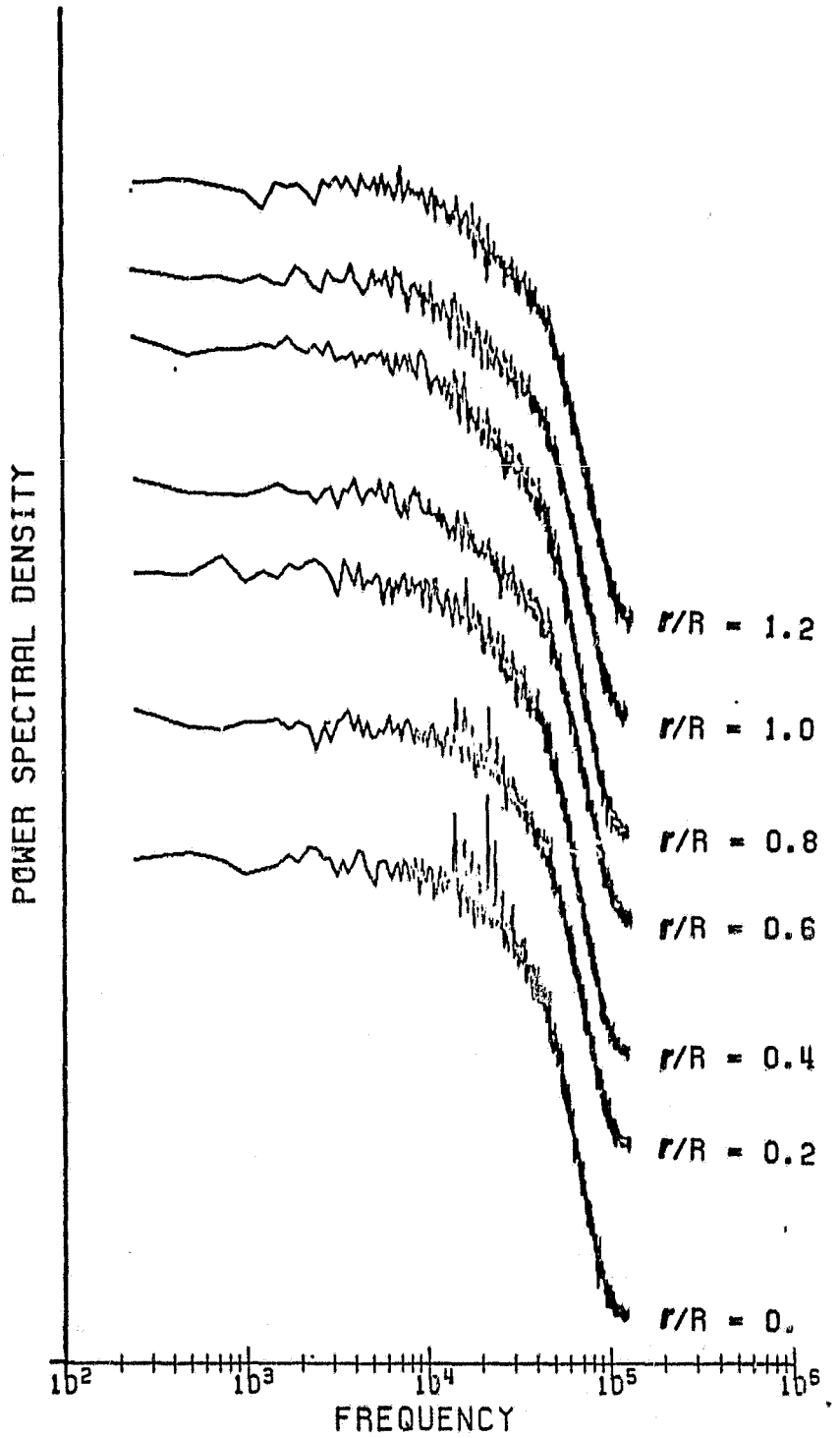

$$= 0.924 \times 10^{-5} \qquad (cm^3)$$

The hot wire also has very good spatial resolution because the wire diameter is 5 μm, but the length of the wire is relatively large for our jet. The ratio of the wire length to the jet diameter is 2mm/5.8mm = 0.35. Thus, the hot wire measurements are not well resolved in that dimension. This might explain the behavior shown in Figure 40. Notice that at the center of the jet, strong fluctuation around 20 KHz can be detected by the hot wire. But as the probe point moves outward, these fluctuations reduce sharply. This is probably because of the spatial integration effect which reduces the high frequency fluctuations in the outer region of the flow where the correlation of the fluctuations is not as strong as that of the center region of the jet. Yet, the RDV can resolve those fluctuations at a larger radial distance. The good spatial resolution and the nonintrusive nature of the technique make multi-dimensional turbulence measurements in a compressible flow very promising for the RDV.

5.4 FLOW VISUALIZATION

5.4.1 Flow Visualization in a Uniform Flow

By expanding the laser light into a sheet and shining it into a nearly ideally expanded jet, a luminous pattern can be recognized (Figure 41). In this figure the laser frequency was tuned to resonate with the low velocity region

of the jet. When the laser frequency was tuned to highlight the high velocity portion of the jet, a different pattern can be seen, as shown in Figure 42. Some background fluorescence can also be seen in Figure 41 and 42. This is due to the diffusion of the sodium atoms from the jet to the ambient gas which is not moving.

5.4.2 Flow Visualization in a Structured Flow

When the laser light sheet illuminated an underexpanded jet, a diamond-shaped structure appeared, as shown in Figure 43. Since in a diamond-shaped structure the flow velocity, pressure, and temperature are not uniformly distributed, only those sodium atoms with proper velocity will fluoresce. The luminous regions in Figure 43 are the low velocity regions of the jet. However, velocity is not the only parameter which will affect the fluorescence intensity. The number density of sodium and the broadening of the sodium spectral line are also factors. The bright triangle regions in the photograph are believed to be the regions behind the shocks. It is very bright, not only because the velocity there is low but also because the density there is higher than that in other regions.

By tuning the laser frequency high velocity regions of the flow were high-lighted, as shown in Figure 44. Comparing this photograph with the previous photograph, one can easily see that now the brightest regions largely correspond

Figure 41: Flow Visualization with the Laser Light Sheet Shined into a Nearly Ideally Expanded Jet - Low Velocity

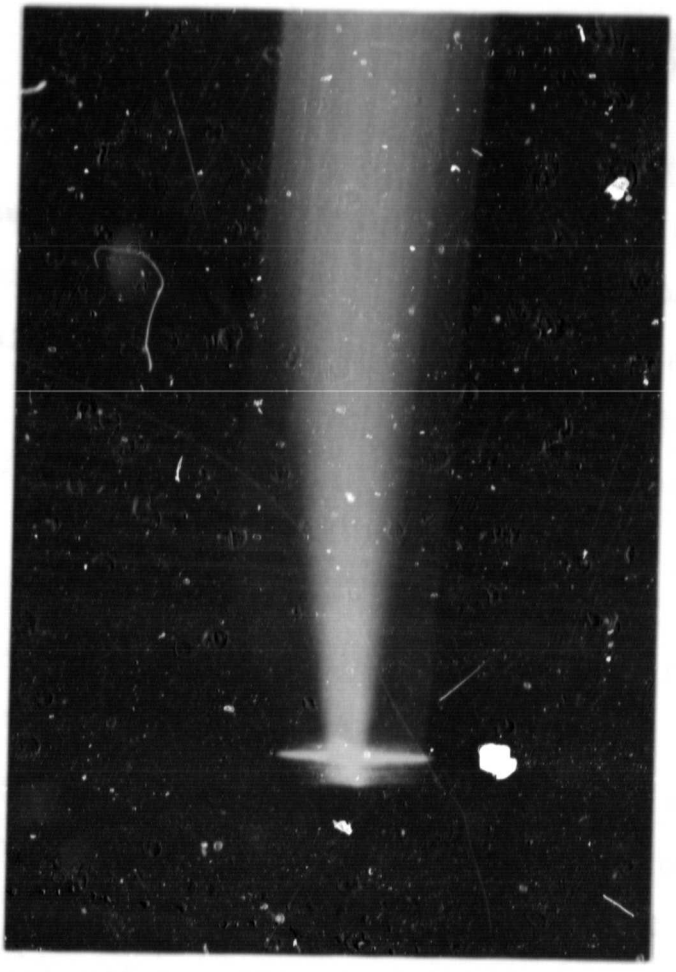

Figure 42: Flow Visualization with the Laser Light Sheet Shined into a Nearly Ideally Expanded Jet - High Velocity

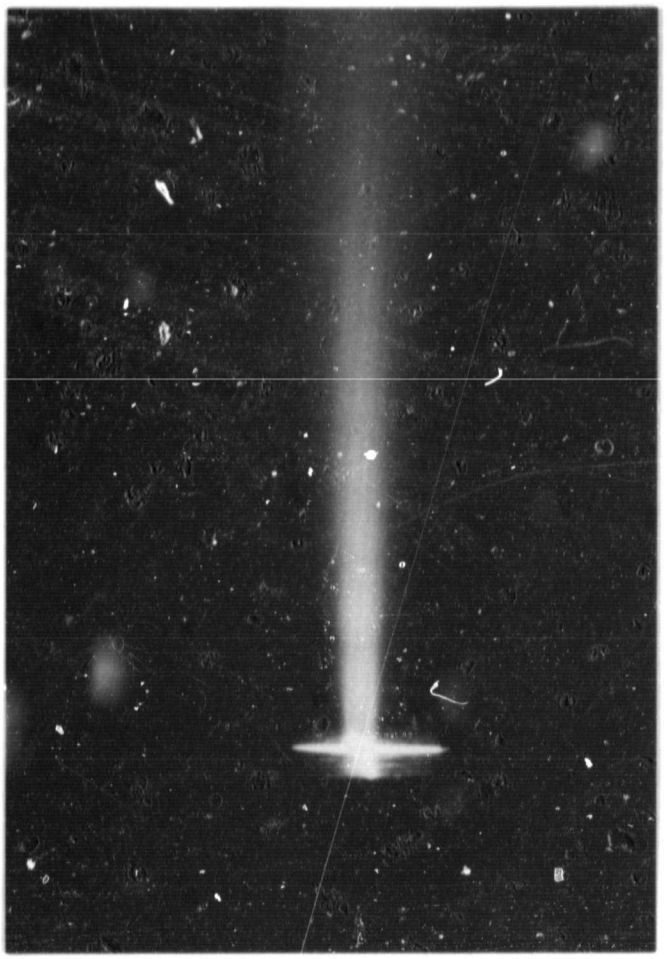

ORIGINAL PAGE
COLOR PHOTOGRAPH

Figure 43: Flow Visualization with the Laser Light Sheet Shined into an Underexpanded Jet - Low Velocity

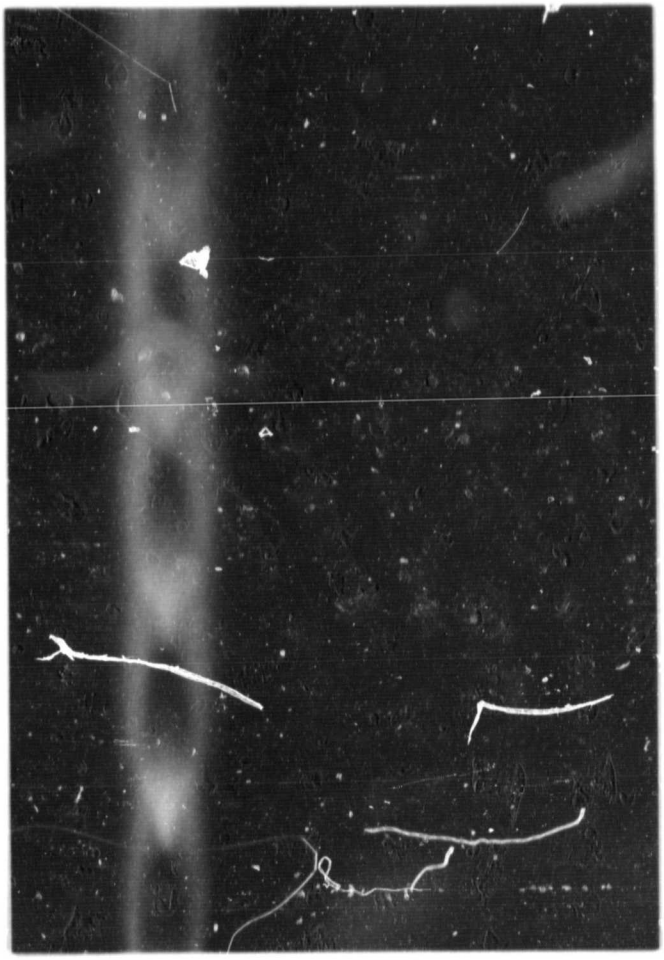

ORIGINAL PAGE
COLOR PHOTOGRAPH

to the darkest regions in the previous photograph. However, the bright triangle regions in the previous photograph remain bright because of the relatively high sodium number density.

When the light sheet was focused onto the jet from the side window, the pattern becomes asymmetric(Figure 45). The asymmetry is present because this flow is an underexpanded jet from a conical nozzle. The flow velocity is not parallel to the center line of the jet. This asymmetric pattern also indicates that the higher contrast is mainly due to the Doppler velocity shift. The broadening effect which will smear out the visualized pattern does not affect the contrast very much. The narrow luminous region downstream shows only faint structure because the laser light missed the cylindrical lens, so it was not focused to a sheet (the black bar across the picture is the shadow of the frame of the cylindrical lens). The integrated effect obscures the flow structure there. Figure 46 is a picture of the same jet with the laser tuned to highlight the high velocity components. Note that the low velocity regions which are the bright regions in the previous photograph are now dark and the bright regions are now the high velocity regions.

Figure 44: Flow Visualization with the Laser Light Sheet Shined into an Underexpanded Jet - High Velocity

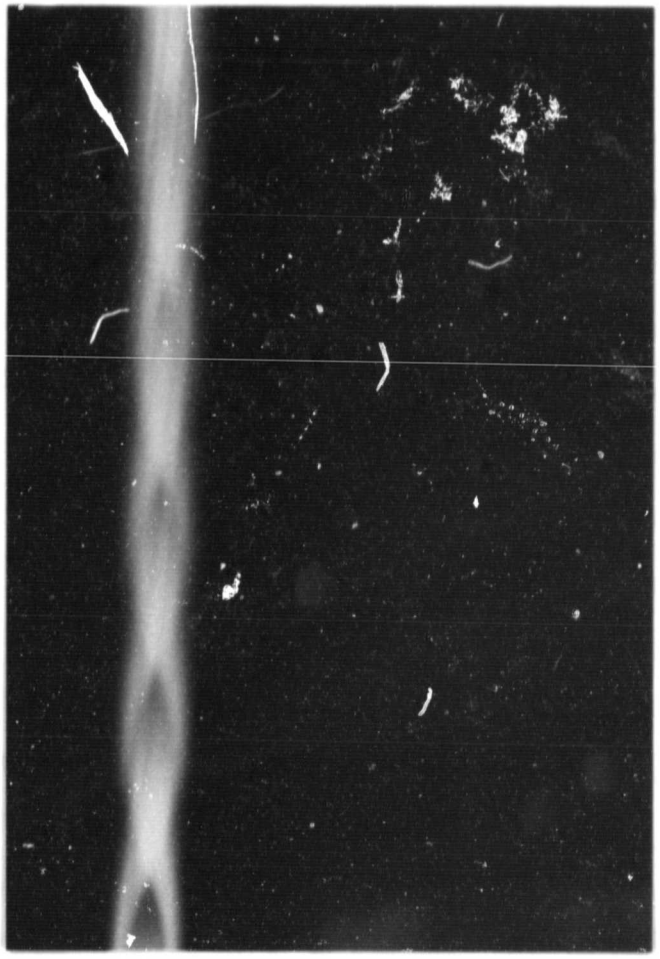

Figure 45: Flow Visualization with the Laser Light Sheet Shined into an Underexpanded Jet from the Side Window - Low Velocity

Figure 46: Flow Visualization with the Laser Light Sheet Shined into an Underexpanded Jet from the Side Window - High Velocity

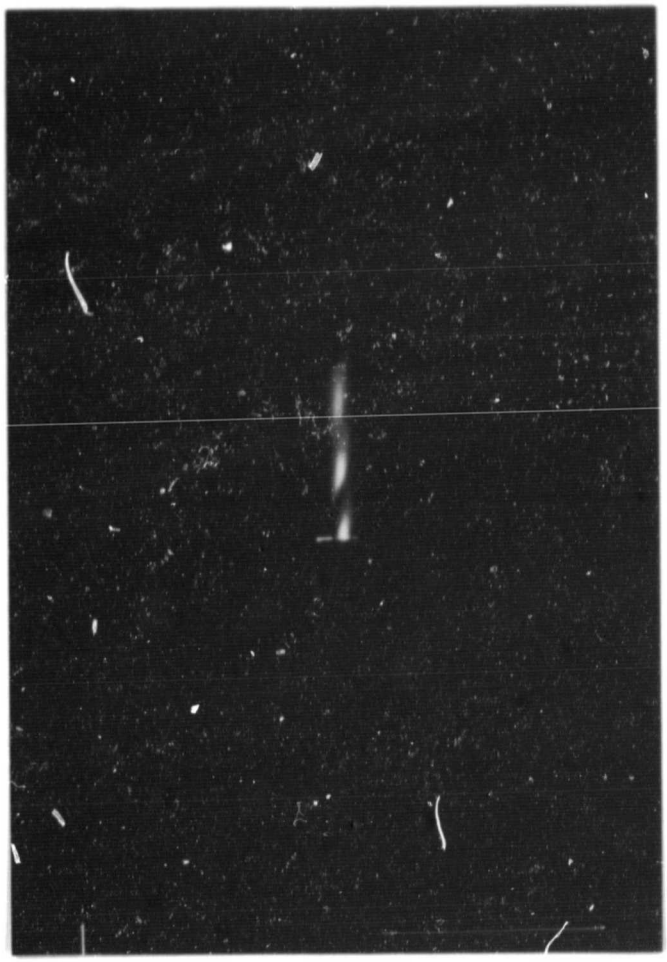

Chapter VI

FUTURE WORK

Besides applying the RDV in a supersonic nitrogen jet, as described in this thesis, and applying it in a hypersonic helium wind tunnel (Zimmermann et al., (1-6)) the RDV can perhaps be developed further for the following applications.

6.1 AIR FLOW

To be able to apply the RDV to air flow is extremely important because most of the flow facilities in industry and research laboratories use air. For air flow, sodium seeding is not appropriate because sodium will react with the water vapor in the air flow. Even though we can use dry air, the number of free sodium atoms which are available will still be very limited because of the large quenching cross section of the oxygen molecules (twice as large as that of the nitrogen molecules) and the chemical reactions (22) such as

$$Na^* + O_2 \dashrightarrow NaO + O$$

or

$$Na + O_2 + M \dashrightarrow NaO_2 + M$$

Some preliminary work on applying the RDV to air flow has been done. Iodine molecules were used as tracer parti-

cles(74). Iodine was chosen because of its very high vapor pressure and its chemical inactivity in the air flow. Iodine has the disadvantage of having a much more complicated molecular structure than sodium. It is also quenched by air, however, the fluorescence signal from the iodine molecules in a low pressure flow is strong enough to be seen with the naked eye.

The diamond-shaped structure of an underexpanded supersonic jet can be easily identified in the photograph shown in Figure 47. This structure is different from Figures 45 and 46 because the laser light was multi-frequency. Thus, more than one velocity group was excited.

6.2 TURBULENCE MEASUREMENTS

The turbulence measurements done in this work is only preliminary. In the future, more quantitative analyses should be made especially in separating out the total fluorescence intensity fluctuations into fluctuations of velocity, temperature, and pressure. From equation IV-9, one may derive that

$$I_\nu'^2 \cong S_V^2 \overline{V'^2} + S_T^2 \overline{T'^2} + S_p^2 \overline{P'^2}$$

$$+ 2S_V S_T \overline{V'T'} + 2S_V S_p \overline{V'P'} + 2S_T S_p \overline{T'P'}$$

By operating the RDV at a minimum of six different frequencies, one may determine all six unknowns. This is a similar method as that employed by the hot wire technique in resolving mass flux and total temperature fluctuations.

Figure 47: Flow Visualization in Iodine Seeded Air Flow

Since the laser frequency is easy to scan, more than a hundred frequency steps can easily be taken across the spectral lines. By averaging the data at each frequency step and fitting the theoretical spectrum across it, one may obtain mean flow properties. The sensitivity curves for this particular spectrum can be derived numerically. Then, the six turbulence parameters($\overline{V'^2}$, $\overline{T'^2}$, $\overline{P'^2}$, $\overline{V'T'}$, $\overline{V'P'}$, $\overline{T'P'}$) can be obtained by least squares fitting the mean square fluctuations across the spectral lines using the sensitivity curves obtained above. Note that to carry out this scheme, a laser with high stability in its frequency must be used because the scan across the spectral lines may take a long time.

The potential of using the saturation spectroscopy for turbulence measurements is worth further investigation. Since when a spectral line is saturated, the fluorescence intensity is a function of density only, thus saturation spectroscopy is useful in isolating the density fluctuation. However, as the laser intensity goes up, the optical pumping might creep in and distort the spectral line shape. A study of the effect of optical pumping or locating other spectral lines which are free of the optical pumping effect would be necessary before the saturation spectroscopy can be employed.

The frequency response of the RDV system in this investigation is limited to about 50 KHz. This limitation comes

from the fact that a photomultiplier is not designed for the detection of high intensity light. A low-noise photo-diode or a low-noise photo-transistor should be employed to extend the frequency response of the RDV system.

6.3 MULTI-DIMENSIONAL MEASUREMENTS

The RDV has so far been applied to one-dimensional measurements only. It is relatively easy to extend its uses to two- or three-dimensional measurements, and some preliminary work has been done to achieve this. The dye laser beam was split into three beams and directed into the nitrogen jet at three different directions. Each of these laser beams was sensitive to the velocity component along its direction. By measuring the three non-coplanar velocity components, the true 3-D velocity vector can be constructed. To distinguish the fluorescence signals from the three laser beams, a precision chopper was used to label the signal. The chopper allowed only one beam to pass through at one time, while a slot detector generated a square wave at three times the "chopping frequency" of each beam(Figure 48). This square wave was used to trigger the photon counter and also served as a timing signal for the computer data acquisition.

The preliminary raw data are shown in Figure 49. This figure is similar to the raw data shown in Chapter III, except that three sodium D_2 lines were detected in this case.

Figure 48: Chopper & the Timing of the Laser Beams

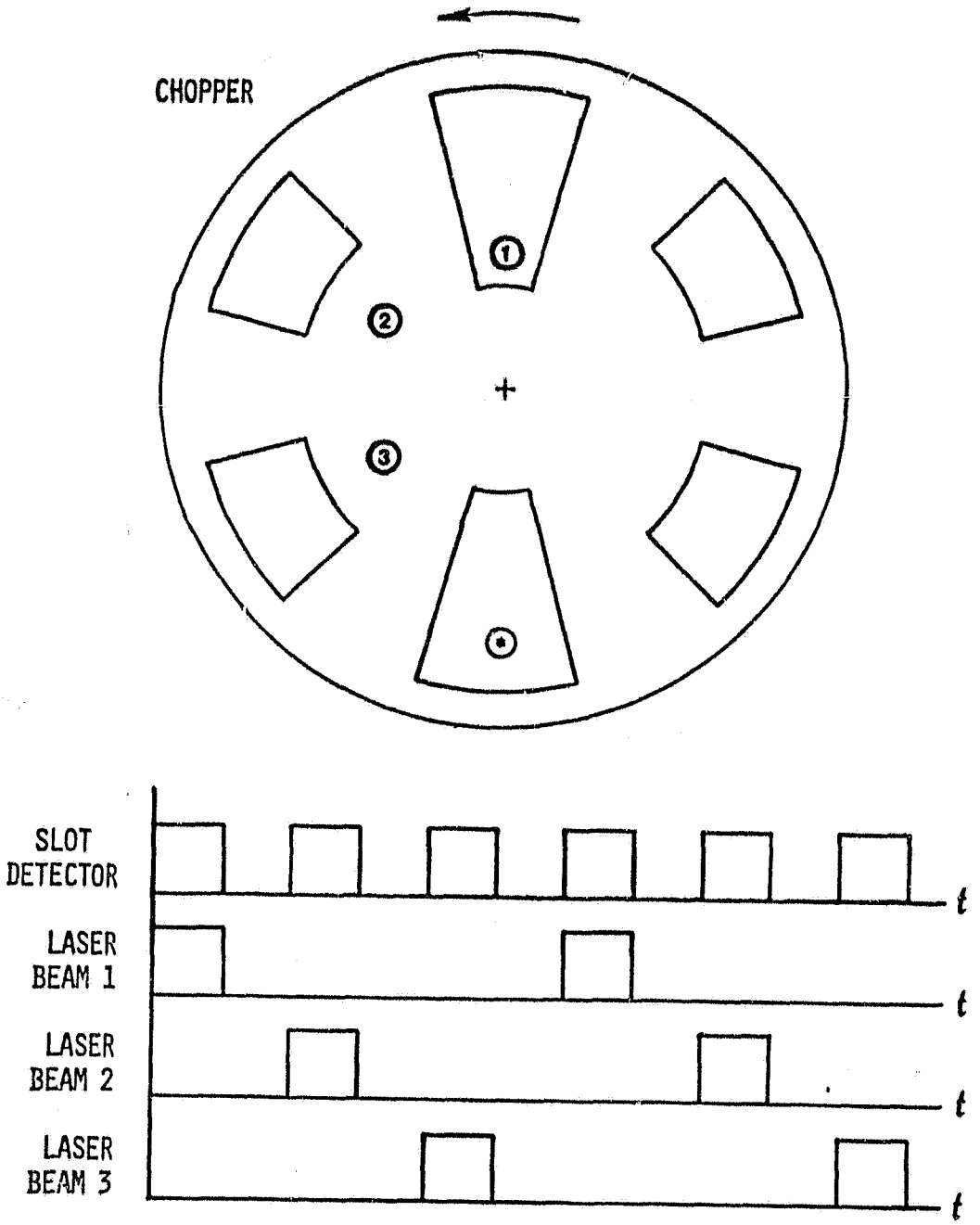

Each of these sodium spectra corresponds to one velocity component of the flow.

Two-dimensional or three-dimensional measurements are important for flow measurement because one-dimensional measurements are not realistic. The preliminary work accomplished here demonstrates that the RDV can easily be applied to multi-dimensional measurements.

6.4 MEASUREMENTS OF SPECIES DENSITY

As discussed in Chapter IV, velocity, temperature, and pressure information is extracted from frequency parameters such as frequency shift and linewidths. The intensity of the fluorescence spectrum also contains some information. Normally, the intensity of the spectral line is directly proportional to the number density of the tracer species(Equation VI-1), which in our case is the number density of the sodium atoms. This relation between the fluorescence intensity and the sodium density is complicated by the quenching effect. Thus one has to determine the quenching cross sections accurately before any reliable measurement of the tracer species concentration can be obtained. If accurate quenching cross sections are not available, saturation spectroscopy, where the spectral intensity is independent of the quenching, can be employed. This saturation LIFS technique has been developed extensively by John Daily(80 - 82).

Figure 49: 3-D RDV Data

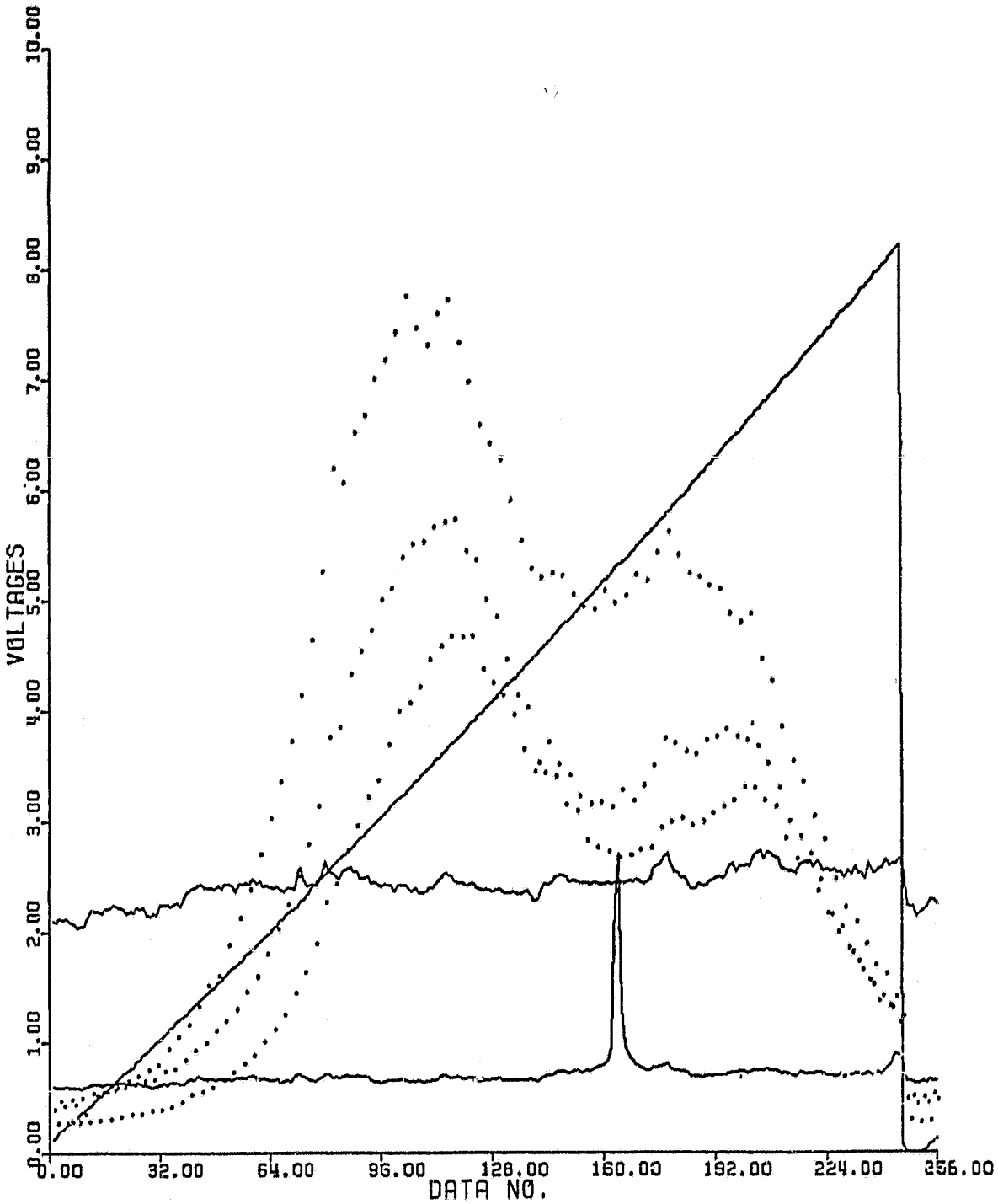

Furthermore, we can develop the RDV for major species number density measurement. As mentioned in the last section, the sodium D_1 line is coupled with sodium D_2 line through the collisional process between the sodium atoms and the nitrogen molecules. Thus the fluorescence intensity ratio of the D_1 and D_2 lines is determined by the number density of the quenching species, i.e., nitrogen. By measuring the fluorescence intensity of D_1 and D_2 lines simultaneously, one may calculate the number density of the major species. The feasibility of applying this technique to sodium-nitrogen system has been investigated by Campbell and Lewis(83). A similar technique has been applied to the hypersonic helium flow by Driscoll(84) using electron beam as the excitation source.

6.5 TWO-PHOTON SPECTROSCOPY

Instead of exciting the sodium atoms from ground 3S states to 3P states, we can excite sodium atoms into 4S or 3D states by using two-photon spectroscopy. The most interesting feature of the two-photon spectroscopy is its Doppler-free characteristic. When the two simultaneously-absorbed photons are propagating in opposite directions, the positive Doppler shift in one photon will be compensated by the negative Doppler shift in the other photon. This will eliminate not only the Doppler shift caused by mean flow motion, but also the Doppler broadening. Therefore, when the

RDV is used for flow visualization, the visualized patterns can be explained unambiguously. A detailed discussion on this subject can be found in Ref. 6.

Chapter VII

CONCLUSIONS

We have demonstrated the usefulness of the RDV in average and turbulent point measurements in a supersonic nitrogen jet. In addition we have shown that it is also useful in flow visualization. Furthermore, broadening and pressure shift cross sections at low temperature can be determined by directing the laser beam perpendicular to the jet. Some preliminary work for future development of this technique has also been presented.

Our conclusions may be summarized as follows:

From the measurements of the broadening and pressure shift cross sections:

1. The measurements indicate that the interaction between the sodium atoms and nitrogen molecules is stronger than the van der Waals interaction, and weaker than the quadratic Stark interaction. If an inverse power law is used to approximate the intermolecular potential, the inverse power N will be about 4.3.
2. The measured broadening cross sections correlate well with those measured recently under high temperature conditions. However, the pressure shift cross sec-

tions measured at high temperature(in the boundary of the jet) are lower than those from the literature. The uncertainty of the pressure shift cross section is very large; about 50% at high temperature. This may be caused by the uncertainty of the jet direction and the finite scanning range of the laser frequency.

3. The pressure shift is not negligible in our flow. a sodium-nitrogen system. It is about 21% of the Doppler shift at the center of the jet, and about 10% at the boundary of the jet. The uncertainty in pressure shift cross section measurements increases the uncertainty in velocity measurements. However, the effect is relatively small; about 5% of the flow velocity.
4. The quenching cross section may be as large as half the broadening cross section, but the quenching effect does not severely affect the RDV measurement since we can easily obtain a visible fluorescence.

Conclusions reached from the measurements of the mean flow properties include:

1. The velocity, Mach number, static pressure, and total temperature measured by the RDV agree well with those measured by the pitot probe and the total temperature probe. The uncertainties of the RDV measurements at the center of the jet are:

	uncertainty	relative uncertainty
velocity	±43 m/sec	5.7%

temperature	$\pm 20^{\circ}K$	18%
pressure	± 1.5 torr	12%
Mach number	± 0.28	8.5%

2. The RDV velocity measurement was systematically higher than pitot tube values. This may be attributed to a small error in the estimated angle between the jet and the laser beam. The much larger discrepancy in the velocity measurements found at the edges of the jet may be explained by the fact that the RDV can only detect flow properties through the presence of sodium atoms. Yet, in the mixing layer essentially all the sodium atoms, seen by the RDV, come from the center part of the jet. Thus the measured velocity is biased towards the higher value.
3. The relatively large uncertainties in the measured flow properties partly arise from the finite frequency scanning of the dye laser. These uncertainties can be greatly reduced by using a better laser with a larger scanning range, and by conducting a two-beam experiment.
4. Measurements in an underexpanded jet were attempted. The results clearly indicate the presence of an oblique shock and an expansion fan. However, because the present RDV measurements are one-dimensional, the three-dimensional nature of these flows makes the quantitative analysis difficult.

5. Since only one beam is required for each dimension, the RDV can be easily extended for 3-D measurements.

The application of the RDV to the turbulence measurements is established in the following aspects:

1. Since the RDV signal is continuous in nature, spectral analysis can be used to analyze the frequency components of the turbulent flow.
2. The frequency response of the RDV technique is limited by the photon statistics. For this work, the frequency response is limited to 50 KHz. By using photo-detectors which can accept higher signal intensity, the frequency response in theory can be extended to mega hertz.
3. The spatial resolution of the RDV is very good. By focusing the laser beam, the probe volume can be smaller than 10^{-5} cc.
4. Since the sensitivity to velocity, temperature, and pressure(or density) is different at different laser frequencies, the fluctuations of these flow properties may be separated by making measurements at six or more laser frequencies. Furthermore, since the velocity sensitivity curve bears three nodes at the extremes of the spectral line, one can easily tell if pressure and temperature fluctuations exist.

Flow visualization using the RDV technique was demonstrated in a nearly ideally expanded jet and an underexpand-

ed jet. From the photographs shown in Chapter V, we learned that

1. Due to spectral line broadening, the observed pattern was determined not only by the velocity distribution but also by the temperature and density distributions. However, in the underexpanded jet, it was the velocity magnitude and direction which played the major role.
2. Since the laser beam was focused into a thin light sheet, and since the light sheet was directed perpendicular to the viewing direction, there was no spatial integration. In other words, the RDV has a much better spatial resolution than most conventional flow visualization techniques.

Appendix A

LASER DOPPLER VELOCIMETRY

The LDV is the most popular laser flow diagnostic technique for velocity measurements. Details of this technique can be found in many places(85 - 88). Only the basic principles will be briefly reviewed here.

Several different types of configurations can be used. Among these the dual beam forward scattering (Figure 50) is the most popular one. From Figure 50, one can easily see how the fringes are formed. The fringe spacing d is determined by the angle between the two beams and the wave length of the laser light, i.e.

$$d = \frac{\lambda}{2\sin(\theta/2)}$$

To get the Mie scattering signal from the flow , one normally has to seed the flow with solid or liquid particles. As the seeding particles pass through this fringe pattern, the scattered light is modulated in frequency. The modulation frequency is:

$$f = U/d$$

where U = particle velocity

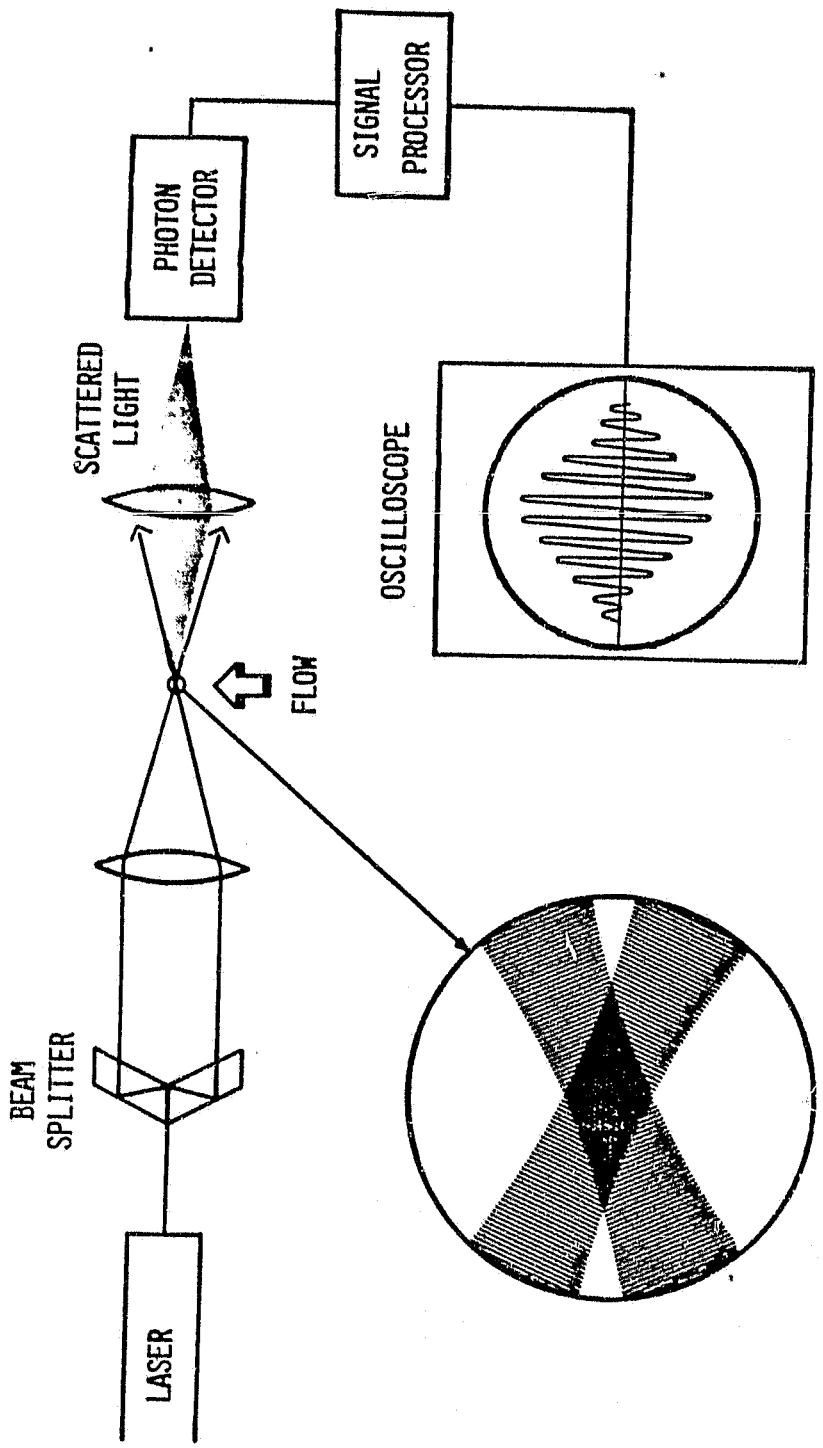

Figure 50: Laser Doppler Velocimetry

This frequency can be found by processing the signal collected by the photomultiplier with a frequency counter. Knowing the fringe spacing, one can calculate the particle velocity. However, the velocity that the LDV measures is the particle velocity, not the velocity of the gas flow. Unless the particle follows the flow closely, the LDV will not be a reliable technique for flow velocity measurement. For particles to follow the flow, they must satisfy the following conditions(89):

$$\omega\tau_p < 1.0$$

$$(\rho_g \omega r_p^2/2u)^{1/2} << 1.0$$

$$\rho_g/\rho_p << 1.0$$

$$Re << 1.0$$

$$K_n \leq 0.5$$

$$\sigma_g \leq 1.5$$

$$m_p n/\rho_g \leq 0.01$$

where τ_p = dynamic relaxation time of the particle
$= \rho_p d_p^2 C_c/18\mu$

C_c = Cunningham correction factor

μ = average viscosity

ω = flow fluctuation frequency

ρ = density

r = radius

K_n = Knudson number = λ_g/d_p

σ_g = standard deviation of the particle size distribution

Re = Reynolds number = $\rho_g(u_g-u_p)d_p/\mu$

n = number density of the aerosol

m_p = average mass of the aerosol

subscripts p and g denote particles and gas flow respectively

In fact, a finite amount of time lag, however small, will always be present. This lag time decreases with the decrease in particle size and particle density. However, other considerations, such as the signal to noise ratio and the molecular slip, will place a lower limit on the particle size. Evidently the LDV is not a very good tool for turbulence with high frequency fluctuations because as the turbulence frequency increases, the particle lag problem will become worse. Furthermore, the measured turbulent frequency spectrum will be biased toward high frequency(90). This is because the high frequency fluctuations will pass through the probe volume many times more than those low frequency fluctuations can in the sampling time interval. It is not well developed for supersonic flow measurements either because , with all sorts of shocks or expansion fans that may exist in the flow, the fidelity of the LDV measurement is low (Figure 51). Besides the limitation of the particle lag, the frequency limit of the photomultiplier becomes a serious problem as the flow velocity is higher than several hundred meters per second. This is simply because the Dop-

pler shift frequency is too large to be handled by the electronic equipments. Figure 52 depicts this problem.

As we can see from this figure, when the flow is supersonic, the scattering angle is limited to a few degree that is, the fringe spacing is very large. In that case, although the Doppler frequency is reduced, the probe volume becomes so large and the number of fringes in the probe volume becomes so small that the measurement is not reliable anymore. Table 7 lists a sample calculation of the LDV parameters in a supersonic case. If an argon-ion laser and a photomultiplier with maximum frequency response of 100 MHz are used, the scattering angle will be limited to about 5 degree. With the conditions given in the table, there are only 16 fringes in the probe volume. With this brief discussion, one can easily see why the LDV, with its great success in subsonic flow, is not very practical in supersonic flow.

Figure 51: Particle Lag behind Normal Shock(92)

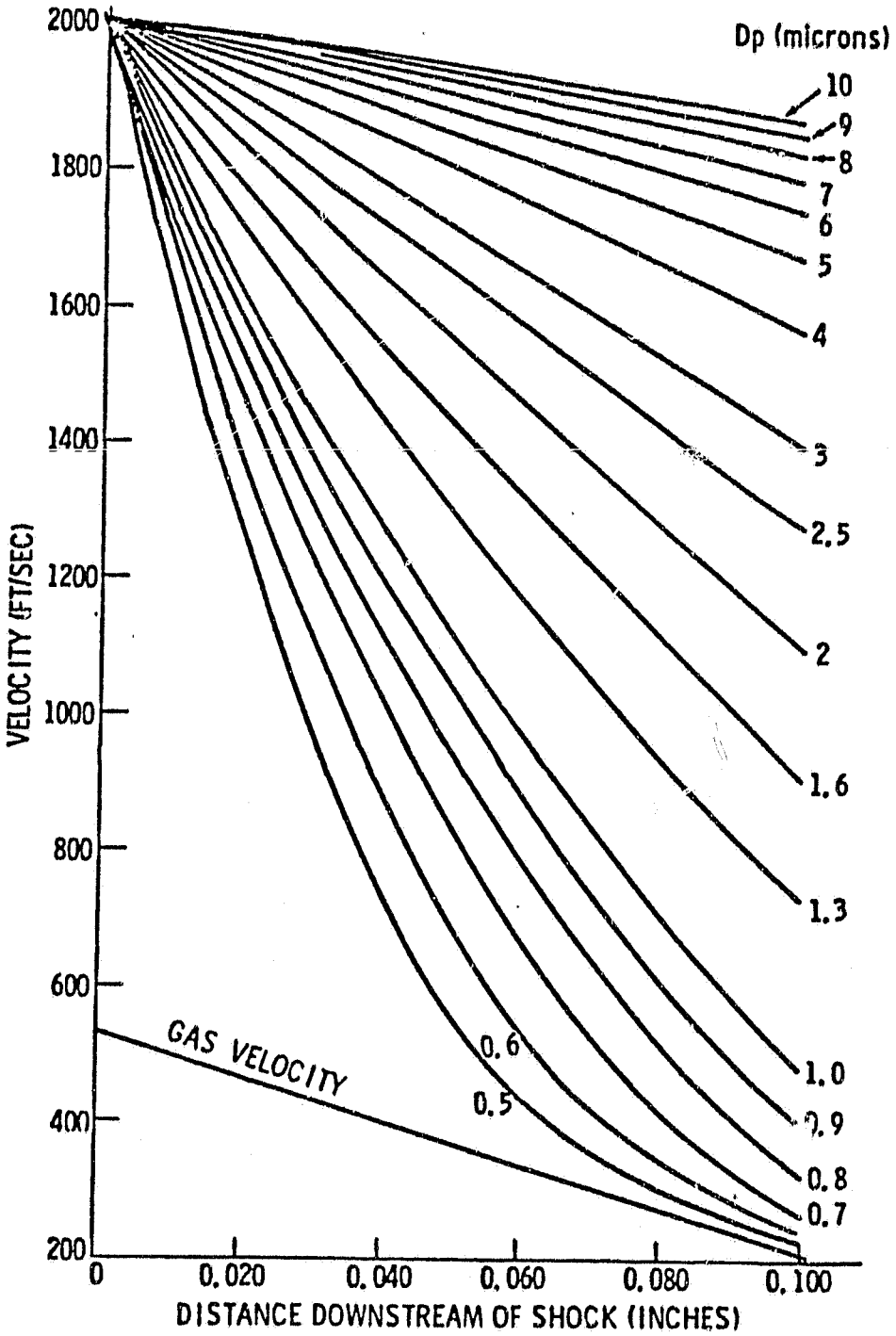

Figure 52: Doppler Frequency Shift as a Function of Scattering Angle

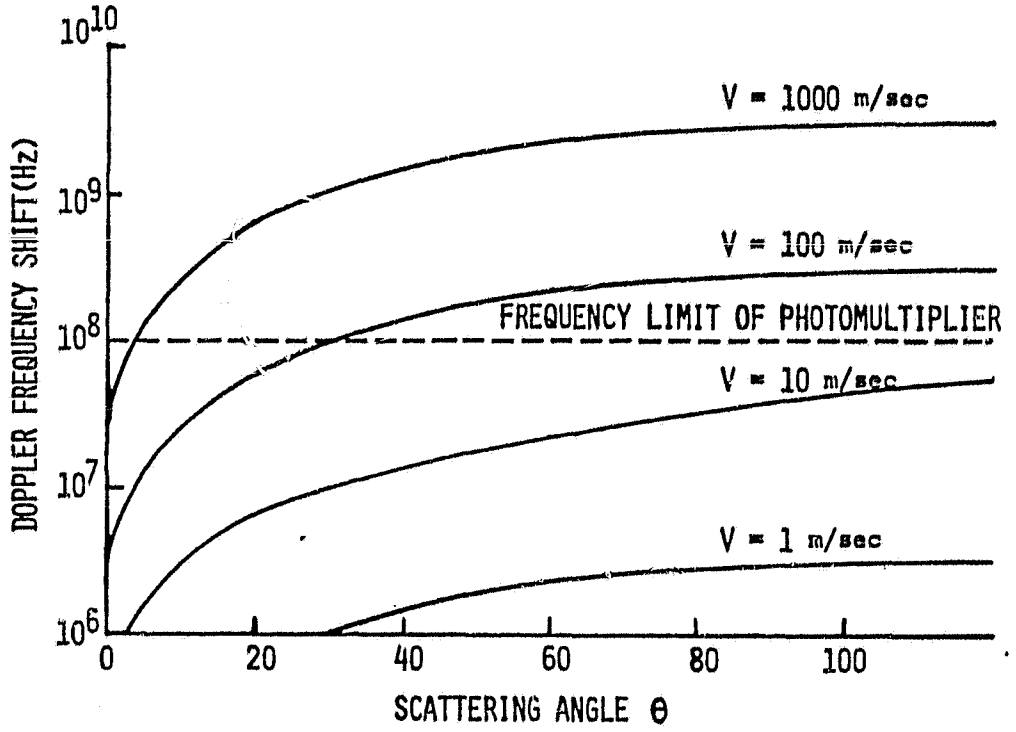

TABLE 7

The LDV in Supersonic Flow

WAVE LENGTH (Å) =	5145.00
BEAM DIAMETER (mm) =	1.50
FOCAL LENGTH (cm) =	20.00
FLOW VELOCITY (m/s)=	650.00

BEAM SEPARATION (cm)	ANGLE (deg)	FRINGE SPACING (μm)	DOPPLER FREQUENCY (MHz)	dX,dY (mm)	dZ (mm)	NO. OF FRINGES
.2	.57	51.45	12.63	.109	21.836	2
.4	1.15	25.73	25.27	.109	10.919	4
.6	1.72	17.15	37.90	.109	7.279	6
.8	2.29	12.87	50.52	.109	5.460	8
1.0	2.86	10.29	63.15	.109	4.369	10
1.2	3.44	8.58	75.77	.109	3.641	12
1.4	4.01	7.35	88.38	.109	3.121	14
1.6	4.58	6.44	100.99	.109	2.732	16
1.8	5.15	5.72	113.59	.109	2.429	19
2.0	5.72	5.15	126.18	.109	2.186	21

Appendix B

HOT WIRE TECHNIQUE

The hot wire anemometer is among the most versatile and widely-used instruments for measuring fluctuating velocities. Their popularity stems from the small sampling volume, fast response, high sensitivity, and relatively low cost. They can be applied to supersonic flow measurements as well as subsonic flow measurements. In the past thirty years, there have been a tremendous number of studies on this subject (93 - 96). Only the basic principles of the technique will be discussed here. Attention will be focused on its application to supersonic flows.

Hot-wires are electrically-heated thin resistive elements, normally circular wires of tungsten, platinum, or platinum alloy. When the fluid flow passes over these sensing elements, the flow properties can be derived from the forced convective heat loss from the wires. The hot wire sensor can be operated in either a constant current or a constant temperature mode. In the constant current operation, a current through the wire is maintained constant and the wire voltage is measured. In the constant temperature system, the wire temperature is maintained constant by employing a feedback amplifier. Since the wire properties

such as thermal inertia, overheat ratio, etc. are constant in constant temperature mode, a constant temperature system is easier to operate than a constant current system. Since the system we used was a constant temperature system, the discussion in this Appendix will be limited to the constant temperature system.

The circuit for the constant temperature system is shown in Figure 53. The output of the system is the voltage output of the amplifier, which is the voltage required to drive the necessary current through the sensor. The variable resistor R_3 is used to set the overheat ratio. When the sensor operates, R will fluctuate with the fluctuations in the flow velocity or flow properties. This will imbalance the bridge. With the amplifier striving to maintain $e_2=e_1$, the current i will vary to restore the original R value. Since we can not operate the system with zero mean voltage, an offset voltage e_{offset} is used to establish a mean current through the system. To test the frequency response of the system, a square-wave test signal e_t is introduced into the sensing element.

As was mentioned earlier, the principle of the hot wire is the energy balance between the heat loss and the electrical energy input. The input power to the sensor is

$$i_1 e_1 = \frac{e_1^2}{R} = \left(\frac{R}{R+R_1}\right)^2 \frac{e_o^2}{R} = \frac{R}{(R+R_1)^2} e_o^2$$

$$R = R_o\{1+\alpha(T-T_{ref})\}$$

where R_o = resistance of the sensor at reference

Figure 53: Schematic of Constant Temperature Hot Wire Anemometer

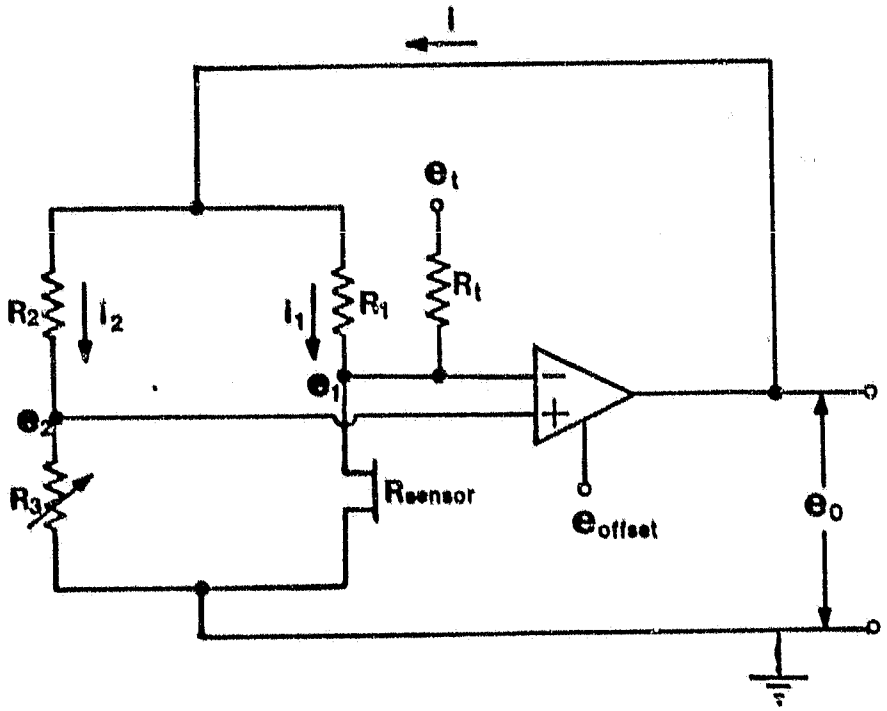

temperature

α = thermal coefficient of the resistance

T_{ref} = reference temperature

T = wire operating temperature

With free convection, conduction, and radiation losses being neglected, the heat loss from the cylindrical wire is

$$q = q_{conv} = hs(T-T_o)$$
$$= NuK_f \pi l(T-T_o)$$

where $Nu = Nu(Re, Pr, Ma, Gr, Kn, (l/d), \tau, \gamma, \theta)$

$$\approx \{A(Pr, \tau)+B(Pr, \tau)Re^n\}(1+\tau/2)^m$$

and h = convective heat transfer coefficient

K_f = thermal conductivity of the fluid

d = diameter of the wire

l = length of the wire

T = wire operating temperature

T_o = stagnation temperature of the fluid

Nu = Nusselt number

Re = Reynolds number

Pr = Prandtl number

Ma = Mach number

Gr = Grashof number

Kn = Knudson number

τ = overheat ratio = $(T-T_o)/T_o$

γ = ratio of specific heats of the fluid

θ = angle between the sensor and the flow velocity

The last relation is the generalized King's law with the coefficients shown in Table 8.

TABLE 8

Coefficients in Generalized King's Law(96)

Re	A	B	n	m	Ref.
Re<40	0.24	0.56	0.45	0.17	(a)
Re>40	0.	0.48	0.51	0.17	(a)
1<Re<4	0.	0.89	0.33	0.08	(b)
4<Re<40	0.	0.82	0.38	0.09	(b)
40<Re<400	0.	0.62	0.47	0.12	(b)
0.1<Re<1000	0.32	0.43	0.52	0.	(c)

(a) D.C. Collis & M.J. Williams, J. Fluid Mech. 6, 357 (1959).
(b) R. Hilpert, Waermeabgabe von geheizten Draehten und Rohren, Luft, Forsch, Arb, Ing. Wes. 4, 215 (1933).
(c) W.H. McAdams, "Heat Transmission", Chap. 10, McGraw-Hill, 1954.

The output voltage e_o is

$$e_o = (R+R_1)\left\{\frac{Nu\pi K_f l(T-T_o)}{R}\right\}^{1/2}$$

Note that not only the flow velocity, but also the flow temperature, flow density, and the flow direction will affect the output voltage. Moreover, the nonlinear nature of the relation makes the calibration extremely important for hot wire measurements.

When applying the hot wire technique to the supersonic flow, three problems were identified by L. S. G. Kovasznay (97, 98).

1. A higher frequency response is required.

2. A new heat loss law is needed.

3. Three independent flow parameters are required.

The first problem is solved automatically with the development of the constant temperature technique because a constant temperature has a very high frequency response (>100 KHz). For the second problem, Kovasznay(97) has derived an empirical form of the heat loss at supersonic velocities

$$q = (A+BRe^{1/2})(1-C\frac{T-T_{rec}}{T_o})\pi l K_f(T-T_{rec})$$

where T_{rec} = recovery temperature

$C = 0.18$

$A = 0.580$

$B = -0.795$

Therefore, in supersonic flow, the heat loss law is basically the same as that in the subsonic flow. It depends on the mass flux ρU and the stagnation temperature, and is independent of Mach number. The only difference from the subsonic case is an additional temperature dependent term.

The third problem is an intrinsic property of supersonic flow. Because the flow is compressible, there is an additional independent variable. Therefore, an additional assumption is required. Further information can be found in other studies (94 - 101).

Appendix C

MODIFIED VOIGT PROFILE

As described in Chapter II, the Voigt profile is the convolution of a Lorentzian profile and a Gaussian profile, and the expressions for these two profiles are:

$$(I_\nu)_L = I_o \cdot \frac{(\Delta\nu_L/2)^2}{(\nu-\nu_o-\Delta\nu_{sp}-\Delta\nu_{sD})^2+(\Delta\nu_L/2)^2}$$

$$(I_\nu)_G = I_o \exp\{-\frac{c^2(\nu-\nu_o)^2}{\nu_o^2 \cdot \bar{u}^2}\}$$

where $\Delta\nu_L = N\sigma_b\bar{v}$

$\Delta\nu_{sp} = N\sigma_s\bar{v}$

In the same chapter, it was also mentioned that the broadening collision cross section and pressure shift cross section were temperature dependent. Strictly speaking, they are functions of the relative velocity of the perturber and the absorber.

$$\Delta\nu_L = N\langle\sigma_b v_r\rangle$$

$$\Delta\nu_{sp} = N\langle\sigma_s v_r\rangle$$

Since v_r depends on the velocity of the absorber v, the convolution procedure described in Chapter II for Voigt profile is mathematically inconsistent(109). This inconsistency can

lead to a serious error in the resulted line profile. But under certain conditions, the Voigt profile can still be treated as a good approximation. If we take these velocity-dependent broadening and shift effects into account, the resulted profile is called Modified Voigt Profile(MVP) or Speed Dependent Voigt Profile(SDVP)(102 - 108).

The most general expression for MVP was given by Paul Berman (102). The profile he derived is:

$$I(\delta) = \pi^{-3/2}\int_{-\infty}^{\infty} \frac{e^{-z^2}\cdot \eta(z)}{\eta(z)^2+\{\xi(z)-z\}^2}$$

$$-\pi^{-3/2}\int_{-\infty}^{\infty} dz.e^{-z^2}.z.\frac{\{z^2+\eta(z)^2-\xi(z)^2\}\frac{d\eta}{dz} + \frac{2\eta(z)\xi(z)\frac{d\xi}{dz}}{\{\xi(z)+z\}^2}}{\{\eta(z)^2+\{\xi(z)-z\}^2\}\{\eta(z)^2+}$$

where $z = v/u$

$y = kuz\tau$

$\eta(z) = \{\Delta\nu_L(uz)\}/ku$

$\delta = (\nu-\nu_o)/ku$

$\xi(z) = \{\nu-\nu_o-\Delta\nu_{sp}(uz)\}/ku$

$\alpha(z) = \eta(z)+i\xi(z)$

The first term is the simple Voigt profile and the second term is a complicated modified term for the Voigt profile.

However, the velocity-dependent effect is easier to understand if we follow the derivation of Herbert Pickett(103).

If we assume the velocity-dependency of the broadening collision rate to be of the form

$$R_b = (\Delta\nu_L/N) = \langle\sigma_b\bar{v}_r\rangle = K_b v_r^n$$

then

$$R_b(v) = \int_0^\infty f(v_r/v)R_b(v_r)dv_r = R_{bo}M(-n/2,3/2,x^2)$$

where $f(v_r/v)$ = distribution function for relative velocity v_r of the perturbing molecule with respect to an absorbing molecule with velocity v

$$= \frac{4v_r}{\pi v\bar{v}_p}\sinh(8vv_r/\pi\bar{v}_p^2)\exp\{-4(v^2+v_r^2)/\pi\bar{v}_p^2\}$$

v_p = rms speed of the perturber

$$R_{bo} = \bar{R}_b\left(\frac{m_a}{m_a+m_p}\right)^{n/2} = \bar{R}_b(1-m^*)^{n/2}$$

$$m^* = m_p/(m_a+m_p)$$

M = confluent hypergeometric function

$$x = v\sqrt{m_p/2kT}$$

and subscripts a and p denote the absorber and the perturber, respectively.

The same relation can be applied to pressure shift.

$$R_s = K_s v_r^s$$

$$R_s(v) = R_{so}M(-s/2,3/2,x^2)$$

The resulted MVP is:

$$I(\delta) = \int_0^\infty \frac{NR_b(v)}{N^2R_b^2(v)+\{\delta-NR_s(v)\}^2} f(v)dv$$

where δ = frequency offset from the resonance

As one can easily see from these equations, the important parameters which will determine how good an approximation Voigt profile is are n, s, and m*.

The velocity-dependent effect on the shape of the spectral lines has been discussed extensively by R. J. Lovett and M. L. Parsons (105). Generally speaking, it does not affect the line wings but will make the spectral line sharper at the line center, that is, the peak will be higher and the full width at half maximum will be smaller. The effect is shown in Figure 54.

If the mass of the absorber is much larger than that of the perturber, that is, m*-->0, the Voigt profile will always be a good approximation for any value of n or s. But as m* approaches 1, that is, the perturber becomes heavier than the absorber, the error produced by using Voigt function as the line profile can be as large as 30%.

Another important feature of the MVP is the prediction of the asymmetry of the line profile. The asymmetry is caused by the velocity-dependence of the pressure shift. But because the analysis of MVP with velocity-dependent shift is very complicated and because the effect of asymmetry is normally not very pronounced at low pressure under which the spectroscopic analysis is employed, this problem is normally neglected.

Unfortunately, to the knowledge of the author, the MVP can not be evaluated at this time by other than direct nu-

Figure 54: Velocity Dependent Effect on the Line Shape(103)

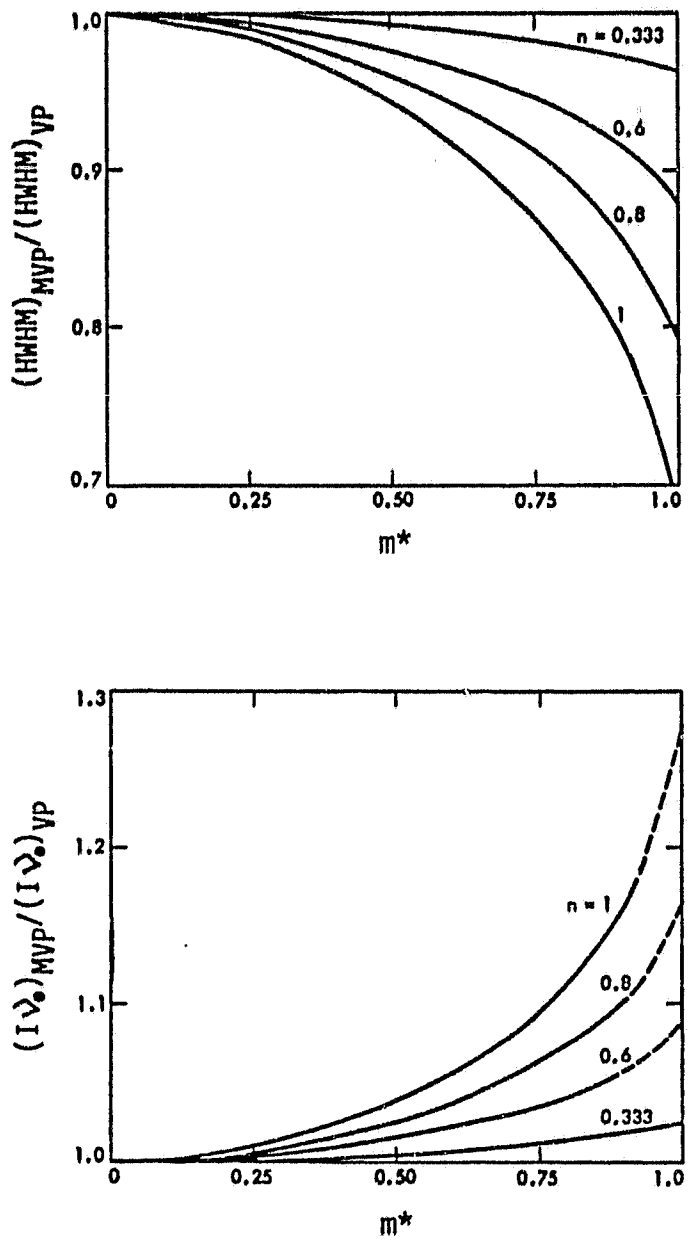

merical integration methods. This fact, along with the uncertainty in the velocity-dependencies of broadening and shift and normally-small deviation of the line shape from the Voigt profile, makes the effort to incorporate MVP for spectral line shape analysis a not very attractive job. However, it is certain enough that if a precise spectral analysis is required or if the deviation is too large to be neglected, MVP should be imposed.

Appendix D

TEMPERATURE AND VELOCITY DEPENDENCIES OF COLLISION CROSS SECTIONS

The theories mentioned in Chapter II imply that the broadening collision cross section and pressure shift collision cross section have the same temperature-dependence if the intermolecular potential is given in the form of inverse power law. That is,

$$P.E. = a/r^N$$

However, the semi-classical treatment of the impact approximation given by Frost et al.(111 - 113) has shown that the shift is obtainable only in second-order Born approximation. But the broadening is obtainable in first-order Born approximation. Consequently, the temperature-dependencies are different for these two types of cross sections.

When employing this new treatment, the resulted temperature-dependence of broadending cross sections is the same as that derived from Lindholm's theory

$$\sigma_b \propto T^{-\frac{1}{N-1}} \qquad (D-1)$$

while the temperature-dependence of the shift cross sections is(103):

$$\sigma_s \propto T^{-\frac{N+2}{2(N-1)}}$$

The temperature-dependencies of these cross sections are not very meaningful physically, because the relative velocity is the true factor that determines the collision effect. The velocity-dependencies of these cross sections can be obtained through the following transformation:

Let $\sigma = \sigma(T) = aT^{\alpha}$,

since $\sigma(T) = \int_0^{\infty} \sigma(v) \cdot f(v) \cdot dv$

$$= \int_0^{\infty} \sigma(v) \left(\frac{m}{2\pi KT}\right)^{3/2} \exp\left(-\frac{1}{2}\frac{mv^2}{K\pi}\right) 4\pi v^2 dv$$

$$= \int_0^{\infty} \sigma(v) \frac{2}{\sqrt{\pi}} \frac{v}{\sqrt{\frac{2K}{m}}} \frac{1}{T^{3/2}} \exp\left(-\left(\frac{v}{\sqrt{2K/m}}\right)^2 \frac{1}{T}\right) \cdot d\left(\frac{v}{\sqrt{2K/m}}\right)^2$$

thus, if let $s = 1/T$ and $x = \left(\frac{v}{\sqrt{2K/m}}\right)^2$,

then $\sigma(T) = as^{-\alpha} = \frac{2}{\sqrt{\pi}} \int_0^{\infty} \sigma(x) x^{1/2} s^{3/2} \exp(-sx) dx$

$$as^{-(\alpha+3/2)} = \frac{2}{\sqrt{\pi}} \int_0^{\infty} \sigma x^{1/2} \exp(-sx) dx$$

By employing the inverse Laplace transformation, we may obtain

$$ax^{(\alpha+3/2)-1} = \frac{2}{\sqrt{\pi}} \sigma x^{1/2}$$

Therefore,

$$\sigma = a \cdot \frac{\sqrt{\pi}}{2} \cdot \left(\frac{m}{2K}\right)^{\alpha} \cdot v^{2\alpha}$$

$$= \text{const} \cdot v^{2\alpha}$$

The temperature- and velocity-dependencies of the broadening and shift cross sections are tabulated in Table 9 for some special types of interaction.

TABLE 9

Temperature & Velocity Dependences of Collision Cross Sections

N	$\sigma_b(T)$	$\sigma_b(v)$	$\sigma_s(T)$	$\sigma_s(v)$
N=∞ Hard Sphere	T^0	v^0	$T^{-0.5}$	v^{-1}
N=6 van der Waals	$T^{-0.2}$	$v^{-0.4}$	$T^{-0.8}$	$v^{-1.6}$
N=4 Quadratic Stark	$T^{-0.333}$	$v^{-0.667}$	T^{-1}	v^{-2}
N=3 Dipole	$T^{-0.5}$	v^{-1}	$T^{-1.25}$	$v^{-2.5}$

REFERENCES

1. R. B. Miles, "Resonant Doppler Velocimter", AGARD CP-193, 20-1, May 1976.

2. R. B. Miles, "Resonant Doppler Velocimter", Phys. of Fluids, Vol. 18, No. 6, p751, June 1975.

3. R. B. Miles, E. Udd, & M. Zimmermann, "Quantitative Flow Visualization in Sodium Vapor Seeded Hypersonic Helium", Appl. Phys. Lett. 32(5), March 1978.

4. M. Zimmermann & R. B. Miles, "Hypersonic Helium Flow Field Measurements with the Resonant Doppler Velocimeter", Appl. Phys. Lett. 37(10), p885, 15 Nov. 1980.

5. M. Zimmermann & R. B. Miles, "Low Temperature He-Na Collision Rate Measurement", J. of Phys. B, Atom. Molec. Phys., 14, L85, 1981.

6. M. Zimmermann, "Resonant Doppler Velocimeter", Ph.D. thesis, Princeton University, March 1980.

7. M. Zimmermann & R. B. Miles, "Velocity Temperature and Density Measurements and Flow Visualization: Modeling and Experiments in Hypersonic Flow", To be published.

8. R. C. Weast, "Handbook of Chemistry and Physics", C. R. C., 1976-1977.

9. N. I. Sax, "Dangerous Properties of Industrial Materials", Reihold.

10. E. L. Lewis & L. F. NcNamara, "Broadening of the D lines and the Relaxation of the Resonance Levels of Sodium Due to Collisions with Helium", Phys. Rev. A, vol. 5, No. 6, June 1972.

11. W. M. Fairbanks, Jr., T. W. Hansch & A. L. Schalow, "Absolute Measurement of Very Low Sodium-vapor Densities Using Laser Resonance Fluorescence", J. Opt. Soc. Amer., vol. 65, #2, p199, February 1975.

12. R. G. Breene, "Shift and Shape of Spectral Lines", Pergamon, 1961.

13. R. G. Breene, "Theories of Spectral Line Shape", John Wiley, 1981.

14. H. R. Griem, "Plasma Spectroscopy", McGraw-Hill, 1964.

15. M. Baranger, "Spectral Line Broadening in Plasmas in Atom & Molecular Processes", Academic Press, 1962.

16. W. R. Hindmarsh & J. M. Farr, "Collision Broadening of Spectral Lines by Neutral Atoms", Progress in Quantum Electronics, 2, 143, 1972.

17. A. P. Thorne, "Spectrophysics", Chapman and Hall, 1974.

18. A. E. Siegman, "An Introduction to Lasers and Masers", McGraw-Hill, 1971.

19. S. Chen & M. Takeo, Broadening and Shift of Spectral Lines Due to the Presence of Foreign Gases", Rev. Mod. Phys., 29, p20, 1957.

20. I. V. Hertel, H. Hofman & K. J. Rost, "Elctronic to Vibrational Energy Transfer in the Differential Scattering of Na", Phys. Rev. Lett., 36, 15, p861, 1976.

21. I. V. Hertel, H. Hofman & K. A. Rost, "Crossed Beam(E-VRT) Energy Transfer Experiment", J. Chem. Phys., 71, 2, p674, 1979.

22. J. A. Silver, N. C. Blais & G. H. Kwei, "Crossed Beam Studies of the Dynamics of Electronic Energy Transfer: Quenching of Na($3p^2P_{1/2}$) Atoms by N_2, O_2, CO, and NO Molecules", J. Chem. Phys., 71, 8, 1979.

23. E. R. Fisher & G. K. Smith, "Vibration-Electronic Coupling in the Quenching of Electronically Alkali Atoms by Diatomics", Appl. Opt., 10, 8, p1803, 1971.

24. E. Bauer, E. R. Fisher & F. R. Gilmore, "De-excitation of Electronically Excited Sodium by Nitrogen", J. Chem. Phys., 51, 10, p4173, 1969.

25. E. R. Fisher & G. K. Smith, "Alkali Quenching in High Temperature Environments", Chem. Phys. Lett., 13, 5, p448, 1972.

26. J. R. Barker, "A Modified Model for Quenching and Electronic-Vibrational Energy Transfer", Chem. Phys., 18, p175, 1976.

27. C. Bottcher & C. V. Sukumar, "Quenching of Excited Atoms by Collisions with Stable Molecules", J. Phys. B, 10, 14, p2853, 1977.

28. E. A. Gislason, A. K. Keleyn & J. Los, "Calculation of the Vibrational Distribution in Quenching of Na(3^2P) by N_2 and CO", Chem. Phys., 59, p91, 1981.

29. A. Bjerre & E. E. Nikitin, "Energy Transfer in Collisions of an Excited Sodium Atom with Nitrogen Molecule", Chem. Phys. Lett., 1, p179, 1967.

30. D. R. Jenkins, "The Determination of Cross Sections for the Quenching of Resonance Radiation of Metal Atoms-I. Experimental Method and Results for Sodium", Proceedings of Roy. Soc., 293, p1435, 1966.

31. P. L. Lijnse & R. J. Elsenaar, "The Temperature Dependence of the Quenching Flames of 1500-2500^oK", JQSRT, 12, p1115, 1972.

32. H. P. Hooymayers & P. L. Lijnse, "The Relationship between the Fluorescence Yield and the Underpopulation of Doublet Excited States", JQSRT, 9, p995, 1969.

33. M. Czajkowski, L. Krause & G. M. Skardis, "Quenching of Mercury-Sensitized Fluorescence in Sodium, Induced in Collisions with N_2 Molecules", Can. J. Phys., 51, p1582, 1973.

34. B. P. Kibble, G. Copley & L. Krause, "Inelastic Collisions between Excited Alkali Atoms and Molecules-II. The Quenching of Sodium Resonance Radiation by N_2, H_2, HD, and D_2", Phys. Rev., 150, 1, p159, 1967.

35. J. R. Barker & R. E. Weston, "Energy-Dependent Cross Sections for Quenching of Na($3p^2P$) by Several Gases", J. Chem. Phys., 65, 4, p1427, 1976.

36. E. A. Andreev, "Energy Transfer in N_2-Alkali Collisions", Chem. Phys. Lett., 23, 4, p516, 1973.

37. M. J. Jongerius, A. R. D. Van Bergen, Tj. Hollander & C. Th. J. Alkemade, "An Experimental Study of the Collisional Broadening of the Na-D Lines by Ar, N_2, and H_2 Perturbes in Flames and Vapor Cells-- I. The Line Core", JQSRT, 25, p1, 1981.

38. P. L. Lijnse, "Temperature Dependence of the Quenching of the Na-D-Doublet by Nitrogen Molecules", Chem. Phys. Lett., 18, 1, p73, 1973.

39. V. S. Letokhov & V. P. Chebotayev, "Nonlinear Spectroscopy", chapter 1, Springer-Verlag, 1977.

40. J. L. Hall, "Lectures in Theoretical Physics", vol. XII-A, p161, Ed. K. T. Mahanthapa, W. Z. Brittin, 1971.

41. A. Yariv, "Introduction to Optical Electronics", Holt, Rinehart & Winston Inc., 1971.

42. H. A. Lorentz, I, II, Versl. Amsterdam Acad., 14, 518,577, 1905.

43. V. Weisskopf, Z. Physik, 75, 287, 1932.

44. E. Lindholm, Uber Verbreiterung und Verschiebung Von Spektrallinien Dissertation, Uppsala, 1942.

45. P. W. Anderson, Phys. Rev., 76, p647, 1949.

46. A. Corney, "Atomic and Laser Spectroscopy", Clarendon Press, 1977.

47. I. V. Hertel & W. Stoll, "Collision Experiments with Laser Excited Atoms in Crossed Beams", Adv. At. Mol. Phys., 13, p113, 1978.

48. I. V. Hertel & W. Stoll, "Principles and Theoretical Interpretation of the Electron Excitation by Laser Excited Atoms", J. Phys. B, 7, p570, 1974.

49. R. Walkup, A. Spielfiedel, W. D. Phillips, & D. E. Pritchard, "Line-shape Changes due to Optical Pumping of Na in Buffer Gas", Phys. Rev. A, Vol. 23, No. 4, p1869, April 1981.

50. J. K. Kielkopf, "New Approximation to the Voigt Function with Applications to Spectral-Line Profile Analysis", J. of Opt. Soc. of Amer., vol. 63, No. 8, p987, 1973.

51. C. Young, "Calculation of the Absorption Coefficient for Lines with Combined Doppler and Lorentz Broadening", JQSRT, vol. 5, p549, 1965.

52. B. H. Armstrong, "Spectrum Line Profiles: The Voigt Function", JQSRT, vol. 7, p61, 1967.

53. E. E. Whiting, "An Empirical Approximation to the Voigt Profile", JQSRT, vol. 8, p1379, 1968.

54. S. R. Drayson, " Rapid Computation on the Voigt Profile", JQSRT, vol. 16, p611, 1976.

55. J. J. Oliver & R. L. Longbothum, "Empirical Fits to the Voigt Line Width: A Brief Review", JQSRT, vol. 17, p233, 1977.

56. J. H. Pierluissi & P. C. Vanderwood, "Fast Calculational Algorithm for the Voigt Profile", JQSRT, vol. 18, p555, 1977.

57. A. K. Hui, B. H. Armstrong & A. A. Wray, "Rapid Computation of the Voigt and Complex Error Functions", JQSRT, vol. 19, p509, 1978.

58. A. H. Karp, "Efficient Computation of Spectral Line Shapes", JQSRT, vol. 20, p379, 1978.

59. J. Humlicek, "An Efficient Method for Evaluation of the Complex Probability Function: The Voigt Function and Its Derivatives", JQSRT, vol. 21, p309, 1979.

60. J. Puerta & P. Martin, "Three and Four Generalized Lorentzian Approximations for the Voigt Line Shape", Appl. Opt., vol. 20, No. 22, p3923, November 1981.

61. A. Klim, "A Comparison of Methods for the Calculation of Voigt Profiles", JQSRT, vol. 26, No. 6, p537, 1981.

62. C. V. Trigt, Tj. Hollander & C. T. J. Alkemade, "Determination of the a-Parameter of Resonance Lines in Flames", JQSRT, vol. 5, p813, 1965.

63. P. R. Bevington, "Data Reduction and Error Analysis for the Physical Sciences", McGraw-Hill, 1969.

64. S. J. Kline & F. A. McClintock, Mech. Eng., 75, 3, 1953.

65. H. W. Liepmann & A. Roshko, "Elements of Gasdynamics", John Wiley & Sons, 1957.

66. P. Materna, "Hot Wire Anemometry in a Low Density Hypersonic Turbulent Boundary Layer", thesis, Princeton University, 1979.

67. S. Pai, "Fluid Dynamics of Jets", John Wiley & Sons, 1954.

68. J. C. Laurence & V. A. Sandborn, "Heat Transfer form Cylinders", Symposium on Measurements in Unsteady Flow, Amer. Soc. Mech. Eng., 1962.

69. C. C. Horseman & W. C. Rose, "Hot Wire Anemometry in Supersonic Flow", NASA TM X-62, P495, Dec. 1975.

70. C. K. W. Tam, "On the Noise of a Nearly Ideally Expanded Jet", J. Fluid Mech., Vol. 51, Part 1, p69, 1972.

71. C. K. W. Tam & P. J. Morris, "The Radiation of Sound by the Instability Waves of a Compressible Plane Turbulent Shear Layer", J. Fluid Mech., Vol. 98, Part 2, p349, 1980.

72. D. K. Mclaughlin, G. L. Morrison & T. R. Troutt, "Experiments on the Instability Waves in a Supersonic Jet and Their Acoustic Radiation", J. Fluid Mech., Vol. 69, Part 1, p73, 1975.

73. T. R. Troutt & D. K. Mclaughlin, "Experiments on the Flow and Acoustic Properties of a Moderate-Reynolds-Number Supersonic Jet", J. Fluid Mech., Vol. 116,, p123, 1982.

74. J. C. McDaniel, Jr., "Investigation of Laser-Induced Iodine Fluorescence for the Measurement of Density in Compressible Flows", SUDAAR No.532, Standford University, Jan. 1982.

75. J. M. Telle & C. L. Tang, "Very Rapid Tuning of CW Dye Laser", Appl. Phys. Lett., Vol. 26, No. 10, p572, May 1975.

76. L. Krause, "Sensitized Fluorescence and Quenching", Adv. in Chem. Phys., Vol. 28, Chap. 4, 1975.

77. N. H. Wrobel & N. H. Pratt, "Laser Induced Sodium Fluorescence Measurements in a Turbulent Propane Diffusion Flame", Appl. Phys. Lett. 32(5), March 1978. 17th Symposium on Combustion.

78. C. H. Muller, K. Schofield, & M. Steinberg, "Laser Induced Flame Chemistry of Li and Na. Implications for Other Saturated Mode Measurements", J. Chem. Phys., 72, p6620, June 1980.

79. A. C. Eckbreth, P. A. Bonczyk, & J. F. Verdieck, "Review of Laser Raman and Fluorescence Techniques for Practical Combustion Diagnostics", EPA-600/7-77-066, June 1977.Phys., 14, L85, 1981.

80. J. W. Daily, "Saturation Effects in Laser Induced Fluorescence Spectroscopy", Appl. Opt., Vol. 16, No. 3, p568, March 1977.

81. J. W. Daily, "Saturation of Fluorescence in Flames with Gaussian Laser Beam", Appl. Opt., Vol. 17, No. 2, p225, Jan. 1978.

82. J. W. Daily, & C. Chen, "Laser-Induced Fluorescence Measurement of Sodium in Flames", Combustion & Flame, 33, p47, 1978.

83. D. H. Campbell & J. W. Lewis, "Detailed Temporal Behavior of Laser-Excited Sodium Tracer in Nitrogen and Application to Nitrogen Number Density Measurements at Low Densities", Appl. Opts., Vol. 20, No. 23, p4102, Dec. 1981.

84. J. Driscoll, "Development of the Electron Beam Fluorescence Technique for Measurements in a Hypersonic Turbulent Flow", Ph.D. thesis, Princeton University, June 1975.

85. F. Durst, A. Melling & J. H. Whitelaw, "Principles & Practice of Laser Doppler Anemometry", Academic Press, 1976.

86. Drain, "The Laser Doppler Technique", John Wiley & Sons, 1980.

87. Proceedings of L. D. A. Symposium, "The Accuracy of Flow Measurements by Laser Doppler Methods", Demark, 1975.

88. S. A. Self & J. H. Whitelaw, "Laser Anemometry for Combustion Research", Combustion Science & Technology, 1976, vol. 13, p171.

89. M. K. Mazumder & K. J. Kirsch, "Flow Tracing Fidelity of Scattering Aerosol in Laser Doppler Velocimetry", Appl. Optics, vol. 14, No. 4, p894, April 1975.

90. D. Kreid, "Laser Doppler Velocimeter Measurements in Nonuniform Flow: Error Estimates", Appl. Opt., vol. 13, No. 8, p1872, Aug. 1974.

91. D. A. Jackson & D. M. Paul, "Measurement of Supersonic Velocity and Turbulence by Laser Anemometry", J. of Phys. E, p173, 1971.

92. W. J. Yanta "Turbulence Measurements with a Laser Doppler Velocimeter", NOLTR 73-94, 1973.

93. P. Bradshaw, "An Introduction to Turbulence and Its Measurement", Pergamon Press, 1971.

94. V. A. Sandborn, "Resistance Temperature Transducers", Metrology Press, 1972.

95. TSI Technical Bulletin.

96. R. J. Emrich, "Fluid Dynamics-Method of Experimental Physics, vol. 18, Part A", Academic Press, 1981.

97. L. S. G. Kovasznay, "The Hot Wire Anemometer in Supersonic Flow", J. of the Aeronautical Sciences, p565, 2/1950.

98. L. S. G. Kovasznay, "Turbulence in Supersonic Flow", J. of the Aeronautical Sciences, vol. 20, No. 10, p657, 1953.

99. V. A. Sandborn, "A Review of Turbulence Measurements in Compressible Flow", NASA TMX-62.337.

100. V. S. Demin & N. A. Zheltukhin, "Interpretation of Hot-Wire Anemometer Readings in a Flow with Velocity Pressure and Temperature Fluctuations", Fluid Mechanics-Soviet Research, vol. 2, No. 3., p64, 1973.

101. C. L. Ko, D. K. McLaughlin & T. R. Troutt, "Improved Technique for Hot-Wire Fluctuation Measurements in Supersonic Flows", AIAA paper No. 76-398, 1976.

102. P. R. Berman, "Speed-Dependent Collisional Width and Shift Parameters in Spectral Profiles", JQSRT, vol. 12, p1331, 1972.

103. H. M. Pickett, "Effects of Velocity Averaging on the Shapes of Absorption Lines", J. Chem. Phys., 73(12), p6090, 1980.

104. B. W. Fowler & C. C. Sung, "Doppler and Collision-Broadening Effects in the Profile of Spectral Lines", J. Opt. Soc. Am., vol. 65, No. 8, p949, 1975.

105. R. J. Lovett & M. L. Parsons, "Implications of a Speed Dependent Modified Voigt Function in Atomic Absorption Spectrometry", Spectrochimica Acta, vol. 32B, p421, 1977.

106. M. Mizushima, "Velocity Distribution in Spectral Line Shape", JQSRT, vol. 7, p505, 1967.

107. M. Mizushima, "Velocity Distribution Effect in Pressure Broadened Spectral Lines", JQSRT, vol. 11, p471, 1971.

108. F. N. Edmonds, Jr., "Line Absorption Coefficient Profiles for Velocity-Dependent Broadening", JQSRT, vol. 8, p1447, 1968.

109. A. Ben-Reuven, "Spectral Line Shapes in Gases in the Binary-Collision Approximation", Adv. Chem. Phys., 33, p235, 1975.

110. S. C. M. Luijendijk, "On the Shape of Pressure-Broadened Absorption Lines in the Microwave Region, I. Derivations from the Lorentzian Line Shape", J. Phys. B, vol. 10, No. 9, p1735, 1977.

111. R. S. Frost, "A theory of Microwave Lineshifts", J. Phys. B, No. 9, p1001, 1976.

112. H. M. Pickett, "General Rotational Relaxation Matrix: Its Properties, M Dependence, and Relation to Experiment", J. Chem. Phys., No. 61, p1923, 1974.

113. H. A. Rabitz & R. G. Gordon, "Semiclassical Perturbation Theory of Molecular Collisions, I. First and Second Order", J. Chem. Phys., No. 53, p1815, 1970.